UNIVERSITY OF CALIFORNIA

Los Angeles

Data-driven approaches for assessing hydroclimate change across scales

A dissertation submitted in partial satisfaction

of the requirements for the degree

Doctor of Philosophy in Atmospheric and Oceanic Sciences

by

Gavin Dayanga Madakumbura

2024

ABSTRACT OF THE DISSERTATION

Data-driven approaches for assessing hydroclimate change across scales

by

Gavin Dayanga Madakumbura
Doctor of Philosophy in Atmospheric and Oceanic Sciences
University of California, Los Angeles, 2024
Professor Alexander D. Hall, Co-Chair
Professor J. David Neelin, Co-Chair

The hydrologic cycle is significantly impacted by climate change, affecting both human societies and ecosystem health. Climate change-driven changes in the hydrological cycle can be subtle and difficult to identify, due to noise arising from natural climate variability and uncertainties in the tools used to understand this forced change, such as climate models. This dissertation investigates these changes across different scales, to discern the effects of climate change amidst inherent variability and modeling challenges. It explores the complex interplay between climate change, climate variability, and their impacts on the hydrological cycle, with a particular focus on precipitation patterns, wildfires, and droughts. Central to this research is the application of machine learning (ML) techniques to dissect and understand these phenomena on various spatial and temporal scales.

The first main research theme focuses on enhancing the understanding of the climate change signal within historical climate model simulations and future projections of precipitation on a global scale. In Chapter 2, utilizing ML methods and state-of-the-art climate model simulations, we identify the anthropogenic fingerprints in historical records of annual maximum daily precipitation across four observational and seven reanalysis datasets. Chapter 3 is dedicated to understanding future changes in precipitation patterns and reducing the uncertainty of these projections. We introduce an emergent constraint on the

tropical atmospheric overturning circulation, a major contributor to model uncertainty in future precipitation patterns. Using ML, we estimate the observational estimates of this emergent constraint, yielding a constrained distribution of the future change in circulation (from -1.41±1.06 %/K to -2.20±0.93 %/K). Through this approach, we provide constrained spatial patterns of future precipitation changes, important for impact assessments.

The second main theme focuses on the regional and ecosystem-scale impacts of climate change and climate variability, through changes in the hydrological cycle. In Chapter 4, we focus on the historical fire season onset timing in 13 of California's ecoregions, showing that onset is primarily controlled by climate variability and change via altering fuel moisture. Through this mechanistic knowledge, we quantify the contribution of climate change to the advancing trend in onset. We use an ML-based dynamical adjustment technique to separate the effects of climate change and variability on climatic drivers. We show that climate change has contributed to an advancement of onset by 5-55 days during the 1992-2020 period, across 11 out of 13 ecosystems. Chapter 5 focuses on the impact of droughts on California's forests, particularly the severe 2012-2015 drought, which led to massive tree die-offs in the Sierra Nevada forests. We investigate the vulnerability of forests to drought, with a special interest in why certain areas were more affected and in the drought resistance of southern versus northern Sierra forests. Utilizing remote sensing and climate data, the research identifies a drought sensitivity timescale and examines the interaction between this timescale and drought severity to understand the spatial and temporal patterns of tree mortality. ML is employed to analyze factors contributing to tree mortality, revealing that forests in the Northern Sierras would be susceptible if the drought severity were spatially uniform. The study also explores potential future impacts of climate change on drought severity and forest vulnerability, using global climate simulations to predict changes in drought patterns and their effects on forest die-offs.

There has been a vast uptake of machine learning methods in climate science research over the last few years. The variety of data-driven approaches used throughout this thesis

highlights the wide range of ML applications for understanding hydroclimate change and its impacts. These applications pave the way for future implementation of data-driven methods in the climate sciences, especially in separating the impacts of climate change from internal variability.

The dissertation of Gavin Dayanga Madakumbura is approved.

Karen McKinnon

Gang Chen

J. David Neelin, Committee Co-Chair

Alexander D. Hall, Committee Co-Chair

University of California, Los Angeles

2024

Table of Contents

List of Figures

List of Tables

Acknowledgments

I extend my sincerest gratitude to my PhD advisor, Alex Hall, for being an exemplary guide and mentor throughout my doctoral journey. His unwavering support, insightful mentorship, and generous kindness have profoundly shaped my growth, both as a researcher and as an individual. His encouragement has been instrumental in my development, inspiring me to strive for excellence in all aspects of my life.

I also extend my sincere appreciation to all my friends and colleagues at UCLA for their invaluable support and camaraderie. Their encouragement and insights have greatly enriched my academic journey and personal growth.

A special thank you goes to my collaborators and co-authors, whose expertise, dedication, and collaboration have been instrumental in the success of our joint endeavors. Their commitment to excellence and teamwork has not only facilitated significant achievements but also made the process a truly rewarding experience.

Additionally, I must express my profound gratitude to the UCLA Atmospheric and Oceanic Sciences faculty and staff. Their guidance, expertise, and unwavering support have created an environment conducive to learning and research. The opportunities provided, along with the professional and personal development I have gained, are deeply appreciated. Their dedication to nurturing the next generation of scientists has left an indelible mark on my career and life.

I want to express my deep gratitude to my mother, who has been an unwavering source of support throughout my entire life. Her guidance, encouragement, and sacrifices have not only shaped me into the person I am today but have also laid the foundation for my successes. Her constant belief in me and her endless love have been my guiding light, for which I am eternally thankful.

Lastly, and most importantly, my heartfelt appreciation goes to my wife, Medina, whose exceptional support has been the cornerstone of my journey. Her incredible strength in

managing our household, caring for our baby girl (who is only 9 months old at the time of writing), and providing me with the space and tranquility to pursue my work and research has been nothing short of remarkable. Her sacrifices and unwavering belief in my abilities have been pivotal to my achievements. For her love, patience, and support, I am profoundly grateful.

Funding support for my graduate education was provided by the UCLA Atmospheric and Oceanic Sciences Departmental Fellowship, and Richard P. and Linda S. Turco Graduate Student Fellowship, UCLA Dissertation Year Fellowship, Regional and Global Model Analysis Program for the Office of Science of the U.S. Department of Energy through the Program for Climate Model Diagnosis and Intercomparison, University of California Laboratory Fees Research Program (LRF-18-542511), Department of Energy through the HyperFACETS (DE-SC0016605) project.

Vita

2020–2024	Ph.D. Candidate in Atmospheric Sciences, University of California Los Angeles, USA
2018–2020	M.S. in Atmospheric Sciences, University of California Los Angeles, USA
2015–2017	M.S. in Civil Engineering, University of Tokyo, Japan
2010–2014	B.S. in Civil Engineering, University of Peradeniya, Sri Lanka

Publications

1. **Madakumbura, G. D.**, Kim, H., Utsumi, N., Shiogama, H., Fischer, E. M., Seland, Ø., Scinocca, J. F., Mitchell, D. M., Hirabayashi, Y., Oki, T. (2019). Event-to-event intensification of the hydrologic cycle from 1.5 °C to a 2 °C warmer world. *Scientific Reports*, 9(1), 3483. https://doi.org/10.1038/s41598-019-39936-2

2. **Madakumbura, G. D.**, Goulden, M. L., Hall, A., Fu, R., Moritz, M. A., Koven, C. D., Kueppers, L. M., Norlen, C. A., Randerson, J. T. (2020). Recent California tree mortality portends future increase in drought-driven forest die-off. *Environmental Research Letters*, 15(12), 124040. https://doi.org/10.1088/1748-9326/abc719

3. **Madakumbura, G. D.**, Thackeray, C. W., Norris, J., Goldenson, N., Hall, A. (2021). Anthropogenic influence on extreme precipitation over global land areas seen in multiple observational datasets. *Nature Communications*, 12(1), 3944. https://doi.org/10.1038/s41467-021-24262-x

4. Norris, J., Hall, A., Chen, D., Thackeray, C. W., **Madakumbura, G. D.** (2021). Assessing the Representation of Synoptic Variability Associated With California Extreme

Precipitation in CMIP6 Models. *Journal of Geophysical Research: Atmospheres*, 126(6), e2020JD033938. https://doi.org/10.1029/2020JD033938

5. Klein, S. A., Barnes, E. A., Bonfils, C., Durack, P. J., Goncalves, A., Hall, A. D., Lee, J., Ma, H., **Madakumbura, G. D.**, Ordoñez, A., Pallotta, G., Po-Chedley, S., Zelinka, M. D., Zhang, C. J. (2021). Advancing the Predictability of Water Cycle Phenomena via the Application of AI to Model Ensemble Simulations and Observations. *Artificial Intelligence for Earth System Predictability*, U.S. Department of Energy, AI4ESP1069. https://www.ai4esp.org/white-papers/.

6. Robbins, Z. J., Xu, C., Aukema, B. H., Buotte P. C., Chitra-Tarak, R., Fettig, C. J., Goulden, M. L., Goodsman, D. W., Hall, A. D., Koven, C. D., Kueppers, L. M., **Madakumbura, G. D.**, Mortenson, L. A., Powell, J. A., Scheller, R. M. (2022). Contemporary Warming Increased Bark Beetle-Induced Tree Mortality by 30% During an Extreme Drought in California. *Global Change Biology*, 28(2), 509-523. https://doi.org/10.1111/gcb.15927

7. Norris, J., Hall, A., Thackeray, C. W., Chen, D., **Madakumbura, G. D.** (2022). Evaluating Hydrologic Sensitivity in CMIP6 Models: Anthropogenic Forcing versus ENSO. *Journal of Climate*, 35(21), pp.3355-3368. https://doi.org/10.1175/JCLI-D-21-0842.1

8. **Madakumbura, G. D.**, Norris, J., Thackeray, C., Po-Chedley, S., Ahmed, F., Hall, A. (in review at *Nature Climate Change*). Emergent Constraint on Future Changes in the Tropical Atmospheric Circulation. preprint available at Research Square. https://doi.org/10.21203/rs.3.rs-3908042/v1

9. **Madakumbura, G. D.**, Moritz, M. A., McKinnon, K., Williams, A. P., Rahimi S. Bass, B., Norris J., Fu, R., Hall, A. (in review at *Nature Geoscience*). Climate change drives earlier wildfire season onset in California. preprint available at Research Square. https://doi.org/10.21203/rs.3.rs-883244/v1

10. Norris, J., Hall, A., Thackeray, C. W., **Madakumbura, G. D.** (2023). Historical sensible-heat-flux variations key to predicting future hydrologic sensitivity. *npj Climate and Atmospheric Science* (accepted).

CHAPTER 1

Overview

Understanding the variations and changes in the hydrologic cycle is of paramount importance to human and ecological systems (*Intergovernmental Panel on Climate Change*, 2022). Climate change alters Earth's hydrologic cycle, changing not only the global average amount but also the regional patterns of rainfall (*Allan et al.*, 2020). Understanding various characteristics of this change is crucial for different aspects of human and ecological health, and also for future mitigation and adaptation planning on different spatial and temporal scales. However, the complex dynamical nature of the changes in hydroclimate makes it difficult to isolate the climate signal from the noise arising from climate variability and, oftentimes, from the tools that are used for the tasks, such as Earth system models (*Hegerl and Zwiers*, 2011). This dissertation explores various aspects of changes in the global hydrological cycle, specifically precipitation, across various spatial and temporal scales using data-driven approaches to identify the influence of climate change and climate variability.

Among the methodological approaches available to separate the climate change signal from the noise, data-driven, pattern-based machine learning (ML) methods have recently gained popularity (*Wills et al.*, 2020a). These machine learning approaches facilitate the utilization of spatiotemporal changes associated with the forced response to better understand the nonlinear evolution and the interactions between the signal and noise terms (*Barnes et al.*, 2020). In this thesis, I utilize ML methods ranging from linear, interpretable, regularized regression to non-linear neural networks, along with neural network visualization techniques (*Bach et al.*, 2015). Using these tools, this dissertation addresses two main research themes. The first theme aims to enhance understanding of the climate change signal

in historical climate model simulations and future climate model projections of precipitation, from a global to a continental scale. Under this research theme, I explore the climate change signal of extreme precipitation in historical records (Chapter 2; *Madakumbura et al.* 2020) and the possible constraints on future regional patterns of precipitation projections (Chapter 3; *Madakumbura et al.* 2024a). The second theme is dedicated to understanding the ecoregion-level impacts of historical climate change and climate variability on wildfire characteristics (Chapter 4; *Madakumbura et al.* 2024b) and the impacts of drought on forests (Chapter 5; *Madakumbura et al.* 2020) in California's ecosystems.

Extreme precipitation significantly impacts society by causing disastrous conditions such as flooding, erosion, crop damage, and indirect health impacts (*Handmer et al.*, 2012; *Crimmins et al.*, 2016). Anthropogenic climate change alters Earth's hydrological cycle, intensifying extreme precipitation events (*O'Gorman and Schneider*, 2009). Understanding the climate change signal in historical observational records is crucial for a better understanding of the Earth system's response to anthropogenic forcing and for policy decision-making on climate change adaptation and mitigation efforts (*Intergovernmental Panel on Climate Change*, 2022). Previous studies in the subfield of Detection and Attribution, which focus on detecting the climate change signal in observations, have utilized historical climate model simulations and their multimodel mean trend (or the first principal component) as an anthropogenic fingerprint (*Hegerl and Zwiers*, 2011). Projecting observations onto this fingerprint has helped identify the presence of human influence in the observational record. However, a significant limitation of these studies is their reliance on a single, quality-controlled but spatially incomplete dataset, primarily due to the methodological dependence on long-term trends for detection. Moreover, these studies have not accounted for climate model uncertainty (*Ribes et al.*, 2017). A recently introduced ML-based method overcomes these limitations by using spatiotemporal variation in data to distinguish the signal from the noise caused by model uncertainty and internal variability (*Barnes et al.*, 2019, 2020). This approach, which does not depend on long-term trends in historical records, is capable of incorporating nonlinear

changes and the interactions of the forced signal with natural variability. Furthermore, unlike traditional fingerprinting methods, the fingerprints identified through this method are dynamic, varying over time. In Chapter 2, we apply this ML-based method, trained using the CMIP6 ensemble, to global historical annual maximum daily precipitation data from four observational and seven reanalysis products. Through this analysis, we efficiently generate multiple lines of evidence of an anthropogenic signal in the various manifestations of the observed record.

Future projections of precipitation contain significant climate model uncertainty (*Intergovernmental Panel on Climate Change*, 2022). This uncertainty primarily arises from changes in the dynamical component of precipitation, which is associated with changes in circulation (*Bony et al.*, 2013). While energetics can impose a theoretical limit on the global mean change in precipitation (*Allen and Ingram*, 2002), regional changes in precipitation depend on this dynamical component, which has various competing factors contributing to it and, therefore, has not been constrained before. Motivated by our previous work on constraining hydrological sensitivity (*Norris et al.*, 2022a), and the latest advances in how SST patterns can create similar sensitivity to the tropical (30S-30N) atmospheric overturning circulation (ATOC) under natural variability and climate change (*Zhang et al.*, 2023), in Chapter 3, I investigate the dynamical response in precipitation and the circulation patterns that drive this response. Through this analysis, I introduce an emergent relationship between future projected ATOC and that under natural variability. Constraining the future ATOC spread using the emergent relationship and observations is challenging due to the lack of vertical velocity observations and the uncertainty in reanalysis vertical velocity estimates (*Chemke and Polvani*, 2019), which are the closest we have to observations for this variable. Therefore, I introduce an ML framework, where I model the ATOC of climate model simulations representing only natural variability, using spatial maps of surface air temperature and sea level pressure. The idea is that an ML model trained on GCMs can be applied to observations, similar to *Madakumbura et al.* (2021). This approach allows us to obtain

observational estimates for the historical climate and, therefore, obtain the constrained future ATOC distribution using the above-identified emergent relationship. Finally, we use this constrained future ATOC to obtain future changes in regional precipitation, yielding a constrained regional precipitation projection.

Impact-relevant spatial and temporal scales have been studied during this dissertation research, particularly related to ecohydrology and wildfires. One aspect of wildfires that has received less attention is the temporal aspects of the fire season, particularly the onset of the fire season, which has practical implications for fire risk forecasts (*National Interagency Coordination Center*, 2021). In Chapter 4, we attempt to understand the historical variability and changes in fire season onset and the drivers behind these aspects. By utilizing a comprehensive fire occurrence dataset, I demonstrate that the fire season onset has been predominantly controlled by the climate, rather than by fuel variability and changes in human ignitions. Once we have developed a predictive model for fire season onset, based on physical understanding and climate drivers, we decompose the climate change and climate variability components of historical climate records to quantify the contributions from natural variability and climate change to fire season onset. For this, I use an ML-based version of the signal separation technique known as dynamical adjustment (*Smoliak et al.*, 2015). For each climate variable, the time series is modeled using a proxy for circulation variability (in our case, spatial maps of sea level pressure). This circulation-driven component is identified as the dynamical component or the internal variability component, while the residual is considered as the thermodynamic change or the climate change component. Through this approach, we quantify the impact of climate change and climate variability on fire season onset across all ecoregions of California.

Droughts can have profound effects on ecosystems and human societies (*Mishra and Singh*, 2010). Forests are particularly vulnerable to severe droughts in a warming world, as drought stress on vegetation can be exacerbated by warming driven by climate change (*McDowell et al.*, 2019). An improved understanding of how forests respond to droughts

on an ecosystem scale can provide valuable information for forest managers to anticipate patterns of tree vulnerability and to plan adaptation strategies. During 2012-2015, California experienced a severe multi-year drought that contributed to the die-off of millions of trees in the Sierra Nevada forests (*Fettig et al.*, 2019). This massive forest die-off exhibited distinct spatiotemporal patterns. One research question explores why different regions experienced varying levels of drought stress and whether there is a particular drought duration to which some trees are more vulnerable. Furthermore, it examines whether forests in the Southern Sierras, which were particularly affected by the drought, are less drought-resistant compared to northern forests. In Chapter 5, using remote sensing-based vegetation stress metrics—Normalized Difference Moisture Index, Normalized Difference Vegetation Index, and Canopy Water Content, along with high-resolution climate data (*Flint et al.*, 2013), we attempt to answer these questions. We used data from before 2012 to identify the duration of drought that was best correlated with anomalies in vegetation condition time series, introducing a drought sensitivity timescale (DST). We then investigated how the pre-2012 DST interacted with drought severity to produce the observed spatial and temporal patterns of die-off during the 2012-2015 drought. Utilizing machine learning (ML), specifically a random forest model (*Breiman*, 2001), we modeled the 2012-2015 forest die-off using physically based drivers of tree mortality. This ML model demonstrates that forests in the Southern Sierras were most affected by the severity of the drought. Moreover, had the drought been spatially uniform in severity, the Northern Sierra forests could also have experienced a severe tree mortality episode. Finally, we use output from state-of-the-art global climate simulations to examine how changes in multi-year droughts may amplify future die-off episodes.

CHAPTER 2

Anthropogenic influence on extreme precipitation over global land areas seen in multiple observational datasets

[**Madakumbura, G. D.**, Thackeray, C. W., Norris, J., Goldenson, N., Hall, A. (2021). Anthropogenic influence on extreme precipitation over global land areas seen in multiple observational datasets *Nature Communications*, 12(1), 3944. https://doi.org/10.1038/s41467-021-24262-x]

Abstract

Global climate models produce large increases in extreme precipitation when subject to anthropogenic forcing, but detecting this human influence in observations is challenging. Large internal variability makes the signal difficult to characterize. Models produce diverse precipitation responses to anthropogenic forcing, mirroring a variety of parameterization choices for subgrid-scale processes. And observations are inhomogeneously sampled in space and time, leading to multiple global datasets, each produced with a different homogenization technique. Thus, previous attempts to detect human influence on extreme precipitation have not incorporated internal variability or model uncertainty, and have been limited to specific

regions and observational datasets. Using machine learning methods, we find a physically interpretable anthropogenic signal that is detectable in all global datasets. Detection occurs even when internal variability and model uncertainty are taken into account. Machine learning efficiently generates multiple lines of evidence supporting detection of an anthropogenic signal in extreme precipitation.

2.1 Introduction

Extreme precipitation can have devastating direct societal impacts such as flooding, soil erosion, agricultural damages (*Handmer et al.*, 2012) and indirect health risks and impacts (*Crimmins et al.*, 2016). Anthropogenic warming acts to intensify Earth's hydrologic cycle (*Allen and Ingram*, 2002; *O'Gorman and Schneider*, 2009). This intensification is manifested in part through increased extreme precipitation as a result of greater atmospheric moisture with warming following the Clausius-Clapeyron relationship. However, circulation changes can act to enhance or reduce this increase (*O'Gorman and Schneider*, 2009; *Trenberth et al.*, 2003; *Held and Soden*, 2006; *Norris et al.*, 2019). If current warming trends continue, climate models project that the Earth's atmosphere overall will move towards a more intense precipitation regime (*Sun et al.*, 2006; *Fischer et al.*, 2013; *Kharin et al.*, 2013; *Sillmann et al.*, 2013). Moreover, increased variation between wet and dry extremes is projected, which could have devastating societal impacts (*Madakumbura et al.*, 2019; *Swain et al.*, 2018). These changes in extreme precipitation may have already become apparent on a regional basis (*Allan and Soden*, 2008; *Min et al.*, 2011; *Donat et al.*, 2016, 2019).

Recent studies have detected anthropogenic influence in historical changes to extreme precipitation across North America (*Kirchmeier-Young and Zhang*, 2020) and Northern Hemisphere land areas (*Min et al.*, 2011). These attempts are part of a larger category of studies known as Detection and Attribution (D&A). Often, they initially extract the spatial or spatiotemporal patterns of climate-system response to anthropogenic forcing (so-called

fingerprints) from an ensemble of global climate models (GCMs) (*Stott et al.*, 2010; *Bindoff et al.*, 2013). Projection of observations onto these fingerprints allows for signal detection as the trend of the projection (*Marvel et al.*, 2019). The presence of a signal that can be statistically distinguished from internal variability confirms the influence of anthropogenic forcing. Thus, traditional D&A methods rely on long term observations (*Hegerl and Zwiers*, 2011; *Easterling et al.*, 2016). In the case of extreme precipitation, traditional methods may be difficult to apply globally due to inordinately short records and large observational uncertainty, reflected in multiple global datasets produced with very different assumptions (*Herold et al.*, 2017; *Sun et al.*, 2018; *Roca et al.*, 2019). Another key difficulty with traditional methods is that the models produce a large spread in the extreme precipitation response to anthropogenic forcing (*O'Gorman*, 2012). This spread occurs alongside large internal variability in the models' simulations of the historical period. These two effects create significant uncertainty in the character of the "true" anthropogenic signal. In past research, spread in the response have been suppressed by assuming the anthropogenic fingerprint can be derived from the ensemble-mean change in extreme precipitation (*Ribes et al.*, 2017). Here we aim to take these uncertainties fully into account, by making no assumptions about how to derive the anthropogenic signal from GCM data.

A machine-learning-based method for the detection of anthropogenic influence (DAI) has been shown to overcome the reliance on trends (*Barnes et al.*, 2019, 2020) and is even capable of detecting the human influence from weather data on a single day (*Sippel et al.*, 2020). An artificial neural network (ANN) is trained to predict a proxy of external forcing (*e.g.*, the year of the data) based on the spatial maps of the target variable from an ensemble of GCM simulations. Then a forced signal can be confirmed despite the presence of internal climate variability and inter-model variability (*Barnes et al.*, 2019, 2020). This ANN DAI method can identify the non-linear combinations of the forced signal, internal climate variability and inter-model variability (*Barnes et al.*, 2020). This method also has the advantage of being able to explicitly include internal variability and model uncertainty. It does not assume that

any model or any model-derived quantity, such as the ensemble-mean of the models, is the "true" anthropogenic signal. And it uses the raw GCM data, with GCM internal variability included. In addition, ANN visualization techniques also allow for the interpretability of the models formerly considered as "black boxes", making them explainable (*Ebert-Uphoff et al.*, 2019; *Toms et al.*, 2020), or interpretable in terms of physical processes or system behavior. Use of these visualization techniques alongside the ANN DAI method allows one to capture the time varying dynamic fingerprints of each input and evaluate their physical credibility (*Barnes et al.*, 2020; *Wills et al.*, 2020a).

In this study, we apply the ANN DAI method and the ANN visualization technique known as Layerwise Relevance Propagation (LRP) (*Bach et al.*, 2015; *Montavon et al.*, 2018) to global maps of annual daily maximum precipitation (Rx1day) over land. Using Coupled Model Intercomparison Project, phase 5 (CMIP5) (*Taylor et al.*, 2012) and phase 6 (CMIP6) (*Eyring et al.*, 2015) model ensembles, we first aim to understand how the ANN is detecting the anthropogenic signal and interpret it physically. Then we use the ANN to detect the anthropogenic influence on Rx1day in several land-only observational and reanalysis datasets. Thus, we are agnostic about which GCM is correct, and which gridded data set is a true representation of the observed record. In this way we efficiently generate multiple lines of evidence as to the presence of an anthropogenic signal in the various instantiations of the observed record.

2.2 Data and Method

2.2.1 Data

We use daily precipitation rate output from a collection of climate models participating in CMIP5 and CMIP6 (Table 2.1). Data from each ensemble's historical forcing scenario is combined with future projections following a high-emissions scenario to create a time-series from 1920 to 2099 for each model. Future projections from CMIP5 follow the Representative

Concentration Pathway 8.5 (RCP 8.5) (*Meinshausen et al.*, 2011), while CMIP6 projections follow the Shared Socioeconomic Pathway 5–8.5 (SSP 5-8.5) (*O'Neill et al.*, 2016). To increase our sample size, we combine both CMIP5 and CMIP6 model subsets into one ensemble, which is justifiable considering the very similar time evolution of the total anthropogenic forcing in RCP 8.5 and SSP 5-8.5 scenarios (*O'Neill et al.* 2016, their Figure 3c). We regrid all daily precipitation data to a 2^o x 2^o spatial grid and compute the Rx1day value for each year at each land grid point.

We use four datasets of observational estimates of daily precipitation rate with global coverage: Multi-Source Weighted-Ensemble Precipitation, version 2 (MSWEP) (*Beck et al.*, 2018), Global Precipitation Climatology Centre (GPCC) version 2018 (*Ziese et al.*, 2018), and Rainfall Estimates on a Gridded Network (REGEN) (*Contractor et al.*, 2020), including both REGEN_ALL and REGEN_LONG. MSWEP is a hybrid reconstruction using in situ, satellite and reanalysis data, whereas GPCC and the REGEN datasets are developed from ground-based measurements. REGEN_ALL is developed by interpolating all considered station data whereas REGEN_LONG is developed using only the stations with a data record of 40 years or longer. We further use seven widely used reanalysis products for comparison : ECMWF ERA5 (*Hersbach et al.*, 2020), Japanese 55-year Reanalysis (JRA55) (*Kobayashi et al.*, 2015), Modern-Era Retrospective analysis for Research and Applications, Version 2 (MERRA2) (*Gelaro et al.*, 2017), NCEP Climate Forecast System Reanalysis (CFSR) (*Saha et al.*, 2010), Global Soil Wetness Project Phase 3 (GSWP3) (*Kim*, 2017), NCEP-DOE Reanalysis 2 (NCEP2) (*Kanamitsu et al.*, 2002) and NOAA-CIRES-DOE Twentieth Century Reanalysis version 3 (20CRv3) (*Slivinski et al.*, 2019). These observational and reanalysis datasets are selected considering the availability of full global land coverage and data for at least three decades (Table 2.2). All observation and reanalysis data were regridded to the same 2^o x 2^o spatial grid as the models, and then Rx1day was calculated at each grid point for each year.

2.2.2 Neural network based detection method

Here we apply the method in *Barnes et al.* (2019) (see their Figure 1a) to predict the year with which given annual Rx1day maps from GCMs are associated, a regression task. This requires the ANN to learn the signature of the forced response in simulated Rx1day. By feeding the ANN multicentury data from forced simulations, it learns to distinguish the forced signal from internal climate variability. The use of multiple GCMs helps the ANN learn the common elements of the forced response most relevant to the prediction task, a process that fully considers model uncertainty as well as internal climate variability. Input to the ANN from each model is a vectorized spatial map of Rx1day (2^o x 2^o spatial grid = 16200 grid values) for each year from 1920 to 2099. Our primary goal is to detect the anthropogenic signal in extreme precipitation over land. Thus, we mask out data over the ocean at this stage, resulting in 6082 land grid values. The ANN architecture consists of two hidden layers with ten nodes each. The Rectified Linear Unit activation function is used for all hidden units.

Approximately 80% of the models (35) are used for training the ANN, while the rest (9) are used for testing. K-fold validation is applied to split the initial training dataset into training and validation datasets. Here we set K=2. The mean squared error between the actual and predicted year of Rx1day is used as the loss function to be minimized during the training. For the optimizer which updates the ANN based on the gradient of the loss, we select rmsprop. Climate variables inherently contain spatial autocorrelation. To account for this dependence among adjacent input data points, we use L2 regularization between inputs and the first hidden layer, which adds the sum of squared weights as a penalty term to the loss function. By iterating over L2 values of leading order of magnitudes and inspecting the tradeoff between low prediction error and generalizability (Figure 2.1), we found L2=0.001 to be a suitable value for our analysis.

We could have made the ANN more complex to achieve higher accuracy. But we elected not to do so, partly because Increasing the number of hidden units or changing the other

hyperparameters (except for L2 regularization) did not result in a substantial increase in accuracy. More importantly, we aimed to keep the ANN simple, with a reasonable degree of accuracy. This is because the main goal is not to obtain a perfect prediction, but rather to reveal the forced patterns the ANN learns (*e.g.*, *Barnes et al.* 2019, 2020). As we show in Section 3, imperfections in the prediction also can be physically interpreted within the D&A research framework.

2.2.3 Neural network interpretation using Layerwise Relevance Propagation (LRP)

Assume that for a given input map, x, we get an output $f(x)$, in our case, the predicted year. LRP conservatively back-propagates this value through hidden layers until it reaches the input map. This process generates a relevance heatmap, indicating the areas of importance influencing the value $f(x)$. The conservation property is shown in Eq. 2.1, for relevance propagation between two hidden layers j and k, where k is the higher layer (i.e., closer to the output). The summation operation for each layer (*e.g.*, $\sum_k P_k$) is the summation of the relevance (P) of all hidden units in that layer. The activation, a_k (Eq. 2.2) is the information coming from all units in layer j, to a target unit in layer k. In Eq. 2.2, a_j values are the individual activations of each unit in the layer j, w_{jk} values are the weights associated with the relationship between each unit in layer j and the target unit k, and b_k is the bias of that target unit.

$$\sum_{i=1}^{d} P_i = \cdots = \sum_j P_j = \sum_k P_k = \cdots = f(x) \tag{2.1}$$

$$a_k = \text{ReLU}\left(\sum_j \left(a_j w_{jk} + b_k\right)\right) \tag{2.2}$$

$$P_j = \sum_k \left(\alpha \frac{a_j w_{jk}^+}{\sum_j a_j w_{jk}^+} - \beta \frac{a_j w_{jk}^-}{\sum_j a_j w_{jk}^-}\right) \tag{2.3}$$

The relevance propagation rule from layers j to k is given in Eq. 2.3. This general form is also known as the $\alpha\beta$-rule (*Bach et al.*, 2015; *Montavon et al.*, 2018). The components $()^+$ and $()^-$ indicate only positive and negative weights are being considered, respectively. The α and β coefficients represent the relative amount of positive and negative relevance to be propagated, respectively. As shown in Eq. 2.3, positive relevance (i.e., excitatory influence) and negative relevance (i.e., inhibitory influence) are associated with positive and negative weights, respectively. The α and β coefficients are to be chosen with the constraints $\alpha - \beta = 1$ and $\beta \geq 0$. The combination $\alpha = 2$ and $\beta = 1$ ($\text{LRP}_{\alpha 2 \beta 1}$) have been experimentally inferred as suitable values, and have been adopted in previous research (*Bach et al.*, 2015; *Montavon et al.*, 2018; *Böhle et al.*, 2019; *Dobrescu et al.*, 2019; *Grigorescu et al.*, 2019). Here we adopt the $\text{LRP}_{\alpha 2 \beta 1}$ rule.

The $\alpha\beta$-rule with $\alpha = 1$ and $\beta = 0$ ($\text{LRP}_{\alpha 1 \beta 0}$, also known as the Deep Taylor Decomposition) is a special case where for each input, the sum of LRP relevance heatmaps is equivalent to $f(x)$. This is a valuable property for the interpretation of results. As $\beta = 0$, $\text{LRP}_{\alpha 1 \beta 0}$ only considers the information which positively contributes to the final decision. For regression tasks such as the problem at hand here, inputs which contribute to a decrease in $f(x)$ (i.e., an earlier predicted year; negative relevance) are equally as important as inputs which contribute to an increase (i.e., a later predicted year; positive relevance) to understand what the ANN has learned. Moreover, when $\alpha > 1$, the $\alpha\beta$-rule does not conserve the relevance from the output value back to the input layer. For these reasons, *Toms et al.* (2020) pointed out that caution should be exercised when applying the $\alpha\beta$-rule with 1) $\alpha = 1$ for regression and 2) $\alpha > 1$ in general. We find that for our simple ANN, applying $\text{LRP}_{\alpha 2 \beta 1}$ results in a 1:1 relationship between the resultant relevance heatmaps and $f(x)$ for each input (Figure 2.1d and Figure 2.2d). This allows the visualization of input that contributes to a decrease in $f(x)$ while maintaining a direct relationship between the ANN predicted value and LRP heatmaps. Therefore, we proceed with rescaled relevance heatmaps derived from $\text{LRP}_{\alpha 2 \beta 1}$ for interpreting our ANN. More details on LRP can be found in previous work (*Toms et al.*,

2020; *Bach et al.*, 2015; *Montavon et al.*, 2018, 2019).

2.3 Results

2.3.1 ANN-identified fingerprints of anthropogenic influence

We first discuss the ability of the ANN to predict the year of occurrence for a series of simulated annual Rx1day maps. Predictions of the simulated Rx1day year (Figure 2.2) show that the ANN struggles during roughly the first seven to eight decades of the analysis period. But prediction accuracy gradually increases, noticeably starting from the late 20th century. Thus, compared to when this technique is applied to global-mean temperature (*Barnes et al.*, 2019) there is a lag in the emergence of the anthropogenic signal in extreme precipitation. This delay is likely due to larger internal and inter-model variability in extreme precipitation. We estimate this time of emergence (departure year) as the year when the ANN prediction continuously exceeds a selected base period (1920-1949) (see *Barnes et al.* 2019, and *Mora et al.* 2013 for more details). Some maps of simulated terrestrial Rx1day drawn from various populations of GCM training and testing data sets depart from the base period in the 1970s, but the departures mostly occur later, with lower and upper quartiles of 1991 and 2014, respectively (Figure 2.2c). According to the models, the anthropogenic signal has probably already emerged in Rx1day, consistent with traditional statistical methods (*King et al.*, 2015).

Figure 2.2d shows the relevance pattern identified by the ANN, averaged over the period 1920-1949. Positive (negative) values in the relevance pattern correspond to an increase (decrease) in the predicted year. Therefore, areas of positive relevance can be interpreted as the regions with an advancing tendency on the prediction (i.e. the year) and negative values are the regions with a retreating tendency. The sum of each grid cell value is equal to the predicted year (Figure 2.2d). These relevance patterns can be considered as the ANN-identified fingerprints of anthropogenic influence (*e.g.*, *Sippel et al.* 2020).

The regions with positive relevance include the East Asian and African monsoon regions, and the North Pacific and Atlantic storm tracks (Figure 2.3). The regions with negative relevance include arid and semi-arid subtropical zones such as Northern African and Middle Eastern deserts, Southern South Africa, Australian arid and semi-arid regions, and wet regions such as central and northwestern parts of South America. Regions with negative relevance also coincide with areas exhibiting a large negative dynamical component of the Rx1day trend (*Pfahl et al.* 2017, their Figure 3b). These regions show a significant anthropogenic reduction of vertical velocities associated with Rx1day. This offsets the Rx1day increase stemming from the thermodynamic contribution, and produces only a weak and inconsistent increase in Rx1day (*Pfahl et al.*, 2017). The uncertainty associated with the dynamical component has been identified as a major concern for D&A of precipitation (*Shepherd*, 2014). As suspected, negative relevance of the forced response is associated with lower signal to noise ratios than the regions with positive relevance (Figure 2.2, 2.2). The signal to noise ratios are lower for both internal variability and model variability. This reflects both the higher uncertainty regarding the change in extreme precipitation projected by GCMs for a majority of global arid land regions, as well as larger internal variability in those regions. Here we examined the time-averaged relevance patterns, but further examination of time-varying fingerprints shows that the ANN is also able to identify the time-varying nature of the signal and noise, which cannot be obtained directly by linear models (*Wills et al.*, 2020a).

The ANN-based relevance patterns are consistent with the idea that previously observed long-term trends of terrestrial Rx1day are anthropogenic in origin (*e.g.*, *Min et al.* 2011, their Figure 1e). Many wet land regions of the world have experienced a robust increase in Rx1day to date, whereas in dry regions no such trend can be seen (*Donat et al.*, 2016, 2019). The selection of regions in these previous studies seems to overlap with the high relevance regions in Figure 2.2d.

2.3.2 Origins of the spread in the predicted year

We next investigate why the ANN predicts such a large range of years depending on the data of the underlying GCM used to predict the year. This inter-model spread in the predicted year is especially pronounced before the warming signal emerges (Figure 2.2). Here, we select four GCMs with the highest average predicted year, and four GCMs with the lowest average predicted year, during the baseline period (1920-1949). We obtain the relevance heatmaps for each year of the baseline period for these eight models and calculate the composite difference (i.e. high value minus low value) between two sets (Figure 2.4). Large positive values are seen in the African and Asian monsoon regions. The models predicting later years also have larger 20th century mean state Rx1day values in these regions (Figure 2.3). Thus, the models that predict a higher value in the baseline period have more future-like patterns of Rx1day in their baseline climatologies compared to other models. When projected onto the fingerprints identified by the ANN, these patterns result in a later predicted year compared to the opposite subset. This exercise suggests a potential use of ANN-based DAI methods to understand how biases in historical simulations project onto future changes.

2.3.3 Detected anthropogenic signal in historical Rx1day records

With these physical interpretations of the ANN results and relevance patterns, we use the GCM-trained ANNs to detect whether there is a forced signal in observations. First, we calculate the globally-averaged Rx1day trends in each dataset using a modified Mann-Kendall trend test (*Hamed and Rao*, 1998). Only seven out of the eleven datasets show a significant trend ($p<0.01$) in globally-averaged Rx1day for the historical period, ranging from 0.05 to 0.09 mm/day/year (Table 2.2). Taken at face value, this suggests that the evidence for anthropogenic influence on recent changes in extreme precipitation is weak. However, when we apply the ANN, based on Rx1day data from GCMs, to four datasets of observational precipitation estimates and seven reanalyses, a different story emerges.

If an observational dataset exhibits the same forced response as the GCMs, the predicted year time series from that dataset should have a statistically significant positive correlation with the actual year (r) and a linear regression of these two variables should produce a statistically significant positive slope (*Marvel et al.*, 2019; *Barnes et al.*, 2020). Figure 2.5 shows these two metrics for observations, reanalysis and testing GCMs, from 51 random iterations of the ANN with different training/testing model sets. All observations and reanalysis have high r values (Figure 2.5, 2.6), even in datasets that do not show a significant positive trend in global Rx1day record (Table 2.2). The r values for all observational data sets are substantially larger than those expected by chance (grey shaded area in Figure 2.5e,f). The slope is a measure of signal strength (or the rate of change) in the Rx1day record. Two observational datasets (MSWEP and GPCC) are in line with GCMs, along with four reanalyses (JRA55, MERRA2, NCEP2 and 20CRv3). The two REGEN datasets, ERA5 and CFSR show lower slopes, whereas GSWP3 has the highest slope among the datasets considered here. In general, observational and renalysis products show similar correlations and slopes as the GCMs for the same historical time period (compare the blue dots and the pink bands in Figure 2.5e, f.) This indicates that the observational and reanalysis products show anthropogenic influence on Rx1day that is comparable to what is expected from GCMs.

These results demonstrate that the absence of a significant linear trend in globally averaged Rx1day cannot be taken to mean there is no evidence of anthropogenic signal in Rx1day. This underscores the importance of exploiting the spatial pattern of the response to external forcing to extract the forced signal in observations, as opposed to the trend-based analysis (*Sippel et al.*, 2020; *Wills et al.*, 2020a,b). In particular, areas of negative relevance, defined previously, can act to suppress the trend in the global mean. Further evidence of the importance of spatial patterns can be seen in the fact that the average ANN-predicted values vary widely and systematically across the observational datasets (Figure 2.5a-d, Figure 2.6). This is an indicator of systematic and large relative biases in the Rx1day climatologies of the various data sets (as pointed out above in the discussion of ANN applied to the GCMs,

the average predicted value of the year depends on the magnitude of the Rx1day in the climatology (Figure 2.3). Yet it is significant that the ANN can put the years in close to the correct order, as demonstrated by the significant correlations between actual and predicted years, even if the absolute value of the years is incorrect. This is a strong indicator that the subtle patterns and time variations of the simulated anthropogenic signal are present in the observational data sets and are shared among them, despite the fact that they are systematically biased relative to one another and likely the real world (*Bador et al.*, 2020; *Alexander et al.*, 2020).

2.3.4 Time varying fingerprints

One of the main advantages of using an ANN to detect anthropogenic signals over traditional D&A methods and newly introduced variants (*Sippel et al.*, 2020) is that time varying signals can be accounted for (*Barnes et al.*, 2020). Such signals could be due to the nonlinear evolution of the climate system or temporal and spatial variations in the forcing itself. Figure 2.7a shows the difference between the relevance maps for our baseline period (1920-1949) and the end of the 21st century (2070-2099). While the sum of the relevance maps derived using LRP is larger for later years compared to early years, local differences will explain the redistribution of the importance with time. This ability to aggregate over regions and different samples has been identified as an advantage of using LRP to interpret deep learning models (*Lapuschkin*, 2019; *Montavon et al.*, 2018). The relevance increases with time across Africa and Asia, which is likely to be associated in part with the enhancement of the monsoon systems. A similar increase in relevance can be seen in North Pacific and North Atlantic land regions, possibly associated with the poleward shift of storm tracks (*Yin*, 2005). South African and South American Mediterranean climate regions also show an increase in relevance, associated with subtropical drying, a robust pattern of climate change (*Lu et al.*, 2007; *Scheff and Frierson*, 2012). This indicates that even though dry regions have a smaller signal-to-noise ratio compared to wet regions in terrestrial Rx1day (Figure 2.3), some dry

regions show an increase of signal and/or decrease in noise with time, yielding an increase in the relevance (Figure 2.7). Among the regions with decreasing relevance, a majority of South America and the Western US stand out, possibly due to an increase in model uncertainty in future projections of Rx1day.

To assess the physical validity of the change in relevance determined by the ANN, we break the terrestrial Rx1day record down into its forced signal and changes in noise components between the two periods. Results show that grid cells with increasing relevance have a comparable change in Rx1day, but much less increase in both internal variability and inter-model variability compared to grid cells with decreasing relevance (Figure 2.7b). Therefore, the change of relevance over time is in accord with the tradeoff between increasing noise/intermodel spread and increasing signal with time.

2.3.5 Role of model uncertainty in detecting the anthropogenic influence

To assess the influence of model uncertainty in detecting the signal, we redid the analysis, but including a widely used highly quality controlled HadEX3 dataset (*Dunn et al.*, 2020), which along with its predecessors have been used in traditional detection and attribution of extreme precipitation (*Min et al.*, 2011; *Paik et al.*, 2020). HadEX3 and its predecessors are considered a more reliable dataset than the other observational estimates used in this study, but do not provide full global coverage. Therefore, analyses were done for all GCMs and observations, just over the regions with a continuous data coverage in HadEX3 for the period 1979-2018 (Figure 2.8). Two separate analyses were conducted. The first analysis was similar to the main analysis, using multimodel simulations to train the ANN (Figure 2.9) to include the model uncertainty. The second was done only using the multimodel mean of each training model set to train the ANN (Figure 2.10). When the model uncertainty is included, observations and reanalysis fail to identify the anthropogenic influence for the selected domain (Figure 2.9), whereas when the model uncertainty is not included signal is detected in 11 out of 13 datasets (Figure 2.10). This suggests that when the model

uncertainty is considered, the power of detecting the anthropogenic influence decreases.

Similar behavior in reanalysis and observations and the difference compared to testing data in these results (Figure 2.9, 2.10) also justifies the use of reanalysis as an alternative observation in assessing the anthropogenic influence, as argued in previous studies (*e.g.*, *Shiu et al.* 2012).

2.3.6 Sources of the spread in the signal of observations

For observations, the absolute value of the predicted year shows a wide range of values, with an overall underestimation compared to GCMs (Figure 2.5). A composite difference of the relevance and Rx1day between observations and testing models reveal that different regions contribute to this result (Figure 2.11). In observations, a lower relevance compared to GCMs can be seen over Asia and North America (Figure 2.11a,c,e,g). These patterns correspond to an underestimation of Rx1day in the historical observational record compared to GCMs (Figure 2.11b,d,f,h). Among the observations, the predicted year for GPCC is the highest, which is due to having higher Rx1day over India and Africa.

To investigate the differences in the anthropogenic signal in the four observations, we first calculated the linear trend of Rx1day for each grid cell and weighted that by the normalized relevance for grid cells with a positive relevance (Figure 2.12). A simple explanation for this difference is that when more pixels with a positive relevance show an increase in Rx1day there is an increase in the predicted year, weighted by the relevance. Confirming this, datasets with a greater anthropogenic signal (GPCC and MSWEP, as shown in Figure 2.5) have a higher number of grid cells with an increasing relevance-weighted trend in Rx1day (Figure 12) compared to the datasets with a smaller anthropogenic signal (REGEN_ALL and REGEN_LONG).

2.4 Conclusions

Detecting anthropogenic signals in observations of extreme precipitation has been a challenging task due to large internal variability of rare events, as well as climate model uncertainty. The limited sampling in observations adds additional uncertainty, due in part to a dataset development process that involves a variety of homogenization, extrapolation, and interpolation techniques to produce global gridded products. Using a recently introduced ANN DAI method which utilizes the time evolution of spatial maps of Rx1day in GCMs, subject to realistic radiative forcing, we find fingerprints of anthropogenic signals that are physically consistent with the time evolution of the forced signal. The fingerprints can be distinguished from internal variability, and emerge despite substantial model uncertainty. Using this ANN DAI method, we show that the anthropogenic signal can be detected in all global terrestrial Rx1day records considered in this study. This robust detection occurs despite large systematic biases and large discrepancies in data sources and homogenization methods.

While previous trend-based D&A assessments of Rx1day have demonstrated the human influence in this variable in some regions, those studies assume the ensemble-mean of the GCMs is the anthropogenic signal. This leads to questions as to whether further steps are needed to fully consider model uncertainty (*Ribes et al.*, 2017). We made a simple attempt to examine this issue by applying the ANN DAI method to the same widely-used, quality-controlled Rx1day record used in the previous trend-based D&A assessments. We applied the method twice, once using the same multi-model approach discussed elsewhere in this study, and once assuming the ensemble-mean time series represents the true forced response. Our results show that including internal variability and model uncertainty in the forced response reduces the power of detection (supplementary text). Therefore, the detected signal in multiple datasets in this study, with internal variability and model uncertainty being taken fully into account (Figure 2.5) is a definitive affirmation of a human influence on extreme precipitation in the historical record. Note that while all observations show this anthropogenic influence, the signal magnitude varies considerably, on par with that seen

in the GCMs. This large observational uncertainty underscores a difficulty in constraining future projections of extreme precipitation with historical climate model simulations and observations (*O'Gorman*, 2012; *Borodina et al.*, 2017).

A limitation of the ANN DAI method presented here is the inability to directly quantify the detected anthropogenic influence in terms of physical units. This is especially important when comparing the influence of individual external forcings (*e.g.*, greenhouse gases, aerosols, land use and land cover change, etc.). We also note that different ANN visualization techniques are available (*Samek et al.*, 2019), and those should be explored to understand the sensitivity of the extracted fingerprints to the ANN visualization technique. Despite these limitations, it is clear that ANN DAI methods with ANN visualization techniques are very useful and efficient in identifying the human influence on variables that are highly uncertain in GCMs, and poorly characterized in observations, such as extreme precipitation.

Acknowledgements. We acknowledge the World Climate Research Programme's Working Group on Coupled Modelling, which is responsible for CMIP, and we thank the climate modelling groups for producing and making available their model output. We also thank the Earth System Grid Federation (ESGF) for archiving the data and providing access, and various funding agencies who support CMIP and ESGF. We acknowledge support from the Regional and Global Model Analysis Program for the Office of Science of the U.S. Department of Energy through the Program for Climate Model Diagnosis and Intercomparison.

2.5 Figures

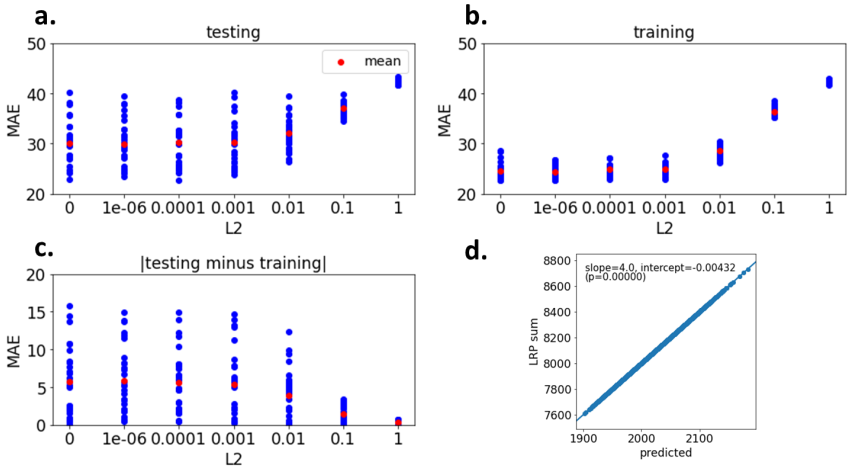

Figure 2.1: Training and testing results of the ANN. (a-c) Mean Absolute Error (MAE) for different L2 regularization values from 51 different ANNs with different training/testing sets. MAE for training data (a), testing data (b) and absolute difference of testing minus training (c). (d) Predicted year vs sum of the relevance heatmap grid cell values obtained from $\text{LRP}_{\alpha 2 \beta 1}$ for all models for a single ANN.

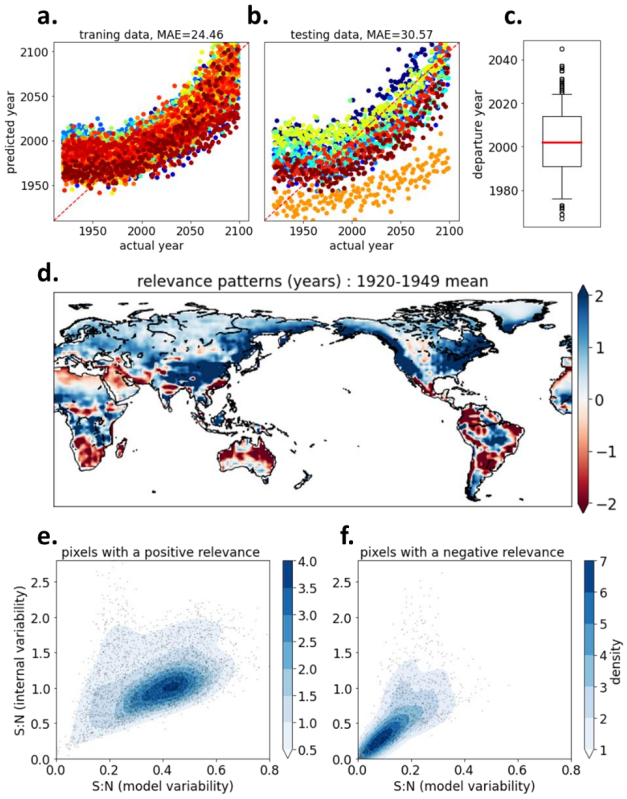

Figure 2.2: Fingerprint of external forcing in simulated Rx1day learned by the ANN. (a,b) Actual year vs predicted year for training data derived from CMIP5 and CMIP6 GCMs (a) and testing data derived from CMIP5 and CMIP6 GCMs (b) for a single ANN. Each GCM is represented by a different color. (c) The year of departure from the base period, 1920-1949, obtained from 51 different ANNs with different training/testing sets. Whiskers represent the 5th-95th percentiles, while blank circles represent outliers. (d) Multimodel, ensemble-mean, layerwise-relevance-propagation-based relevance maps for Rx1day input for the period 2070-2099 from all models. (e,f) Signal to noise ratio density plots for grid cells with a positive relevance (e) and negative relevance (f) in panel (d). Signal is defined as the multi-model mean change in Rx1day between the base period and 1920-1949. Noise is defined in two ways: The first stems from internal variability and is calculated as the multimodel ensemble mean of the standard deviation in Rx1day during the base period. The second pertains to inter-model variability, and is calculated as the inter-model standard deviation of the signal from each GCM. Each dot in (e-f) corresponds to one grid cell.

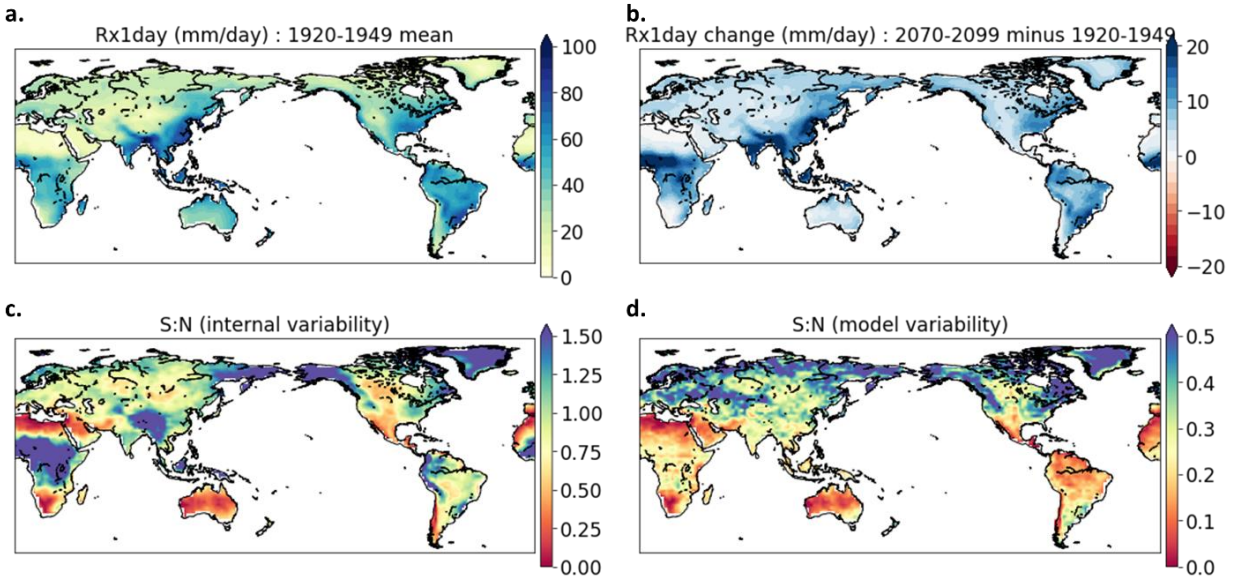

Figure 2.3: Simulated changes in Rx1day. Multimodel mean difference of Rx1day between 1920-1949 and 2070-2099. (b) Climatology of Rx1day for 1920-1949 calculated as the multimodel mean and the time mean. (c-d) Signal to noise ratios (S:N) for noise from internal variability (c) and inter-model variability (d). Signal is calculated as the multimodel mean of the Rx1day difference between the periods 2070-2099 and 1920-1949. Noise from the internal variability is calculated as the multimodel mean of the standard deviation during 1920-1949. Noise from the model variability is calculated as the inter-model standard deviation of the signal of each model.

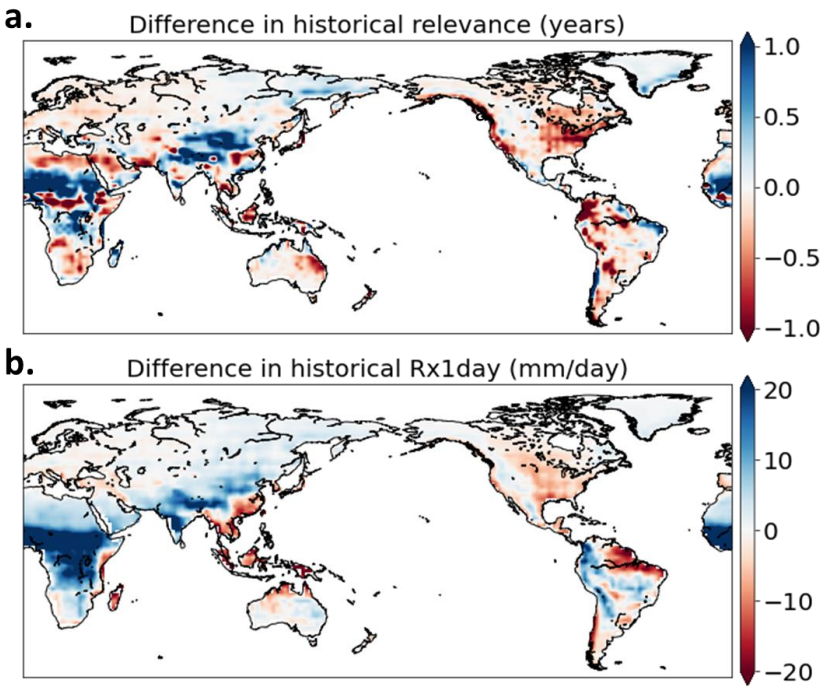

Figure 2.4: Differences between subsets of models with high and low predicted years by the ANN during the baseline period (1920-1949). (a,b) The difference in their relevance maps (a) and Rx1day (b) between the four models with the highest mean predicted year and the four models with lowest mean predicted year, (as shown in Figure 1a-b). The models from each subset are determined by combining the training and testing data.

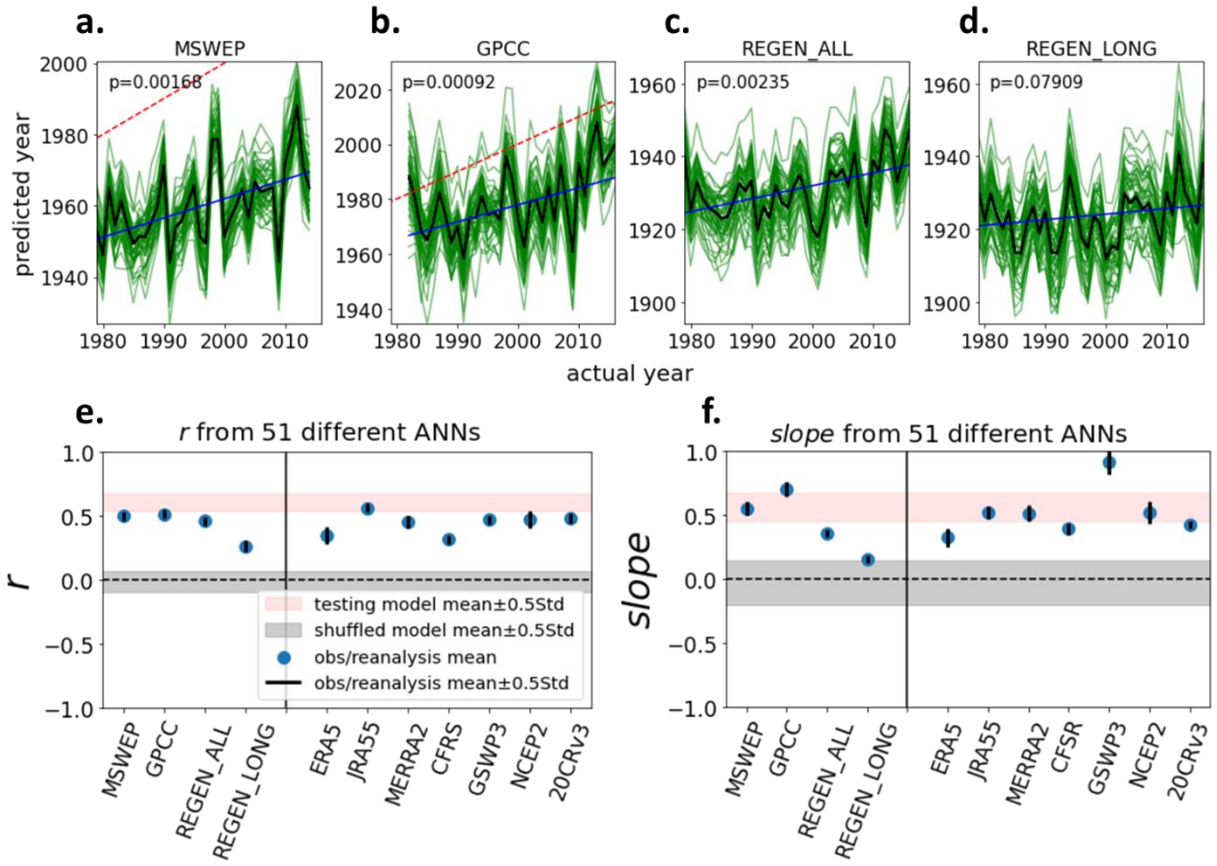

Figure 2.5: Metrics of the forced signal in observation-based estimates of precipitation since 1979. (a-d) Actual year vs predicted year obtained from 51 different ANNs with different training/testing sets, for four observational datasets, MSWEP (a), GPCC (b), REGEN_ALL (c) and REGEN_LONG (d). Green lines show results from each ANN and the black line shows the mean predicted value from all ANNs. The blue line is the best fit line of the mean predicted value. The red dashed line is the 1:1 line. (e) Correlation (r) between the actual years and predicted years, (f) slope of the regression line between actual years and predicted years for observational and reanalysis data (blue circle with black line), and testing models (red and grey shaded regions). Grey shading illustrates the values obtained from testing models after randomly shuffling, for each iteration of training/testing sets. Slope is obtained using the Theil–Sen method (*Theil*, 1950; *Sen*, 1968).

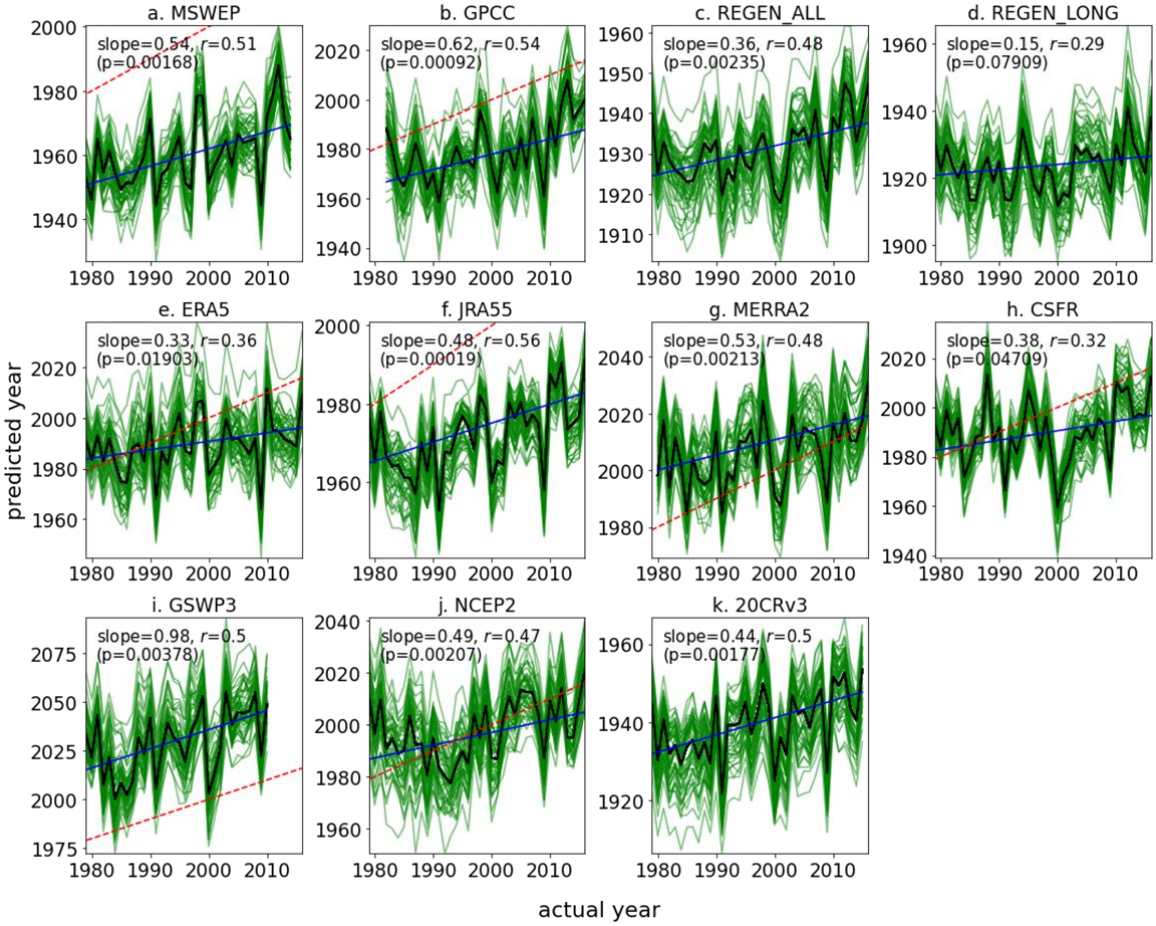

Figure 2.6: Same as Fig. 2.5(a-d), extended for reanalysis. For datasets MSWEP (a), GPCC (b), REGEN_ALL (c), REGEN_LONG (d), ERA5 (e), JRA55 (f), MERRA2 (g), CSFR (h), GSWP3 (i), NCEP2 (j),20CRv3 (k).

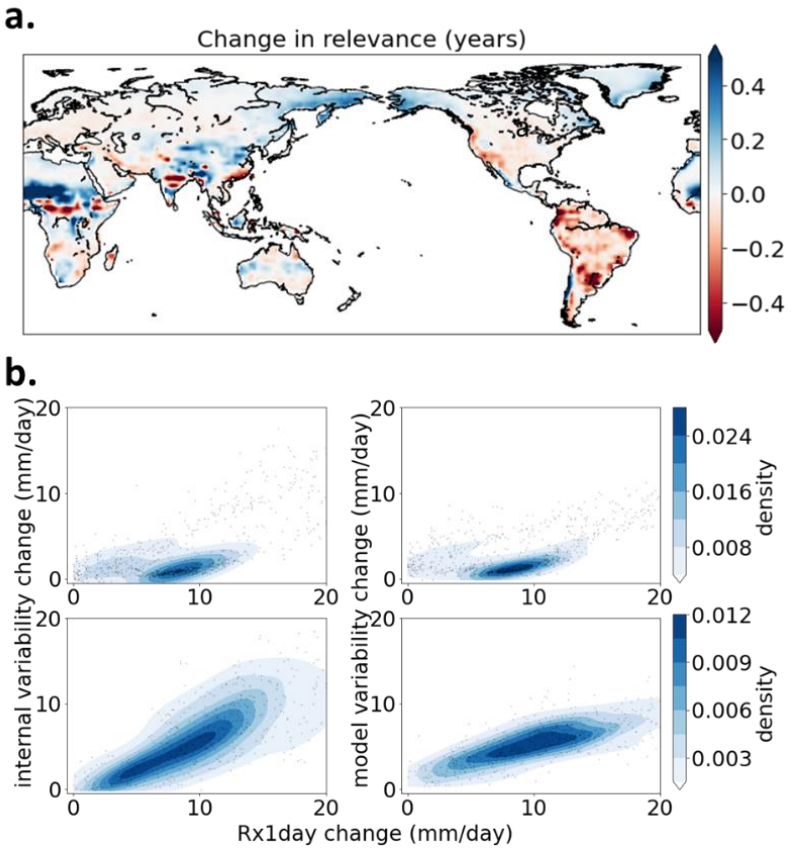

Figure 2.7: Change in the relevance learned by the ANN with time. (a) Multimodel average change of relevance maps between 2070-2099 and 1920-1949. (b) Multimodel ensemble mean change in Rx1day vs change in internal variability of Rx1day (left panels), change in Rx1day vs change in inter-model variability of Rx1day, (right panels), between 2070-2099 and 1920-1949. Top panels show results for grid cells with increasing relevance with time in panel (a) and bottom panels show results for grid cells with decreasing relevance. Internal variability is calculated as the standard deviation of Rx1day and inter-model variability is calculated as the standard deviation of mean Rx1day from all models for each time period. The Rx1day trend at each grid cell was removed by fitting a 4th order polynomial prior to calculation of internal variability. For visualization purposes, grid cells outside the threshold ±0.1 years were selected.

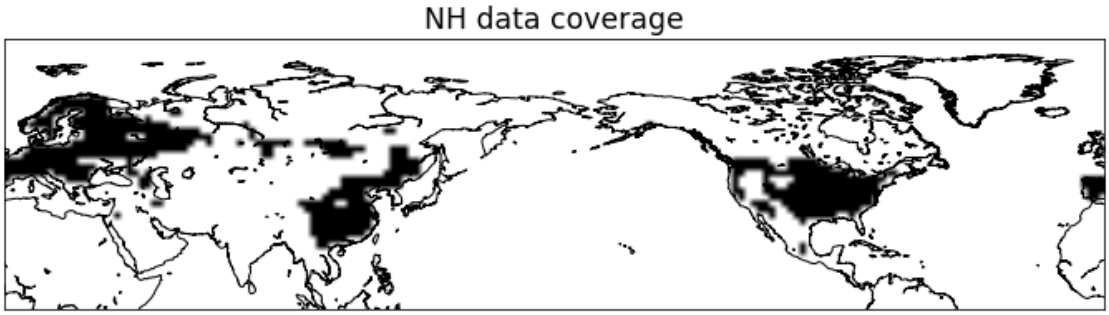

Figure 2.8: Northern hemisphere HadEX3 data coverage considered in the analysis. Only grids with a continuous data record for the period 1979-2018 (black) were selected and regridded to the common 2° x 2° spatial grid prior to the analysis.

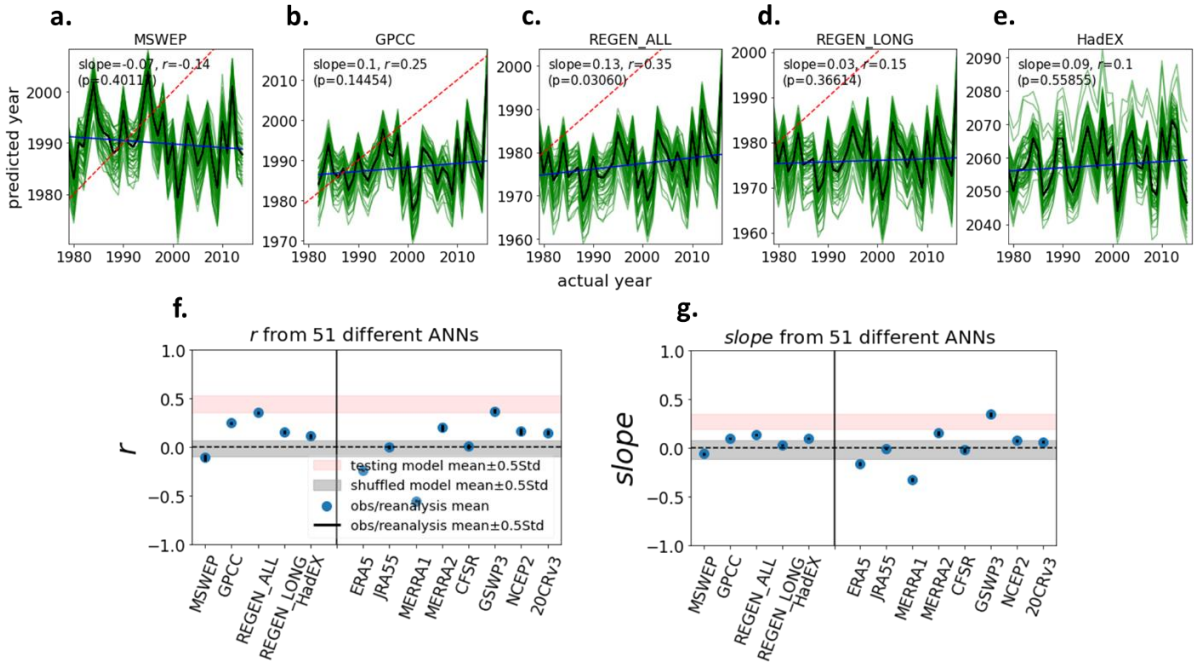

Figure 2.9: Same as Fig. 2.5 but for the domain in Fig. 2.8 and with HadEX3 based results (e-g).

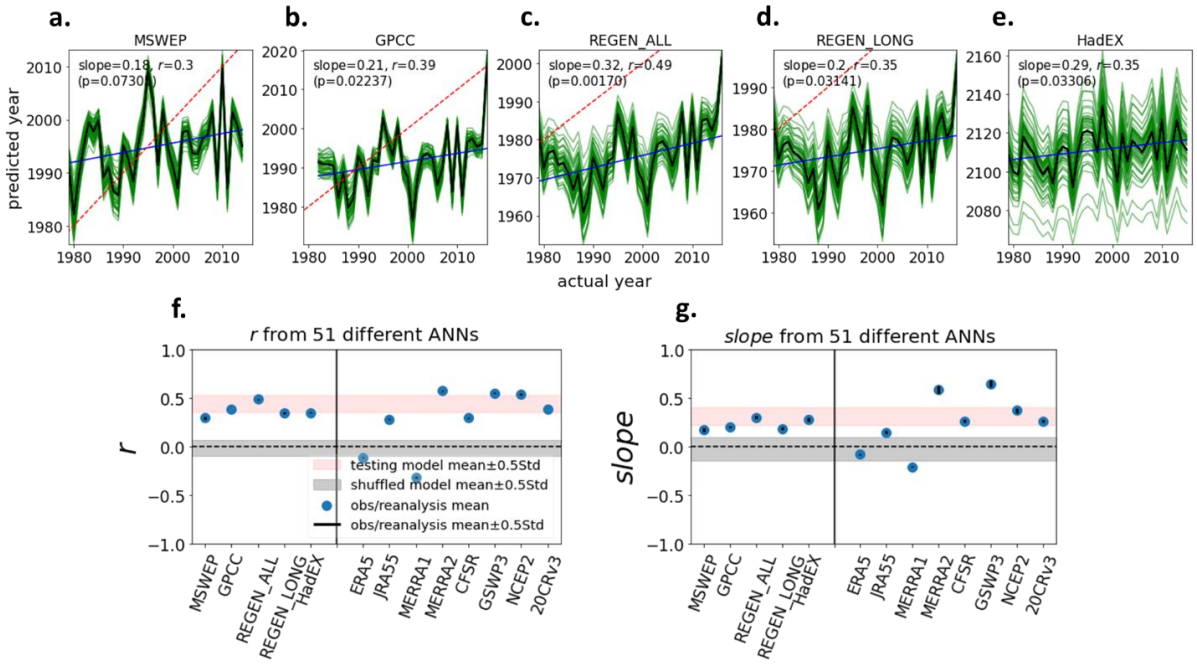

Figure 2.10: Same as Fig. 2.9 but using multimode mean to train the ANN.

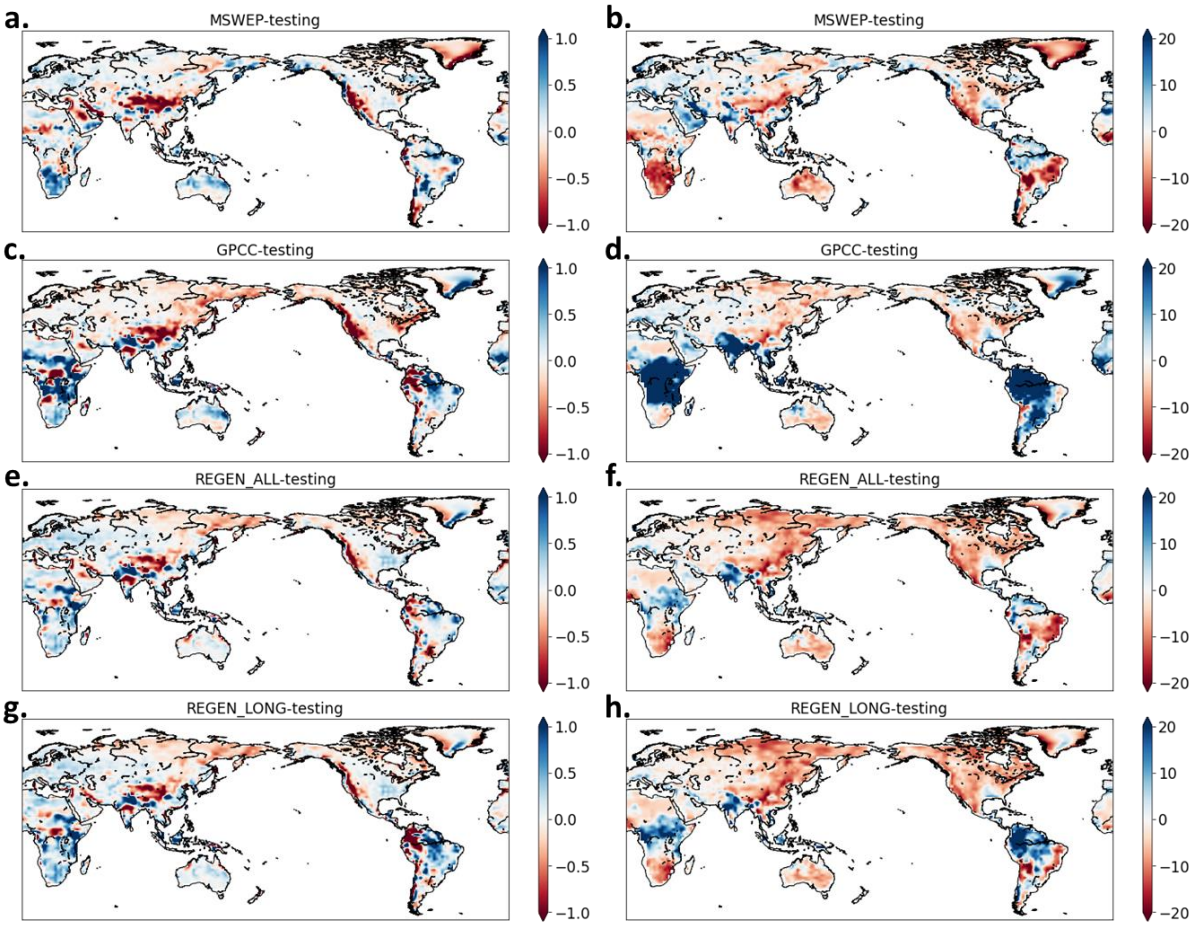

Figure 2.11: Differences of Rx1day and relevance between observations and models. (a,c,e,g) Difference of time average relevance (unit: years) between observations and testing data. (b,d,f,h) Difference of time average Rx1day (unit: mm/day) between observations and testing data. For testing data, an average from all testing models of 51 different ANNs with different training/testing sets was obtained.

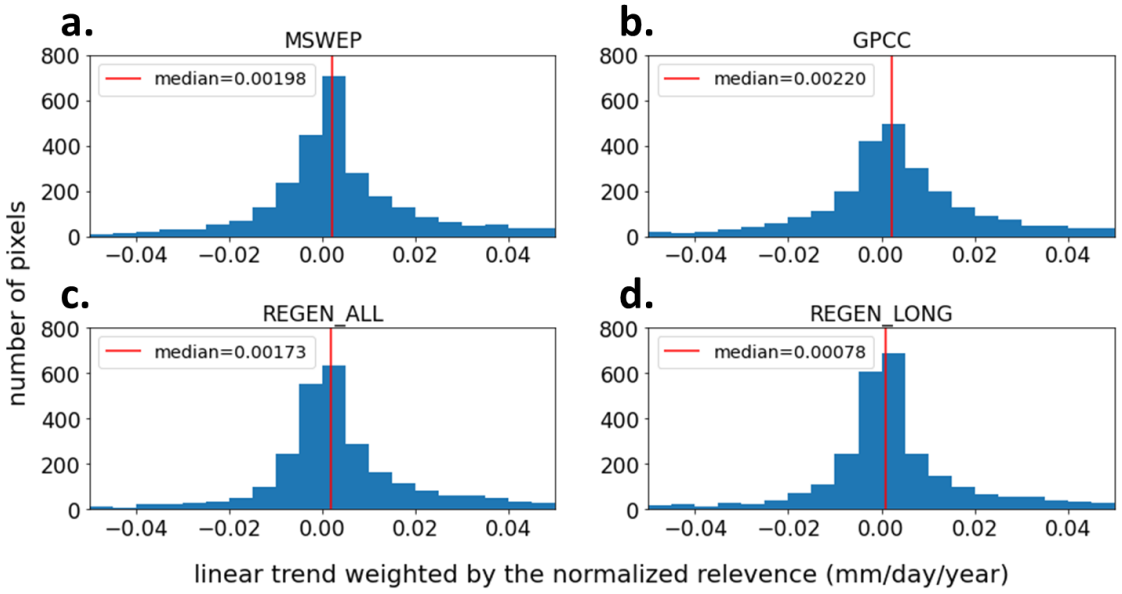

Figure 2.12: Histograms of the relevance-weighted linear trends (mm/day/year) in observed Rx1day for grid cells with positive relevance in Figure 1c. Bin width is 0.005 mm/day/year. Relevance value of each grid cell is first normalized by the global maximum and then used to weight the trend. Median of the distribution is depicted in a red vertical line. As shown by the median, datasets with a greater anthropogenic signal (GPCC and MSWEP, as shown in Fig. 2.5) have a higher number of grid cells with an increasing relevance-weighted trend in Rx1day compared to the datasets with a smaller anthropogenic signal (REGEN_ALL and REGEN_LONG).

Table 2.1: CMIP models and the ensemble variant used in this study.

	CMIP version	Model name	Ensemble variant
1	CMIP6	ACCESS-CM2	r1i1p1f1
2	CMIP6	ACCESS-ESM1-5	r1i1p1f1
3	CMIP6	CNRM-CM6-1-HR	r1i1p1f2
4	CMIP6	CNRM-CM6-1	r1i1p1f2
5	CMIP6	CNRM-ESM2-1	r1i1p1f2
6	CMIP6	CanESM5	r1i1p1f1
7	CMIP6	EC-Earth3-Veg	r1i1p1f1
8	CMIP6	EC-Earth3	r1i1p1f1
9	CMIP6	GFDL-CM4	r1i1p1f1
10	CMIP6	GFDL-ESM4	r1i1p1f1
11	CMIP6	HadGEM3-GC31-LL	r1i1p1f3
12	CMIP6	NM-CM4-8	r1i1p1f1
13	CMIP6	NM-CM5-0	r1i1p1f1
14	CMIP6	IPSL-CM6A-LR	r1i1p1f1
15	CMIP6	MIROC-ES2L	r1i1p1f2
16	CMIP6	MIROC6	r1i1p1f1
17	CMIP6	MPI-ESM1-2-HR	r1i1p1f1
18	CMIP6	MPI-ESM1-2-LR	r1i1p1f1
19	CMIP6	MPI-ESM2-0	r1i1p1f1
20	CMIP6	NorESM2-LM	r1i1p1f1
21	CMIP6	NorESM2-MM	r1i1p1f1
22	CMIP6	UKESM1-0-LL	r1i1p1f2
23	CMIP5	ACCESS1-3	r1i1p1
24	CMIP5	CanESM2	r2i1p1
25	CMIP5	CMCC-CESM	r1i1p1
26	CMIP5	CMCC-CM	r1i1p1
27	CMIP5	CNRM-CM5	r1i1p1
28	CMIP5	CSIRO-Mk3-6-0	r1i1p1
29	CMIP5	EC-EARTH	r1i1p1
30	CMIP5	GFDL-CM3	r1i1p1
31	CMIP5	HadGEM2-AO	r1i1p1
32	CMIP5	HadGEM2-CC	r1i1p1
33	CMIP5	HadGEM2-ES	r1i1p1
34	CMIP5	inmcm4	r1i1p1
35	CMIP5	IPSL-CM5A-LR	r1i1p1
36	CMIP5	IPSL-CM5A-MR	r1i1p1
37	CMIP5	IPSL-CM5B-LR	r1i1p1
38	CMIP5	MIROC5	r1i1p1
39	CMIP5	MIROC-ESM-CHEM	r1i1p1
40	CMIP5	MIROC-ESM	r1i1p1
41	CMIP5	MPI-ESM-LR	r1i1p1
42	CMIP5	MPI-ESM-MR	r1i1p1
43	CMIP5	MRI-CGCM3	r1i1p1
44	CMIP5	NorESM1-M	r1i1p1

Table 2.2: Observations and reanalysis used in this study. Starting year of the time period was chosen as 1979 (or the closest) to be consistent with satellite era. The final year of the analysis period was chosen as the latest year with data. Trend estimates are the global terrestrial area averaged Rx1day linear trend and the statistical significance, obtained by using the Theil-Sen estimator and modified Mann-Kendall trend test *Hamed and Rao* (1998), respectively.

	dataset	Time period considered	trend estimates		
			trend (at 99%)	slope (mm/day/yr)	p value
1	MSWEP	1979-2014	Increasing	0.07	1.7×10^{-5}
2	GPCP FDD 2018	1982-2016	No trend	0.03	0.38
3	REGEN_ALL	1979-2016	Increasing	0.06	6.5×10^{-8}
4	REGEN_LONG	1979-2016	Increasing	0.05	2.6×10^{-6}
5	ERA5	1979-2019	Increasing	0.07	6.2×10^{-11}
6	JRA55	1979-2017	No trend	0.02	0.072
7	MERRA2	1980-2017	Increasing	0.09	$< 2 \times 10^{-16}$
8	CFRS	1979-2017	Increasing	0.085	0.017
9	GSWP3	1979-2010	No trend	-0.018	0.41
10	NCEP2	1979-2019	No trend	0.003	0.8
11	20CRv3	1979-2015	Increasing	0.05	1×10^{-13}

CHAPTER 3

Emergent Constraint on Future Changes in the Tropical Atmospheric Circulation

[**Madakumbura, G. D.**, Norris, J., Thackeray, C., Po-Chedley, S., Ahmed, F., Hall, A. (in revision at *Nature Climate Change*). Emergent Constraint on Future Changes in the Tropical Atmospheric Circulation. preprint available at Research Square. `https://doi.org/10.21203/rs.3.rs-3908042/v1`]

Abstract

Intensification of the hydrological cycle manifests through a global increase in precipitation at a rate lower than the increase in water vapor, and a consequent weakening in the atmospheric tropical overturning circulation (ATOC). This circulation change shapes future precipitation patterns, but is highly uncertain across Earth System Models (ESMs), complicating efforts seeking to constrain projected changes in regional precipitation. Using two ESM ensembles, we present an emergent relationship between the ATOC's response to anthropogenic warming, and the ATOC's variability associated with interannual temperature anomalies. Models simulating the largest future ATOC weakening per degree warming also tend to simulate the largest weakening in association with an internally-generated warm anomaly. Observational estimates of ATOC sensitivity suggest that future ATOC weakening

due to climate change is likely larger than expected from a simple multimodel mean (from -1.41±1.06 %/K to -2.20±0.93 %/K). Lastly, we show how this enhanced ATOC weakening impacts regional precipitation patterns. These constrained circulation and precipitation estimates provide a better understanding of how tropical hydroclimate will respond to future warming and associated regional climate impacts.

3.1 Introduction

Anthropogenic climate change intensifies the global hydrological cycle (*Intergovernmental Panel on Climate Change*, 2022; *Allan et al.*, 2020; *Madakumbura et al.*, 2019). This intensification manifests as an increase in global mean precipitation of about 2-3%/K, a rate limited by radiative processes (*Allen and Ingram*, 2002). Water vapor also increases, at a rate of about 7%/K, in accord with the Clausius-Clapeyron relationship (*O'Gorman and Muller*, 2010)5. The difference between atmospheric moistening and precipitation change implies a decrease in the convective mass flux, through a weakening of the atmospheric tropical overturning circulation (ATOC) (*Held and Soden*, 2006; *Vecchi and Soden*, 2007). The weakening of the ATOC tends to make historically wet regions drier and historically dry regions wetter, thus altering the spatial pattern of future precipitation change from a wet-gets-wetter, dry-gets-drier pattern (*Seager et al.*, 2010; *Norris et al.*, 2019). Furthermore, this dynamical change in mean precipitation is the largest source of uncertainty in the regional patterns of future projections (*Bony et al.*, 2013). Therefore, constraining the response of the ATOC to future warming has significant societal and ecological implications.

Weakening of the ATOC can manifest in both the zonally asymmetric circulation component known as the Walker cell and the zonal mean circulation known as the Hadley cell (*Vecchi and Soden*, 2007). Earth System Models (ESMs) exhibit these circulation changes in future projections (*Vecchi and Soden*, 2007; *Duffy and O'Gorman*, 2023; *Fan and Dommenget*, 2024) and historical simulations with realistic climate forcings (*Chemke and Yuval*,

2023; *Chemke and Polvani*, 2019), though the magnitude of weakening varies across ESMs. Moreover, historical reanalysis estimates of ATOC trends have indicated both weakening (*Shrestha and Soden*, 2023) and strengthening (*Chemke and Polvani*, 2019), differences that may arise from factors such as reanalysis forcings biases and internal variability (*Shrestha and Soden*, 2023; *L'Heureux et al.*, 2013). Meanwhile, analysis of mechanistic drivers, based on moist static energy balance, have shown competing influences on anthropogenic changes in the ATOC. Gross moist stability (a metric of atmospheric stability), changes in the radiative and surface energy fluxes into the atmosphere, and advection of moisture and heat, all can have large contributions to the ATOC response, and each has a large ESM spread (*Duffy and O'Gorman*, 2023; *Fan and Dommenget*, 2024; *Chou et al.*, 2013). This bottom-up approach also suggests different dominant mechanisms of ATOC change in different regions (*Chadwick et al.*, 2013; *Chou et al.*, 2009; *Chou and Chen*, 2010). These gaps in mechanistic knowledge have hindered a comprehensive understanding of how the ATOC responds to climate change and, therefore, efforts to constrain the large ESM uncertainty in future ATOC changes (*Ma et al.*, 2018, 2020).

Changes in the ATOC can be associated with the overall pattern of surface temperature change. Uniform sea surface warming can weaken both the Walker and Hadley cells, but spatially non-uniform changes can dampen or enhance these circulation features (*Chadwick et al.*, 2013; *Ma et al.*, 2012; *Zhang et al.*, 2023). The latter is widely known as the sea surface temperature (SST) pattern effect. Changes to SST gradients can modulate the thermally driven components of the Walker and Hadley circulation (*Zhang et al.*, 2023; *Corvec and Fletcher*, 2017; *Gastineau et al.*, 2009). This pattern effect can also change the ATOC under internal variability, of which the dominant contributor is El-Nino Southern Oscillation (ENSO) (*Zhang et al.*, 2023). Recent work has implied that the hydrological sensitivity (HS) linked to ATOC under internal variability can be a surrogate of the ESM spread in HS under climate change (*Norris et al.*, 2022a). Disagreements in the SST pattern response to greenhouse gas forcing are likely the result of ESM structural differences (*e.g.*,

coupled model SST biases; *He and Soden* 2016 and convective parameterization; *Maher et al.* 2018). Therefore, understanding how the ESM spread under climate change and internal variability are related, has the potential to reduce such structural uncertainty in future ATOC projections.

Emergent constraints (ECs) are a common approach to reduce uncertainty in climate projections (*Hall et al.*, 2019; *Williamson et al.*, 2021; *Cox et al.*, 2018; *Williamson et al.*, 2018). The EC technique uses a physically based, statistically significant relationship between the climate change response and an observable analog from the historical climate, across an ensemble of ESMs. ECs can identify underlying mechanisms that link the ESM spread in a response to climate change to the spread in an analogous response to short-term variability, such as the seasonal cycle or the interannual variability. ECs have successfully constrained the snow albedo feedback (*Hall and Qu*, 2006), sea-ice albedo feedback (*Thackeray and Hall*, 2019), change in tropical precipitation extremes (*O'Gorman*, 2012), change in tropical ocean primary production (*Kwiatkowski et al.*, 2017), and equilibrium climate sensitivity (*Cox et al.*, 2018; *Williamson et al.*, 2018). Since SST pattern effects drive changes in the ATOC and tropical precipitation on both interannual and climate change timescales (*Zhang et al.*, 2023; *Norris et al.*, 2022a), we seek to develop an EC that links future, long-term changes in the ATOC to internal variability in the tropical overturning circulation. Our underlying hypothesis is that there are commonalities in the sensitivity of the ATOC to internally-generated tropical temperature anomalies, on the one hand, and the ATOC response to anthropogenic warming, on the other. Because of these commonalities, the realism of the simulated ATOC response to warming can be evaluated from observations of internal ATOC variability.

3.2 Data and Methods

3.2.1 CMIP5 and CMIP6 simulations

We use monthly mean precipitation, near-surface air temperature (tas), pressure velocity (ω), zonal and meridional winds, surface air pressure, and specific humidity data from 18 CMIP5 (*Taylor et al.*, 2012) and 31 CMIP6 (*Eyring et al.*, 2016) models (Supplementery Table 1, Figure 3.A.2). To examine the temperature-mediated changes due to climate change, we use Abrupt4xCO2 simulations. To represent the internal variability, pre-industrial control (piControl) simulations are used.

To investigate if the emergent relationship identified in this study depends on the ocean-atmospheric coupling and temperature gradients, we use tas and ω from CMIP historical and Atmospheric Model Intercomparison Project (AMIP) simulations (for the period 1979-2014). Historical simulations use atmosphere-ocean coupled ESMs and incorporate realistic historical natural forcings (volcanic eruptions and solar variability), and human-induced forcings, such as CO2 concentration, aerosols, and land use changes. The AMIP simulations are atmosphere-only simulations using prescribed observed sea surface temperature and sea ice concentrations, while other forcings are similar to the historical simulations.

Historical simulations are also used for the cross-validation of the statistical learning-based estimation of the $\overline{\omega^+}$ (see the section Estimation of the simulated and observed ω^+ below). For this, tas and sea level pressure (slp) data from CMIP6 historical simulations are used.

3.2.2 Reanalysis and observations

ω and slp data from three reanalysis products are used in this study; NOAA/CIRES/DOE 20th Century Reanalysis (20Crv3) (*Slivinski et al.*, 2019) for the period 1900-2014, ERA5 Reanalysis (*Hersbach et al.*, 2020) for the period 1940-2014, and MERRA2 Reanalysis (*Gelaro*

et al., 2017) for the period 1980-2014. Observed tas is obtained from the Berkeley Earth Land/Ocean Temperature Record (*Rohde and Hausfather*, 2020).

3.2.3 Decomposition of the thermodynamic and dynamic components of precipitation

Following refs. *Norris et al.* (2019); *Seager and Henderson* (2013); *Norris et al.* (2022b), the atmospheric moisture budget is decomposed as below.

$$P - E = MC \tag{3.1}$$

where P is the Precipitation, E is the Evaporation and MC is the Moisture Flux Convergence. The MC can be written as Eq. 3.2 below.

$$MC = -\frac{1}{\rho_w g}\nabla . \int_0^{p_s} (uq)dp \tag{3.2}$$

here u is the horizontal winds, q is the specific humidity and p is the pressure. ρ_{w} and g are the density of water and the gravitational constant, respectively. ∇ is the gradient operator and $\int_0^{p_s} ()dp$ is the pressure integral from the surface p_s to the top of the atmosphere. MC can be further decomposed as below.

$$MC \approx -\frac{1}{\rho_w g}\nabla . \int_0^{p_s} (\overline{u} + \Delta u)(\overline{q} + \Delta q)dp \tag{3.3}$$

where $\overline{u}$, $\overline{q}$ are the piControl monthly climatology of u and q, respectively. Δ denotes the change from the monthly climatology. This allows us to define the thermodynamic change, which is associated with the changes in the q as

$$P(TH) = -\frac{1}{\rho_w g}\nabla . \int_0^{p_s} (\overline{u}\Delta q)dp \tag{3.4}$$

The dynamical change is associated with the changes in the u and can be written as

$$P(DY) = -\frac{1}{\rho_w g}\nabla . \int_0^{p_s} (\overline{q}\Delta u)dp \tag{3.5}$$

3.2.4 Estimation of the Walker and Hadley circulation

To represent the Walker circulation, the zonal streamfunction (Ψ_Z) (*Yu and Zwiers*, 2010; *Yu et al.*, 2012) is calculated as

$$\Psi_Z = 2\pi a \int_0^p u_D \frac{dp}{g} \tag{3.6}$$

where u_{D} is the divergent component of the zonal wind and a is the radius of the earth. The average zonal wind for the latitudinal band 5°S and 5°N is used. The Hadley cell is estimated using the meridional mass streamfunction (Ψ_M) is calculated as

$$\Psi_M = \frac{2\pi a cos\phi}{g} \int_0^p v \; dp \tag{3.7}$$

where is the ϕ latitude and v is the zonal mean meridional wind.

3.2.5 Estimation of the simulated and observed ω^+ using pressure velocity

Following ref. *Vecchi and Soden* (2007), ω^+ is calculated as the upward monthly pressure velocity, over all model grid points that have ascending motion in the tropics (30°S-30°N). Considering the ESM uncertainty that spans the whole troposphere, the vertical average of ω^+ from surface to 200hPa value of ($\overline{\omega^+}$) is used in the analysis. For the emergent relationship, the tropical average $\overline{\omega^+}$ and surface temperature ($\overline{T}$) are calculated for each year. The $\overline{\omega^+}$ normalized by the temperature change is estimated as the regression coefficient between $\overline{\omega^+}$ and $\overline{T}$. This provides sensitivity of $\overline{\omega^+}$ to temperature change under climate change ($\overline{\omega_{CC}{}^+}$) and the internal variability ($\overline{\omega_{IV}{}^+}$).

For historical and AMIP simulations, first, a trend removal is conducted using a lowess

smoothing and the $\overline{\omega_{IV}{}^{+}}$ is calculated using detrended historical and detrended AMIP $\overline{\omega^{+}}$ and $\overline{T}$ (Figure 3.A.5).

3.2.6 Estimation of the observed ω^{+} using tas and psl

Uncertainties in the representation of forced changes of ATOC in reanalysis could affect the observed $\overline{\omega_{IV}{}^{+}}$ estimates using reanalysis. For an independent estimation of $\overline{\omega_{IV}{}^{+}}$, a statistical learning model of $\overline{\omega^{+}}$, using piControl tas and slp, is developed. This is motivated by 1) the strong link between slp and ATOC (*Chemke and Yuval*, 2023), 2) the availability of robust observational records for tas and slp, 3) the robustness of the climate change signal in tas and slp (*Hawkins et al.*, 2020; *Gillett et al.*, 2003). Having a robust climate change signal in the predictor variables allows a robust estimation of the observed internal variability component, which will be ultimately used with the trained statistical learning model to estimate the observed $\overline{\omega_{IV}{}^{+}}$. Following previous machine learning-based approaches to disentangle climate change and internal variability (*Madakumbura et al.*, 2021; *Barnes et al.*, 2020; *Sippel et al.*, 2020; *Po-Chedley et al.*, 2022), we use partial least square (PLS) regression to model the ESM simulated tropical average annual $\overline{\omega^{+}}$ timeseries, using spatial maps of annual mean tas and slp of each model year as predictors. Using the PLS inferred timeseries of $\overline{\omega^{+}}$, the sensitivity to internal variations in temperature (i.e., the x-axis of the emergent relationship), $\overline{\omega_{IV}{}^{+}}_{\text{modeled}}$, is calculated and compared with the actual value of $\overline{\omega_{IV}{}^{+}}$ (Figure 3.A.6). The number of PLS components was selected by using historical CMIP6 simulations, as this is analogous to the observational record. Therefore, historical simulations essentially serve as out-of-sample testing data. Following ref. (*Hawkins et al.*, 2020), the internal variability component of the historical simulations and observations are estimated by removing the low-frequency component, estimated with a lowess filter. As $\overline{\omega_{IV}{}^{+}}$ for each model should be the same for piControl and historical simulations (Figure 3.A.5), the $\overline{\omega_{IV}{}^{+}}_{\text{modeled}}$ from historical simulations are compared with the corresponding $\overline{\omega_{IV}{}^{+}}$. The number of PLS components is selected by considering the r value and the mean squared

error between $\overline{\omega_{IV}{}^{+}}_{\text{modeled}}$ and $\overline{\omega_{IV}{}^{+}}$ (Figure 3.A.6). Finally, the observed internal variability components of tas and psl are fed to the selected PLS model and observed $\overline{\omega_{IV}{}^{+}}$ are estimated (Figure 3.3).

3.2.7 Estimation of the uncertainty of the observationally constrained estimate

To obtain the uncertainty by taking the errors in both the x and y-axis variables of the emergent relationship, a bootstrapping-based approach is used following ref. (*Simpson et al.*, 2021). The emergent relationship can be written as

$$\Delta y_i = \alpha + \beta x_i + \epsilon(i) \tag{3.8}$$

where x is the present-day quantity, Δy is the future change, α and β are the regression coefficient and the intercept of the linear fit, and ε is the residuals. i refers to individual model data points. ε has a component arising from the internal variability (ε_{IV}) and a component due to the intermodel differences that are not explained by the emergent constraint (δ).

$$\varepsilon = \varepsilon_{IV} + \delta \tag{3.9}$$

The true values of Δy ($\Delta\overline{y}$) and x ($\overline{x}$) can be written as

$$\Delta\overline{y}_i = \alpha + \beta\overline{x}_i + \epsilon_{IV}(i) + \delta(i) \tag{3.10}$$

The variance (σ) of the modeled Δy can be partitioned into the component that is explained by the emergent relationship (σ^2_{EC}) and the remainder (σ^2_{ε}). σ^2_{ε} include contributions from internal variability (σ^2_{IV}) and the intermodel differences that are not explained by the EC (σ^2_{δ})

$$\sigma^2(\Delta y) = \sigma^2_{EC} + \sigma^2_{IV} + \sigma^2_{\delta} \tag{3.11}$$

To obtain the constrained value (Δy_{E})) from the observations (x_{E})

$$\Delta y_E = \alpha + \beta x_E + \epsilon_{IV} + \delta \tag{3.12}$$

To obtain the constrained distribution of Δy_{E}, Probability density functions (PDFs) of each component of the right-hand side in eq. (4) are constructed. 1000 combinations of α and β are estimated with distinct total least square regressions by bootstrapping with replacement. For $\overline{x}_E$, the PDFs are created as normal distributions centered around the observational estimates, with the standard deviation σ_x that represents the internal variability. σ_x is estimated as the error in x. To account for the internal variability (ε_{IV}) and other forced contributions that are unrelated to the emergent constraint (δ), $\Delta y_{\mathrm{IV}} + \delta_E$ is estimated as the $\sigma_\varepsilon^2 - \beta^2\sigma_x^2$. This results in $1000^3 = 1$ billion values of Δy_{E}. The constrained mean and the spread (± 1 standard deviation) are calculated from this distribution.

3.2.8 Constraining the regional pattern of precipitation change

Precipitation change in abrupt4xCO2 (Figure 3.1a) across ESMs is regressed on $\overline{\omega_{CC}{}^+}$, for each model grid cell. 100 regression models for each grid cell are created by sampling with replacement. For each of these regression models, we construct a distribution of constrained precipitation change by using 1000 randomly sampled values from the constrained $\overline{\omega_{CC}{}^+}$ distribution, resulting in 105 constrained values for each grid cell. The constrained mean and the spread are calculated from these values. To obtain the comparable original spread (Figure 3.A.4), the above procedure is repeated with 1000 randomly sampled values from unconstrained $\overline{\omega_{CC}{}^+}$ distribution.

3.2.9 Normalizing variables by the change in temperature

The interannual variability of the target variable is regressed onto that of the global mean near-surface temperature. The resulting regression coefficient is then used as the measure of

the variable normalized by the change in temperature. To calculate uncertainty, the process is repeated with random sampling using replacement.

3.3 Results

3.3.1 Precipitation change under climate change and internal variability

To isolate the circulation-mediated precipitation response under internal variability and climate change, we decompose precipitation change and variability into its thermodynamic and dynamic components. We use 49 ESMs from Phases 5 and 6 of the Coupled Model Intercomparison Project (CMIP5 and 6). The future signal is derived from simulations with abrupt quadrupling of atmospheric carbon dioxide from pre-industrial values (abrupt-4xCO2).

Future ensemble-mean changes in total precipitation, and its thermodynamic and dynamic components, are shown in Figure 3.1a,c,e. The thermodynamic component shows the wet-gets-wetter, dry-gets-dryer pattern (*Held and Soden*, 2006). The total precipitation response (Figure 3.1a) deviates significantly from this thermodynamic change due to a large and dominant contribution from the dynamic component. This appears to be associated with ATOC weakening (*Bony et al.*, 2013): an increase in precipitation in the descending branch of the Walker circulation over the central to eastern equatorial Pacific, and a decrease in precipitation in the ascending branches of the Walker circulation over Africa, the Maritime continent, and South America. The ensemble-mean patterns in Figure 3.1 mask significant diversity across individual ESMs, and the ESM spread of the globally averaged total precipitation response is dominated by the dynamical contribution (Figure 3.A.1) and therefore, the associated changes in the ATOC.

To investigate whether the spatial pattern of change in precipitation is similar under internal variability, we also decompose its precipitation anomalies into thermodynamic and dynamic components (Figure 3.1b,d,f). The piControl simulations from which these are calculated have no changes in external forcing and therefore only represent the precipita-

tion anomalies associated with internally-generated variations in climate. Total precipitation anomalies are almost identical to the dynamical component, and the thermodynamic component is nearly negligible. The dynamic component has a striking resemblance to that of climate change (cf. Figure 3.1e,f). The dynamical component of internal variability reflects the eastward shift and the weakening of the Walker circulation under El Niño, with decreased precipitation over the ascending branch of the Walker circulation. The similarities between future warming and internal variability of both the multimodel mean (Figure 3.1a.b) and the ESM spread (Figure 3.A.1a,f) are consistent with the emergent relationship documented in *Norris et al.* (2022a). Specifically, that study showed a relationship between HS under ENSO versus climate change. These considerations motivate us to analyze the underlying processes of the dynamical component under both climate change and internal variability.

3.3.2 Change in circulation under climate change and internal variability

We first examine the sensitivity of the Walker and Hadley Circulations to future warming and internal temperature variability (Figure 3.2). Note that in this and all subsequent discussions of the internal variability case, we emphasize internal variability's warm phase, for simplicity and because of its obvious analogy to climate change. However, all of our arguments apply (in reverse) to the cold phase as well, and of course the cold anomalies contribute equally to the statistics presented in all figures. The multimodel mean zonal (Walker) circulation response at the equator to climate change (Figure 3.2a) bears a strong resemblance to that of internal variability (Figure 3.2b), as previous studies have noted (*Vecchi and Soden*, 2007; *Bayr et al.*, 2014). Under climate change and the warm phase of internal variability (i.e., dominated by El Niño), climatologically ascending regions (Africa, Maritime continent, and South America) experience a descending anomaly, whereas climatologically descending regions (West Indian Ocean, Pacific Cold tongue, and Atlantic Ocean) experience an ascending anomaly. This indicates a weakening and eastward shift of the Walker circulation. The ESM spread shows a remarkably similar pattern between climate change and internal variability, with the largest

spread over the ascending branches of the Walker Cells. This suggests that the strength of an individual model's Walker circulation response under climate change, shaped by structural and parametric choices, can be predicted from that model's internal variability.

The Hadley cell response exhibits a complex interplay of similarities and differences between climate change and internal variability (Figure 3.2e-f). A similarity is particularly evident in the weakening in the Northern Hemisphere. Over the Southern Hemisphere (SH), Hadley Cell strengthening is seen in the warm phase of internal variability, but the climate change response shows both a weakening (in the deep tropics) and a strengthening (around 15°S). The strengthening of the Hadley cell under warm phases of internal variability can be linked to atmospheric-ocean coupling (*Chemke*, 2022). As with the Walker Circulation, the ESM spread (Figure 3.2g-h) shows very similar patterns between the two responses, particularly over the rising Hadley Cell branches in both hemispheres. Thus the patterns of the ESM spread in circulation response to climate change (Figure 3.2c,g) and internal variability (Figure 3.2d,h), are very similar, especially in the rising branches of both Walker and Hadley circulations. The fact that the same outcome can be seen in these two orthogonal ATOC metrics encourages us to define an aggregated, representative metric of the ATOC, which may be used in an emergent relationship.

3.3.3 An emergent constraint on ATOC

The upward monthly atmospheric vertical velocity, averaged over all grid points that have ascending motion in the tropics (30°S-30°N), denoted here as ω^+, has been widely used to measure the ATOC response to climate change (*Vecchi and Soden*, 2007; *Bony et al.*, 2013; *Merlis*, 2015). Here we use the vertical average of ω^+ over the troposphere (surface to 200hpa), $\overline{\omega_{CC}{}^+}$, as the large values of ESM uncertainty in Figure 3.2 span the whole troposphere. The sensitivity of $\overline{\omega_{CC}{}^+}$ to global-mean temperature under climate change ($\overline{\omega_{CC}{}^+}$) and internal variability ($\overline{\omega_{IV}{}^+}$) are examined. A strong majority (43 out of 49) of ESMs show a negative value for $\overline{\omega_{CC}{}^+}$, indicating weakening of the ATOC under climate

change, with a mean±1 standard deviation of -1.41±1.06 %/K. The slightly positive values seen in the rest of the models can arise from an increase in the height of convective outflow with warming, and do not necessarily signify a strengthening of ATOC (*Chadwick et al.*, 2013). Looking across generations of ESMs, the models produced by Goddard Institute for Space Studies (GISS) and Model for Interdisciplinary Research on Climate (MIROC) are consistently among the ESMs with the least and most negative $\overline{\omega_{CC}{}^{+}}$ values, respectively, in CMIP6, CMIP5 (Figure 3.A.2) and CMIP3 (*Vecchi and Soden* 2007, their Figure 4). The variables $\overline{\omega_{CC}{}^{+}}$ and $\overline{\omega_{IV}{}^{+}}$ are strongly correlated across 49 ESMs (Figure 3.3; r=0.73). This relationship is apparent in both CMIP5 (r=0.83) and CMIP6 (r=0.74), which enhances our confidence in its robustness (*Hall et al.*, 2019).

ESMs show both positive and negative values for $\overline{\omega_{IV}{}^{+}}$. As the Walker circulation weakens during the warm phases of internal variability (Figure 3.2a-b), these positive values could result from the strengthening of the SH Hadley Cell (Figure 3.2f). Models that show the least weakening of the ATOC under climate change show the largest strengthening under the warm phase of internal variability. Observational estimates of $\overline{\omega_{IV}{}^{+}}$, based on de-trended reanalyses vertical velocity, provide central estimates of -2.38, -1.35, and -0.95 %/K for 20Crv3, MERRA2, and ERA5, respectively (Methods). As reanalyses vertical velocity is essentially model derived and may have biases in the ATOC response (*Chemke and Polvani*, 2019; *Mitas and Clement*, 2005), we also estimate $\overline{\omega_{IV}{}^{+}}$ using observed surface temperature and reanalysis sea level pressure data, which is more directly constrained by observations (Methods). Estimates of $\overline{\omega_{IV}{}^{+}}$ produced with this method match with the reanalysis vertical-velocity-based ATOC estimates reasonably well (dashed/dotted vertical lines in Figure 3.3). The emergent constraint suggests a $\overline{\omega_{CC}{}^{+}}$ value of -2.20±0.93 %/K, signifying a 55% greater weakening of the ATOC than the mean of the unconstrained ensemble. This also represents a 12% decrease in model uncertainty. Thus, the original ESM spread is substantially shifted down and slightly constrained.

A number of factors may contribute to changes and variability in the ATOC, producing

this emergent constraint (*Ma et al.*, 2018). ESM cross correlation between $\overline{\omega_{CC}{}^{+}}$ and pi-Control meridional and zonal mass stream function sensitivities indicate that the descending branch of the Pacific Walker cell and SH Hadley Cell, each has a large contribution to the emergent relationship (p value<0.01, Figure 3.A.3a-b). Further cross-correlation between $\overline{\omega_{CC}{}^{+}}$ and climatological ω^{+} over the tropics also points to intermodel variations in climatological Southern Hemisphere Hadley cell as a source of future model spread (Figure 3.A.3c). Further examination of this figure shows significant (p value<0.01) cross-correlation over the southeastern Pacific, including subtropical dry zones. As $\overline{\omega_{CC}{}^{+}}$ is calculated from ascending motion, this high correlation could be related to varying degrees of the double-Intertropical Convergence Zone (ITCZ) bias (*Tian and Dong*, 2020; *Hwang and Frierson*, 2013). A "double ITCZ" creates a spurious intrusion of the tropical rain belt into the southeastern Pacific and is one of the largest sources of ESM bias and uncertainty in precipitation and ascending motion in this region (*Tian and Dong*, 2020). The southeastern Pacific also experiences an intrusion of warm pool convection from the west during the warm phase of internal variability (Figure 3.1b), with substantial ESM uncertainty (Figure 3.A.3f). These results indicate that while the weakening of the ATOC under climate change was previously shown to be dominated by the response of the Walker Circulation (*Vecchi and Soden*, 2007), the uncertainty in the SH Hadley Cell response also contributes to a large ESM spread in the ATOC response.

3.4 Implications and future directions

Better understanding and constraining the evolution of the ATOC under climate change can help improve projections of regional precipitation change. We illustrate this by regressing the precipitation response (Figure 3.1a) against the unconstrained and constrained distributions of $\overline{\omega_{CC}{}^{+}}$, across ESMs (Methods). The difference between these two metrics (the mean change in precipitation sensitivity due to adjusted ATOC) is shown in Figure 3.4a. Notably, this implies a substantial reduction (larger than 20%) in the expected wetting across the

maritime continent (Figure 3.4a,b), a region with appreciable ESM uncertainty (Figure 3.1a, Figure 3.A.1a). The constrained mean indicates a stronger weakening by the dynamical component, resulting in only a slight increase in precipitation. A substantial change is also apparent over the Amazon (Figure 3.4c). The original multimodel mean shows a large drying in the Amazon, which is muted when the ATOC is constrained. These regions also show a reduction (larger than 10%) in the ESM spread (Figure 3.A.4). Among the other regions with noticeable change, strengthening in the projected drying can be seen in West Africa and Central America (Figure 3.4d,e). The above regions are either biodiversity hotspots (*Myers et al.*, 2000; *Costello et al.*, 2022) or population hotspots, or both. Therefore, constrained change in future precipitation can provide valuable information towards habitat conservation planning and is also crucial for climate change adaptation strategies.

Another implication of constraining the ATOC is to provide a clearer picture of the El Niño-like warming under climate change (*Dong et al.*, 2021), and its implications. Weakening of the ATOC, specifically the Walker circulation, can warm the Pacific cold tongue region through the Bjerknes feedback (*Sohn et al.*, 2016). Increased warming in the tropical eastern Pacific can also create a positive cloud feedback, in which east Pacific warming leads to a decrease in the low-level stratus cloud deck off the west coast of South America, and more solar radiation and warming (*Ma et al.*, 2018). A more El Niño-like warming would cause changes in ENSO characteristics, increased frequency of extreme El Niño and La Niña events, and their associated global impacts, particularly on climate extremes (*Cai et al.*, 2015; *Zheng et al.*, 2016). Based on the emergent constraint presented in this study, examining the extent to which the mean state is becoming El-Niño-like is a potential future research avenue, with great socioeconomic and ecological importance, considering the far-reaching impacts of ENSO teleconnections (*Yeh et al.*, 2018).

Clues as to the fundamentally coupled origin of the model biases that produce the emergent relationship presented here can be seen in estimates of $\overline{\omega_{IV}{}^{+}}$ in various types of ESM configurations. Estimates of $\overline{\omega_{IV}{}^{+}}$ using historical simulations from atmosphere-ocean coupled

ESMs produce similar results as piControl simulations (Figure 3.A.5). However, atmosphere-only historical simulations, with prescribed SST and sea ice forcings (AMIP, see Methods), do not produce similar $\overline{\omega_{IV}{}^{+}}$ as piControl. Historical simulations exhibit SST biases due to atmosphere-ocean coupling, similar to the PiControl simulations, whereas the AMIP simulations do not. This indicates that the model biases that contribute to the emergent relationship are possibly related to coupled atmospheric and oceanic processes, and are not purely atmospheric in origin. Examination of mechanistic links between SST patterns and ATOC is an opportunity for future research from an ESM development perspective.

Observational uncertainty of ATOC sensitivity under internal variability can have a major effect on constrained estimates. While reanalysis products are the best available estimates for the observed ATOC, previous studies have indicated that the forced changes in the overturning circulation in some reanalyses are flawed due to biases in the forcings (*Chemke and Polvani*, 2019; *Mitas and Clement*, 2005). Surface pressure and temperature observations provide a similar constraint on ATOC changes, but alternate observations of the ATOC (*e.g.*, radiosonde data and satellite measurements) should also be employed to verify that this constraint is robust to a range of independently-derived observational indices. With these future directions, the emergent relationship identified in this study provides a pathway to ESM developments that could result in more robust regional projections of the intensification of the hydrological cycle.

Acknowledgements. We acknowledge the World Climate Research Programme's Working Group on Coupled Modelling, which is responsible for CMIP, and we thank the climate modelling groups for producing and making available their model output. We also thank the Earth System Grid Federation (ESGF) for archiving the data and providing access, and various funding agencies who support CMIP and ESGF. We acknowledge support from the Regional and Global Model Analysis Program for the Office of Science of the U.S. Department of Energy through the Program for Climate Model Diagnosis and Intercomparison.

3.5 Figures

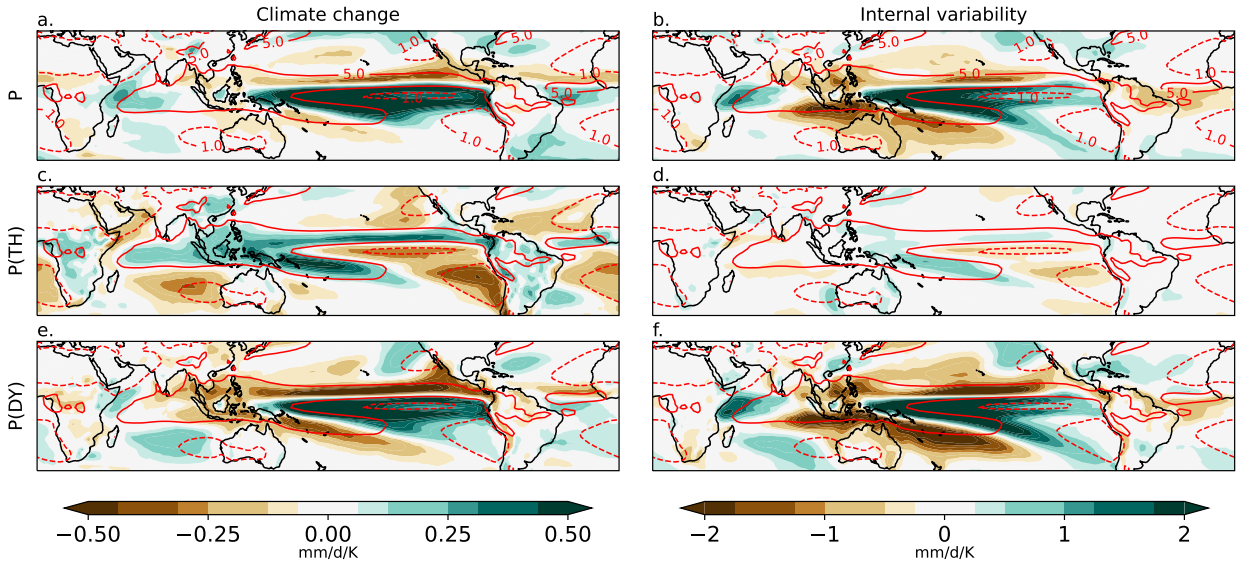

Figure 3.1: Multimodel mean precipitation change under climate change and internal variability. Total precipitation change (a,b), thermodynamic component of precipitation change (c,d) and the dynamic component of precipitation change (e,f). Climate change components (a,c,e) are calculated using the difference between abrupt-4xCO2 and piControl simulations while the internal variability components (b,d,f) are calculated using the interannual variability of piControl simulations. Red contours represent the multimodel mean annual mean precipitation from piControl simulations. Dashed and straight contours represent values 1 and 5 mm/day, to indicate climatologically dry and wet regions, respectively. Values are normalized by the change in temperature.

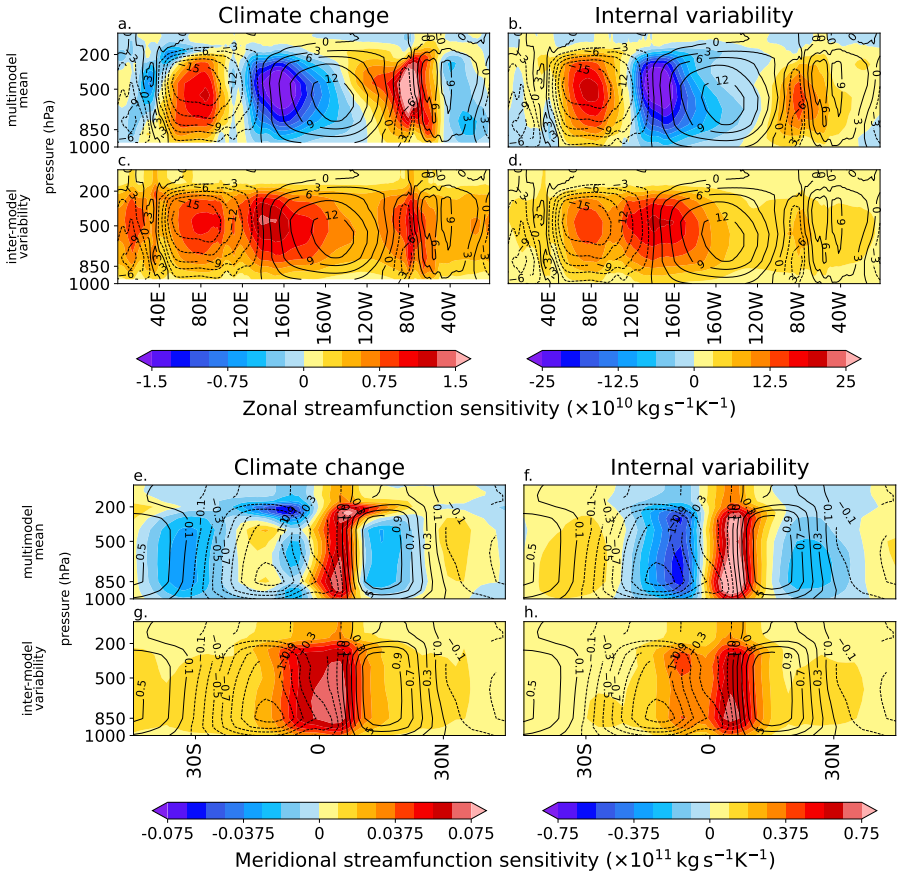

Figure 3.2: Sensitivity of the Walker and Hadley circulations to future warming and internal temperature variability. The sensitivity of the Walker circulation is represented using the zonal mass stream function (x10^{10} kg s^{-1} K^{-1}, 5°S-5°N) (a-d). The sensitivity of the Hadley circulation is represented by the meridional mass stream function (x10^{9} kg s^{-1} K^{-1}) (e-h). Multimodel mean (a-b,e-f) and model spread, calculated as the standard deviation across models (c-d,g-h). Climate change components (a,c,e,g) are calculated using abrupt-4xCO2 simulations and the internal variability components (b,d,f,h) are calculated using piControl simulations. Contours represent the climatological value, calculated as the multimodel mean of the piControl (x10^{10} kg s^{-1} for a-d and x10^{9} kg s^{-1} for e-h). Values are normalized by the change in surface temperature.

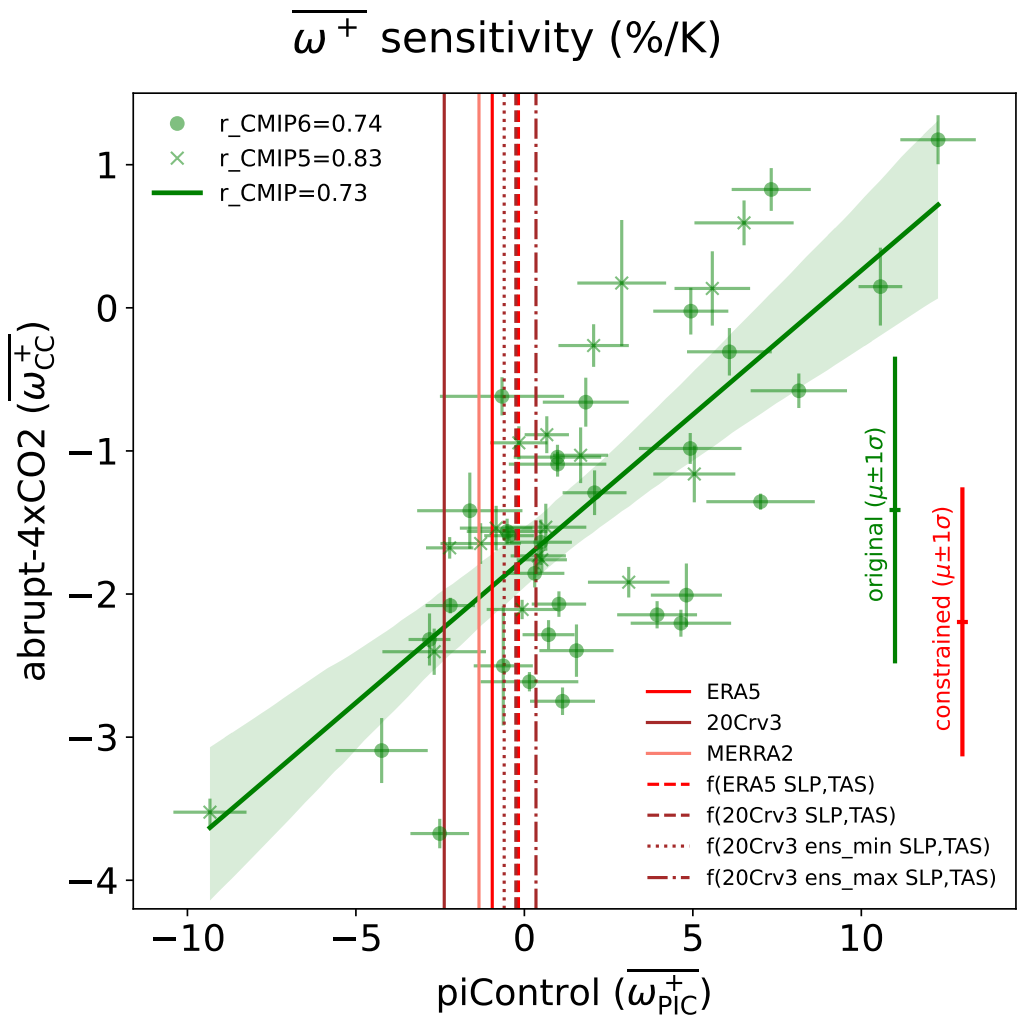

Figure 3.3: Emergent constraint on the atmospheric overturning circulation. The emergent relationship between the sensitivity of to ω^+ climate change ($\overline{\omega_{CC}{}^+}$, y-axis) and internal variability ($\overline{\omega_{IV}{}^+}$, x-axis), normalized by the change in temperature (%/K). Each dot represents a different ESM, and x and y error bars represent the ±1 standard deviation. Solid vertical lines represent the observed historical estimates calculated using various reanalysis datasets. Dashed vertical lines represent the observed historical estimates calculated using observed sea level pressure and surface temperature, and statistical learning (Methods). The green and red lines on the right represent the unconstrained and constrained 66% prediction intervals derived following *Simpson et al.* (2021). Best fit line (green) and the 95% confidence interval (shaded) are shown.

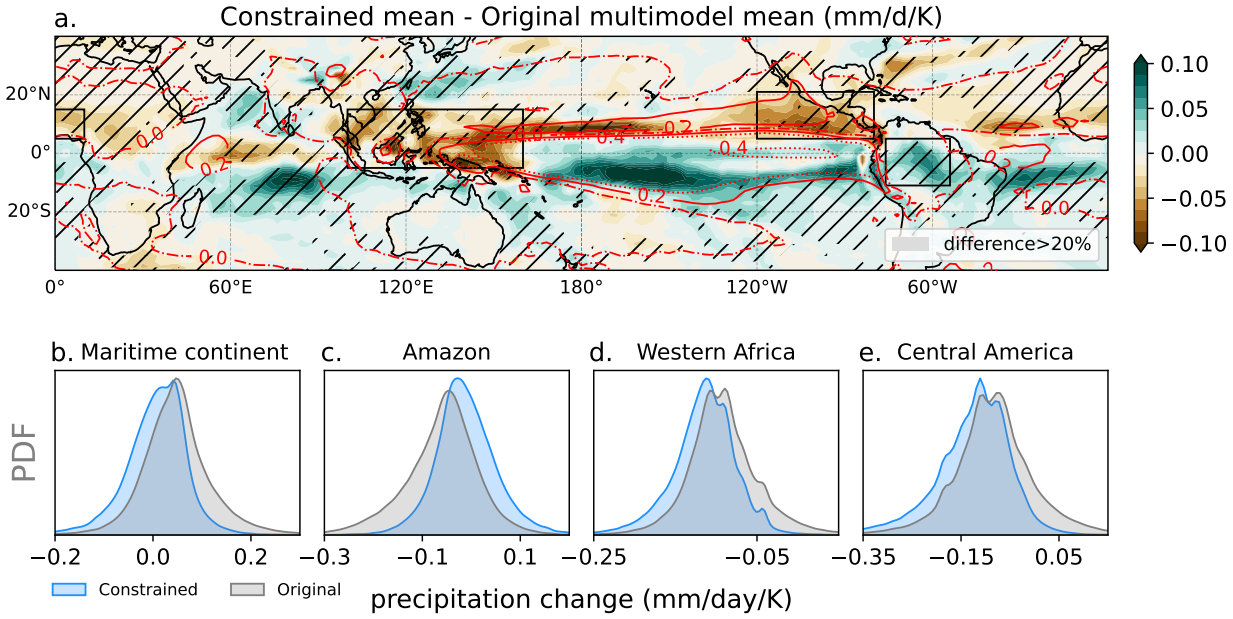

Figure 3.4: Resulting impact of constrained ATOC on future changes in regional precipitation. Difference between constrained precipitation change and the original multimodel mean of the precipitation change (a) (mm/d/K). Hatching indicates changes larger than ±20%. Boxes represent the Maritime Continent (5°S-15°N,100°E-160°E), Amazon (11°S-5°N,76°W-54°W), Western Africa (5°N-15°N,0°E-54°E) and Central America (5°N-21°N,120°W-80°W). Distributions of area average values over the Maritime continent (b), Amazon (c), Western Africa (d) and Central America (e), for original and constrained values, are shown.

3.A Supplement

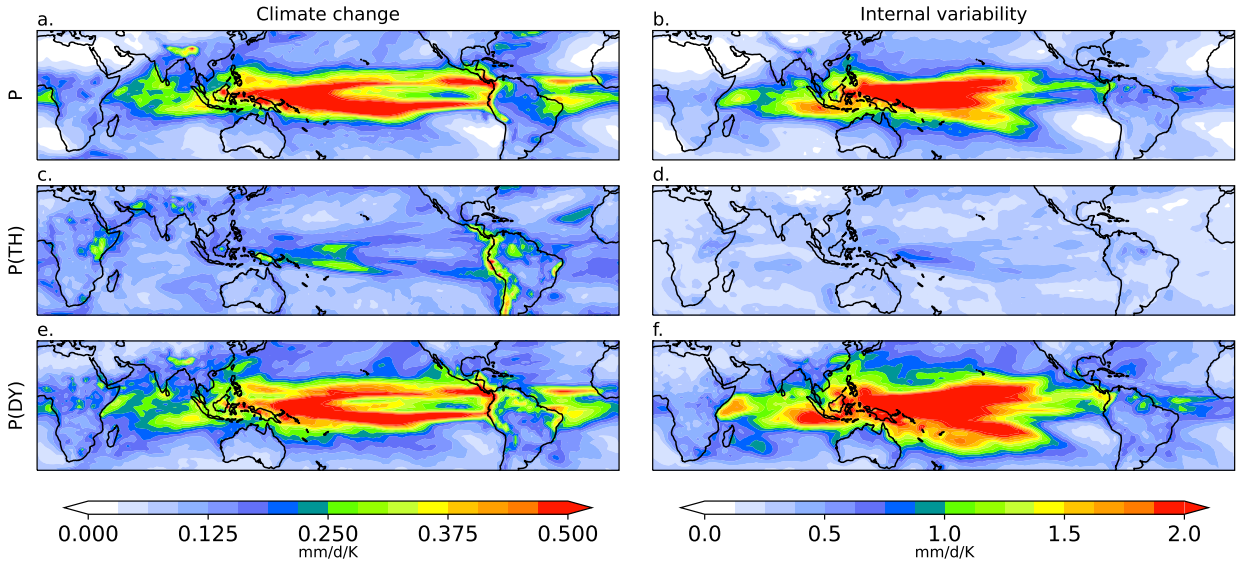

Figure 3.A.1: Same as Figure 3.1 but for the model spread, calculated as the inter-model standard deviation.

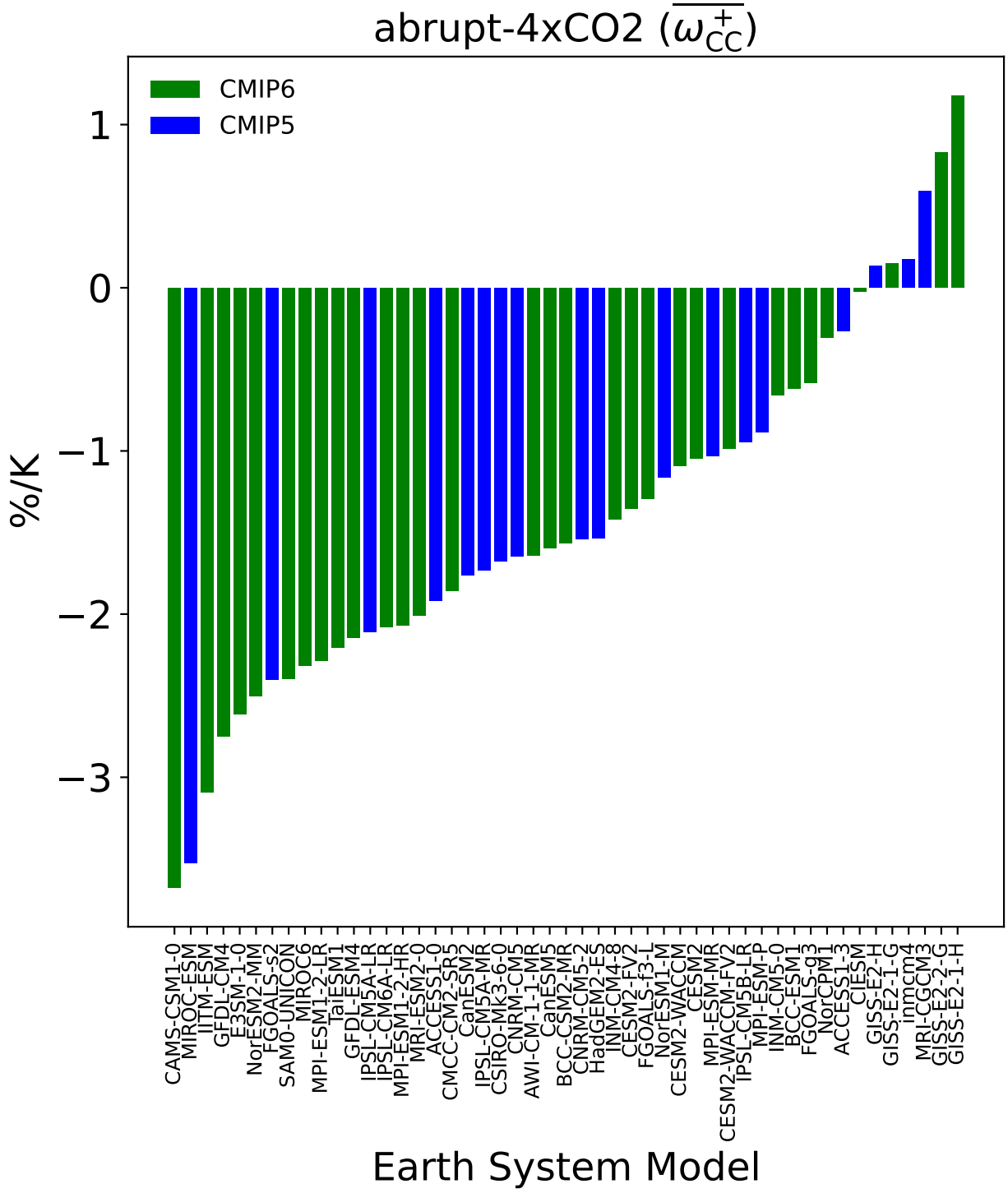

Figure 3.A.2: ESM values of the $\overline{\omega_{CC}{}^{+}}$, calculated using Abrupt-4xCO2 simulations, in descending order. Blue values represent the CMIP5 models and green values represent the CMIP6 models.

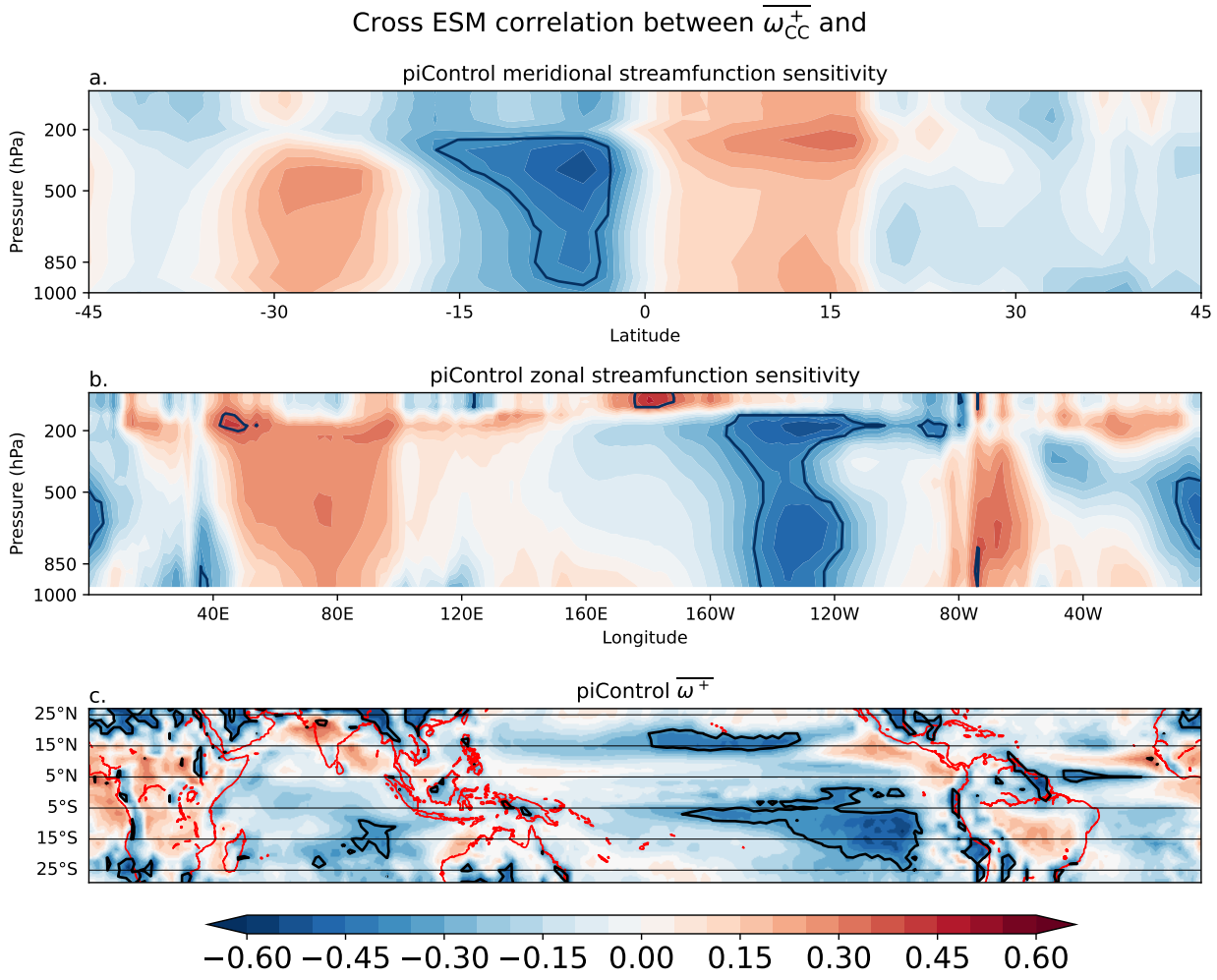

Figure 3.A.3: Model cross correlation between $\overline{\omega_{CC}{}^{+}}$ and piControl (a) meridional stream function sensitivity, (b) zonal stream function sensitivity, and (c) annual mean ω^{+}. The black contour in all panels indicates the p value=0.01.

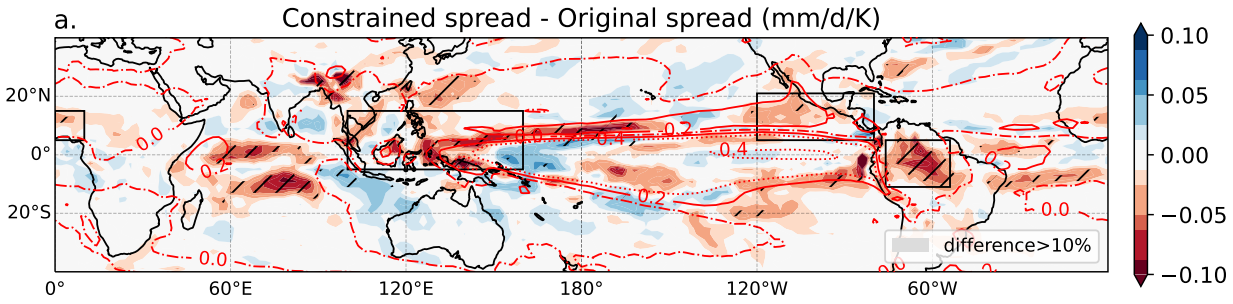

Figure 3.A.4: Same as Figure 3.4a but for the difference between the constrained spread and the original model spread, calculated as the difference between 5th and 95th percentiles. Hatching indicates the regions where the difference is larger than 10% and the original spread larger than 0.2 mm/d/K, to avoid division by small numbers.).

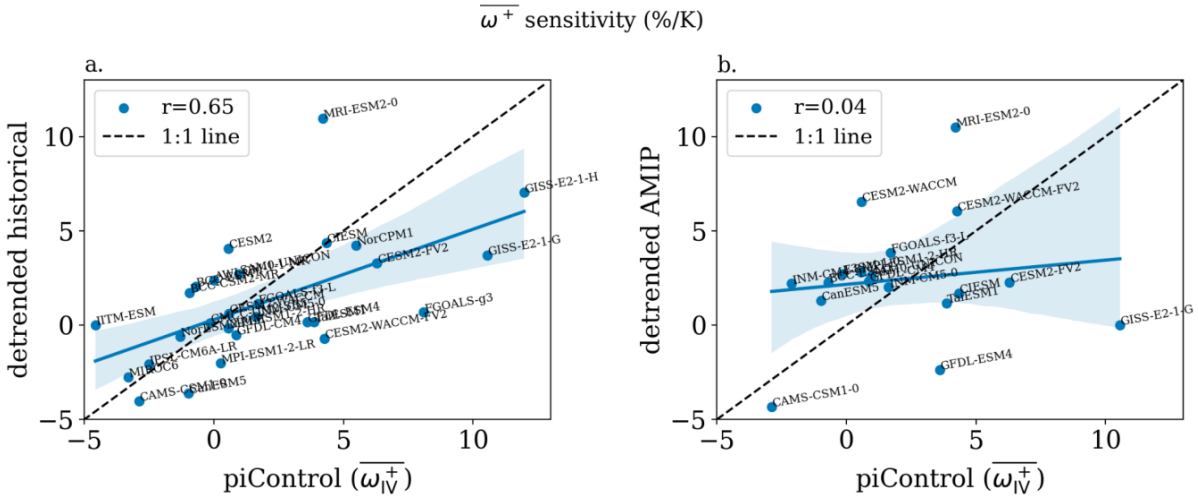

Figure 3.A.5: Relationship between the sensitivity of mean ω^+ to temperature under natural variability (%/K), calculated using piControl simulations ($\overline{\omega_{IV}{}^+}$) and (a) calculated using detrended historical simulations, (b) calculated using detrended AMIP simulation. Dashed black line represents the 1:1. Best fit line (blue) and the 95% confidence interval (shaded) are shown. r value shown is the Spearman rank correlation.

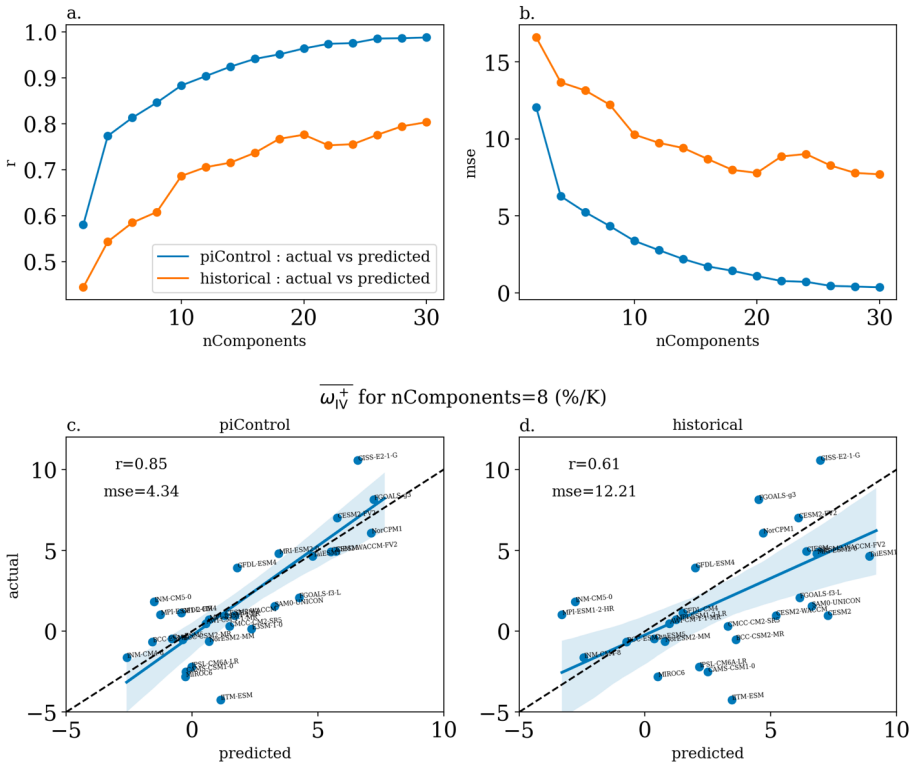

Figure 3.A.6: Metrics of the partial least square (PLS) regression model for estimating ω^+ using sea level pressure (slp) and surface temperature (tas). The correlation (r) (a) and the mean squared error (mse) (b) between actual and predicted sensitivity of ω^+ to temperature (i.e., x-axis of the emergent relationship, $\overline{\omega_{IV}{}^+}$). Predicted sensitivities ($\overline{\omega_{IV}{}^+}$) are calculated using the ω^+ estimates from the PLS regression model using slp and tas from piControl (blue line) and historical (orange line) simulations. r and mse values for different PSL components are shown. Eight PLS components are selected based on the r and mse of the historical simulations, as beyond this number the gain in accuracy is smaller. Predicted and actual $\overline{\omega_{IV}{}^+}$ for the selected PLS model (with 8 PLS components) for piControl (c) and historical (d) simulations. The dashed line represents the 1:1 line and the blue line is the best-fit linear regression line, with the 95% confidence interval shown in light blue. Following ref. *Po-Chedley et al.* (2022), the final value corresponding to observations is estimated after a bias correction using the fit between actual and predicted ω^+ of all piControl simulations.

CHAPTER 4

Climate change drives earlier wildfire season onset in California

[**Madakumbura, G. D.**, Moritz, M. A., McKinnon, K., Williams, A. P., Rahimi S. Bass, B., Norris J., Fu, R., Hall, A. (in review at *Nature Geoscience*). Climate change drives earlier wildfire season onset in California. preprint available at Research Square. `https://doi.org/10.21203/rs.3.rs-883244/v1`]

Abstract

Wildfires in California have become increasingly devastating in recent decades. The fire-season is also lengthening, with an earlier onset. This trend has been hypothesized to be driven by anthropogenic climate change, but it has yet to be quantitatively attributed to climate drivers. Using a comprehensive fire occurrence dataset, we analyze fire-season onset and climate controls on its variability and change during 1992-2020 in 13 California ecoregions. Northern California ecoregions with significant snow cover show a stronger trend towards later onset compared to more arid southern California ecoregions. Onset has trended earlier for all but one ecoregion. Interannual variability of onset is dominated by climate variability, mainly through soil moisture and atmospheric aridity. Even excluding fires from areas with rising human populations, climate factors still primarily dictate onset trends,

rather than human-caused ignitions. Trend attribution using the onset-climate relationship shows that, while natural variability has a large contribution to the earlier onset in Southern California, in 11 out of 13 ecoregions, climate change has advanced fire-season onset by 5-50 days during 1992-2020. Under continued warming, climate change is expected to continue to promote earlier fire-season onsets and exacerbate wildfire risks in California.

4.1 Introduction

Increasingly large and severe wildfires in the western United States (US) have become more costly in terms of lives lost and damage to property and infrastructure in recent decades, particularly in California (*Doerr and Santín*, 2016; *Zhuang et al.*, 2017; *Bowman et al.*, 2017; *Schoennagel et al.*, 2017). Wildfire damages in 2018 alone within California are estimated to be about $148.5 billion (*Wang et al.*, 2021). Anthropogenic climate change (ACC) has already changed fire weather by increasing surface temperature and evaporative demand (*Abatzoglou and Williams*, 2016; *Zhuang et al.*, 2021), and is likely to further exacerbate fire risk. This may happen both directly by altering seasonal patterns of temperature, precipitation, wind, and other conditions central for fire-weather and fuel aridity, and indirectly by increasing fuel availability (*Scott et al.*, 2013). In recent decades, a significant positive trend in annual burned area has been observed in California with strong links to the climate change-driven warming in the region (*Brown et al.*, 2023; *Westerling*, 2018; *Williams et al.*, 2019). A consideration of various characteristics of wildfires and a robust understanding of their controlling factors is vital for understanding how ACC influences fire conditions (*Bowman et al.*, 2020; *Krawchuk and Moritz*, 2014).

Fire-season onset timing is a fire behavior characteristic with practical applications in fire risk outlooks (*National Interagency Coordination Center*, 2021). An earlier than usual onset is an indicator of a potentially longer fire season, and therefore with the risk of more fires burning larger areas and with a longer mean burning time (*Westerling*, 2016). Onset has

been widely identified as when fire weather conditions first surpass a selected threshold (*e.g.*, *Jolly et al.* 2015). For instance, examining Canadian forests, (*Wotton and Flannigan*, 1993) defined onset as when maximum daily temperature first exceeds 12°C for three consecutive days. Such an emphasis on temperature in defining onset has naturally led to the conclusion that ACC has the potential to advance onset in many regions (*e.g.*, *Wotton and Flannigan* 1993; *Strydom and Savage* 2017), including California (*Abatzoglou and Kolden*, 2011). While fire weather is indicative of fire danger, fire occurrence also depends on fuel availability and ignition (*Moritz et al.*, 2012). Additionally, widely used fire weather metrics may not represent complex hydrological processes such as snow (*Abatzoglou and Williams*, 2016), which influences soil moisture and hence fuel flammability. This highlights the importance of investigating fire-season onset using fire occurrence data to develop a robust understanding of its drivers, including the influence of ACC (*Williamson et al.*, 2016).

The question of how much ACC and natural variability have contributed to the changes in historical fire-season onset in California has yet to be answered (*Westerling et al.*, 2006; *Westerling*, 2016). One major limitation of previous attempts to understand fire-onset (*Westerling et al.*, 2006; *Westerling*, 2016; *Dennison et al.*, 2014) is that they were restricted to large fire sizes (*e.g.*, fire size >405 ha). This reduced the sample size and made it more difficult to develop robust statistics, especially in regions where either fuel limitations or fire suppression efforts, or both, can limit the occurrence of such large fires. In addition, large fires may require the occurrence of multiple unique environmental stressors and conditions (*Khorshidi et al.*, 2020), making causal interpretations difficult. Moreover, offshore-wind-driven large fires in Southern California, in particular, are limited by human ignitions (*Keeley et al.*, 2021). Difficulty in interpreting the causal drivers makes attributing changes in fire onset to natural variability, ACC, and other potential causes challenging. This stresses the need for assessing the onset using comprehensive fire records with a wide spectrum of fire sizes and an objective definition of onset.

In this study, we use an extensive record of fire occurrence data from 1992-2020 for ecore-

gions in California (*Short*, 2022). By analyzing the distribution of start dates of all recorded fires, we define a physically interpretable fire-season onset. We utilize high-resolution observational climate data to identify mechanisms and main drivers of this onset. Through this mechanistic understanding, we quantify the influence of climate change and natural variability on observed changes in onset during recent decades.

4.2 Data and Methods

4.2.1 Fire occurrence and climate data

We use the 5th edition of the United States Forest Service Fire Program Analysis-Fire Occurrence Database (FPA-FOD) (*Short*, 2022). The dataset is quality-controlled and comprehensive, with 2.3 million wildfires that were recorded by United States federal, state, and local agencies during 1992-2020. We use the data attributes discovery date, and location (latitude and longitude) in the analysis.

To investigate the climate drivers of fire-season onset, observed monthly precipitation, snow water equivalent, maximum and minimum temperature, vapor pressure deficit, and soil moisture are obtained from TERRACLIMATE (*Abatzoglou et al.*, 2018), which has 1/24th degree spatial resolution for the period 1960-2020. For dynamical adjustment to isolate the natural variability, we use ERA5 (*Hersbach et al.*, 2020) sea level pressure (SLP) data for the period 1960-2020.

Considering the spatial heterogeneity of climatic conditions (*Minnich*, 2018; *Norris et al.*, 2021) and fire behavior (*van Wagtendonk*, 2018; *Williams et al.*, 2019) within California, we analyze 13 ecoregions based on United States Environmental Protection Agency's ecoregion level III classification (*Omernik and Griffith*, 2014). These ecoregions represent vegetation characteristics and climate conditions, from deserts to forests and therefore, results can implicitly indicate the role of vegetation in the onset-climate relationship (*e.g.*, *Syphard et al.* 2017).

4.2.2 Human population proxy

Nighttime light (*Elvidge et al.*, 1999) measurements are an indicator of human activities (*Li and Zhou*, 2017), which has also been found to be the best overall explanatory variable of the spatial variability of human-caused ignitions (*Chen and Jin*, 2022). We use the harmonized global nighttime light dataset from (*Li et al.*, 2020) regridded to a 270 m grid. To inspect the influence of human activities on onset-climate relationships, we remove fires from the regions with a positive trend in nighttime light for the period 1992-2018 (Figure 4.A.1).

4.2.3 Live and dead fuel moisture data

We use a deep learning-based reconstruction of dry season (July-August) liquid water in canopy above 2m in height, for 1992-2017 (*Asner et al.*, 2016; *Brodrick et al.*, 2019). This dataset is developed using remotely sensed canopy water estimates (high-fidelity imaging spectroscopy and light detection and ranging aerial surveys) and environmental data (*e.g.*, elevation, slope, aspect, relative elevation, Landsat 8 surface reflectance, distance to the nearest road, road density, maximum incident solar irradiation from four periods throughout the year, and spatial coordinates). The year 2012 is missing from this dataset due to missing Landsat training data. Original data at 30 m spatial resolution is regridded to a 270 m grid for the analysis.

As an independent measurement of fuel moisture, we use directly measure live fuel moisture content (LFMC) from the National Fuel Moisture Database. We first select sites across California that had at least one LFMC measurement during the August-September period and at least 25 years of summer data from the 1992-2020 study period. Recognizing the potential impact of data gaps, particularly during significant climatic events such as multi-year droughts or wet periods, we refine the selected dataset by excluding sites with any 3-year consecutive period of missing data, aiming to mitigate distortion in our correlation calculations. This provides at least one site for ecoregions: Central California Foothills and Coastal

Mountains, Southern California Mountains, Southern California Northern Baja Coast, and Sierra Nevada. We combine the regions with multiple sites to obtain one representative timeseries for each region.

4.2.4 Estimation of the influence of natural variability and climate change

To estimate the influence of natural variability and anthropogenic climate change (ACC), we first develop a causal effect network (CEN) following (*Kretschmer et al.*, 2016). We consider the following as key drivers of fire season onset: seasonal average precipitation, snow water equivalent, maximum and minimum temperatures, and VPD. This study posits that the effects of antecedent conditions, such as precipitation, snow, and temperature, persist into later seasons via soil moisture and therefore fuel moisture, thereby influencing the fire-onset. This is in addition to the immediate climatic conditions, such as VPD which can influence fire-onset through influencing dead/fine fuel moisture. For example, in regions where the fire season window (gray shaded area in Figure 4.A.1) ends in June-July-August (JJA), we analyze the aforementioned variables across seasons: December-January-February (DJF), January-February-March (JFM), February-March-April (FMA), March-April-May (MAM), April-May-June (AMJ), May-June-July (MJJ), and JJA of the current year, as well as DJF to November-December-January (NDJ) of the preceding year. This results in 19 seasonal timeseries for each variable, yielding a total of 95 potential predictor time series (19 seasonal timeseries for each of the 5 variables). The CEN framework provides a methodology based on causal discovery to identify the most important variables from this initial list.

As the first step, the correlation between the onset time series of each year and antecedent climate variables is calculated (*e.g.*, Figure 4.A.1) and the significant (p-value$<$0.1) cases are selected. This list of selected variables is called potential parents (P_0). As the second step, the P_0 are sorted based on the absolute value of the correlation above. Conditional independence tests are then carried out between each of the variables in P_0 and onset, first, by removing the influence of the variable with the highest correlation (say Z). This

is done by calculating the partial correlation. If a variable X has a statistically significant (p-value<0.05) partial correlation with onset, it is declared that X has an influence on onset independent of Z. If the partial correlation is not significant, the variable is removed. The causal principle that a variable must precede in time or occur simultaneously with another variable to influence it is always observed. This way we objectively obtain a smaller subset of P_0 (say P_1). This is repeated by conditioning on the variable with the next highest absolute correlation with onset in P_1. After evaluating conditional independence with one variable, we incrementally include two, three, and more variables, continuing until the resulting independent variables list converges. Finally, we create a least square regression model for the onset of each ecoregion using the selected climate drivers (Table 4.A.1, Figure 4.A.6). With the resultant drivers and the models of onset, we proceed to quantify their influence on onset.

To isolate the influence from natural climate variability, we use the dynamical adjustment technique (*Bass et al.*, 2022; *Siler et al.*, 2019; *Smoliak et al.*, 2015). Dynamical adjustment isolates the variability of the target climate variable that is linked to the circulation-induced variability. This is the dynamical component, which we treat as an estimate of natural climate variability. The residual contains the thermodynamic change that is forced by ACC-driven warming. Following *Siler et al.* (2019), we use SLP of the domain Northern Hemisphere 0-80°N Pacific/North America sector 110-290°E, as the variable that represents the circulation change and use partial least square (PLS) regression to map a target climate variable for a given season of all ecoregions (independent variable, y_0) onto the SLP (independent variable, X_0). We first remove the low frequency variability of X_0 ($X_{\text{low·freq}}$) and y_0 ($y_{\text{low·freq}}$) using nonparametric lowess smoothing. Then the $y = y_0$ - $y_{\text{low·freq}}$ is mapped onto the $X = X_0$ - $X_{\text{low·freq}}$ using PLS regression. The number of PLS components was selected using leave-one-out cross-validation. Natural variability component (dynamical component) is then estimated as the PLS modeled estimate (y_{mod}) and the ACC is taken as the residual, y_0 - y_{mod}.We follow this procedure for each variable and each season, separately. Once we

separate the natural variability and ACC component of each climate driver used to model onset, we estimate the contribution from each component on the onset trend.

It is important to note that the dynamical adjustment technique is just one among several methods available for this task (*Deser et al.*, 2020). The impact of methodological uncertainty on the quantitative estimates provided may warrant further studies.

4.2.5 Uncertainty estimation of the regression model

The uncertainty in regression coefficients is calculated by applying a leave-one-out procedure. For each sample, we remove one year at a time and re-create the climate-onset least square regression model, resulting in 29 different models.

For the uncertainty in the trend estimates and soil moisture contribution to onset (total, NV and ACC), we randomly resample the years with replacement and calculate the trend of observed onset, modeled onset, NV component and ACC component, for 100 samples. To estimate the uncertainty of the attribution of observed trends in onset to trends in modeled, NV and ACC, we calculate the contribution of trends for each of the above-created 29 leave-one-out regression models. This results in 2900 estimates for each variable.

All trend estimates in this study are calculated using linear least-square regression.

4.3 Results

4.3.1 Onset based on fire occurrence records

Figure 4.1 shows the time series of onset for 13 level III ecoregions of California (*Omernik and Griffith*, 2014). Following *Hanes et al.* (2019), fire onset is defined as the 5th percentile of the empirical cumulative distribution function of the discovery dates of fires during each calendar year (i.e. the Julian date). The distributions of onset during 1992-2020 in each ecoregion show different shapes (Figure 4.1, subpanel insets). Northeastern California (Cascades, and

Eastern Cascades Slopes and Foothills) shows a peak of onset in May-July. By contrast, Northwestern and Central California (Coast Range, Klamath Mountains/California High North Coast, Central California Foothills and Coastal Mountains, Central California Valley, and Sierra Nevada) have a peak in April-June; in southern California, the fire-season often begins in the latter part of the cool season (January-March). These contrasts are indicative of the background climates among ecoregions. In addition to a later end to wet season precipitation, Northeastern ecoregions have a large snow and subsurface water storage that can carry the moisture from the winter precipitation towards the spring and summer, delaying fire onset (*Bales et al.*, 2006). Meanwhile, Southern California is more arid with an earlier end to the wet season, so that soil moisture from winter precipitation is less persistent through the dry season (*van Wagtendonk*, 2018). Furthermore, southern California can experience periods of very high vapor pressure deficit (VPD), even in winter when offshore Santa Ana winds can be strong (*Jin et al.*, 2015; *Faivre et al.*, 2014). Southern California also has extremely high variability in the timing and magnitude of the winter rainy season and precipitation events within it (*Byrne et al.*, 2023), likely contributing to the multimodal distribution of fire-onset in some ecoregions.

All ecoregions except the Sonora Basin and Range show a negative trend in the onset (i.e., Julian date of onset becoming earlier in the year). Arid and semi-arid ecoregions (Mojave Basin and Range, Southern California Northern Baja Coast, Southern California Mountains, Northern Basin and Range, Sonoran Basin and Range, Central Basin and Range) show insignificant to marginally significant trends at the 0.1 level ($0.06<$p-value<0.33). But the rest of the ecoregions show rapid and significant trends (p-value<0.01). The most negative trends are in the Cascades (-2.7 days/year), Eastern Cascades Slopes and Foothills (-2.4 days/year), Central California Foothills and Coastal Mountains (-2.2 days/year) and Central California Valley (-2.1 days/year).

4.3.2 Climate controls of fire-season onset

Based on the contrasting distributions of the onset across ecoregions observed in Figure 4.1, we hypothesize that onset variability is dominated by climate. To investigate this, the correlation between the linearly detrended onset and detrended climate variability of different seasons is shown in Figure 4.5 and Figure 4.A.1. The antecedent climate variables suggest causal links with the onset. Winter and early spring (December-March) soil moisture is generally the variable with the highest correlation, and is significant for all ecoregions. This correlation is greatest for the Central California Foothills and Coastal Mountains (0.89), Southern California Mountains (0.88), Sierra Nevada (0.87), and Southern California Northern Baja Coast (0.87). Winter precipitation generally has the next highest correlation, although this likely reflects mostly the same information as soil moisture. Spring to summer VPD (Figure 4.A.1) shows strong negative correlations, especially for the Southern California Mountains (-0.78), Klamath Mountains/California High North Coast (-0.75), and Sierra Nevada (-0.71). And this is similarly reflected by strong negative correlations for temperature in the same months. Meanwhile, high mountainous regions (Sierra Nevada, Southern California Mountains, and Cascades) show large positive correlations for snow water equivalent (0.77, 0.69, and 0.67, respectively). Overall, these relationships indicate that winter precipitation and snow can influence the onset through delayed effects on soil moisture and VPD, while spring to summer temperature and VPD can influence onset over shorter timescales.

Trends in human ignitions have been found to influence fire characteristics (*Balch et al.*, 2017). Repeating the analysis excluding areas with increasing human population (Methods, Figure 4.A.2-4.A.4), we find similar onset trends and onset-climate relationships to those shown in Figure 4.5. Furthermore, the number of human-ignited fires is showing decreasing trends in many ecoregions, throughout the year (Figure 4.A.5). These results suggest the trends in fire onset observed here are mainly controlled by climate, not human activities. While the interannual variability of other fire characteristics such as burned area can be significantly influenced by fuel amount and human population density (*Forkel et al.*, 2019),

our results suggest interannual variability of fire-season onset is mostly governed by climate impacts, possibly through influencing the moisture content in the plant material itself.

To further investigate how climate can influence the fire-onset, we examine the relationship between fire-onset and fuel moisture. Climate conditions can impact the onset by affecting the moisture content of both live and fine dead fuels. However, as the analysis here is conducted on monthly to seasonal climate timescales, fine dead fuel moisture estimates relevant for igniting and carrying fire under many synoptic weather conditions (*e.g.*, 1 and 10-hour dead fuel moisture content; *Nelson* 2000) fall outside this study's scope. Therefore, we limit our analysis to live fuel moisture. Remote-sensing-based estimates of vegetation moisture content can provide more spatially and temporally complete data compared to direct measurements of live fuel moisture content (LFMC) (*Dennison et al.*, 2005; *Roberts et al.*, 2006; *Rao et al.*, 2023). Remote sensing-based reconstructions of dry-season canopy water content (CWC) of vegetation canopy above 2m in height (*Asner et al.*, 2016; *Brodrick et al.*, 2019) show significant positive correlation with fire-onset across California (Figure 4.3a). This strong relationship is particularly evident in Southern California ecoregions, Central California Foothills and Coastal Mountains, Cascades, and the southern Sierra Nevada. We also investigate this relationship using direct measurements of LFMC from the National Fuel Moisture Database for regions that have continuous coverage (see Methods). This verifies the reconstructed CWC results (Figure 4.3b-e), in particular for the Central California Foothills and Coastal Mountains (r=0.69), Southern California Mountains (0.72), Southern California Northern Baja Coast (0.66), and Sierra Nevada (0.66). Regions with particularly high fuel moisture and onset correlation in Figure 4.3 also stand out as the regions where the soil moisture-onset correlation in Figure 4.5 are strong. This is consistent with the soil moisture dominance in the temporal and spatial variability of fuel moisture (*Brodrick et al.*, 2019; *Countryman and Dean*, 1979; *Goulden and Bales*, 2019).

4.3.3 Roles of natural variability and climate change on observed onset trends

With the above mechanistic understanding of how onset variability is controlled by climate variability, we next decompose the influences of climate drivers on the observed onset trend. Using a causal effect network framework (*Kretschmer et al.*, 2016; *Runge et al.*, 2015, 2019) we select the climate variables and seasons that have a causal influence on onset for each region (see Methods). We then model the fire-onset of each ecoregion as a linear function of these climate variables. Next, the time series of each climate variable is separated into natural-variability and ACC-driven components, using the dynamical adjustment technique (see Methods). Dynamical adjustment isolates the variability of the target climate variable that is linked to the circulation-induced variability (*Bass et al.*, 2022; *Siler et al.*, 2019; *Smoliak et al.*, 2015). This is the dynamical component, which is generally interpreted as due to natural variability. The residual contains the thermodynamic change that is generally interpreted as due to ACC-driven warming. From these time series of natural variability and ACC components of climate drivers, contribution to onset trend by each component is estimated (Figure 4.4, Figure 4.A.6).

California experienced a severe multiyear drought during 2012-2015 (*Madakumbura et al.*, 2020; *Williams et al.*, 2015). Dominated by this drought, the natural variability components of all regions have a large negative trend. This negative trend caused earlier fire-onset in all ecoregions. The largest contribution from natural variability can be seen in the arid/semi-arid regions of the Mojave Basin and Range (accounting for a trend of 30 days from 1992–2020) and Southern California Mountains (25 days). The smallest influence of natural variability is seen in the Sonoran Basin and Range (a negative trend contribution of 3 days).

Distributions of ACC contribution are either partially or completely negative, contributing to an earlier onset. Central estimates of distributions show that ACC has contributed to an earlier onset in nine out of thirteen ecoregions. This is particularly pronounced in the Cascades (50 days), Northern Basin and Range (38 days), and Sierra Nevada (31 days).

Meanwhile, in southern California ACC has slightly delayed onset, ranging from 9 days in the Mojave Basin and Range to 13 days in the Sonoran Basin and Range. One possible reason for this is that some of these regions are more fuel-limited, where moisture is needed for fuel growth, making the climate-onset relationship more complicated than the modeling approach considered in this study. Furthermore, this could also be due to the greater influence of precipitation variability over warming in these water-limited regions (Figure 4.5, Figure 4.A.1). Specifically, the definition of onset used in this study—the 5th percentile of the empirical cumulative distribution function of the discovery dates of fires during each calendar year—marks the fire onset in Southern California during the latter part of the cool and wet season (Figure 4.1). This is a period during which precipitation variability outweighs the effect of temperature variability (Table 4.A.1). For higher percentiles of the empirical cumulative distribution function, we observe a clear and larger contribution from ACC towards an earlier fire activity in Southern California (Figure 4.A.7-4.A.8).

Climate does not fully account for the observed trends of fire-onset in some ecoregions (difference between observed and modeled trend distributions in Figure 4.4), particularly the Coast Range, Eastern Cascades Slopes and Foothills, and Central California Foothills and Coastal Mountains. Possible reasons could be nonlinear climate influences not captured by our linear models, or other factors that we did not consider.

4.4 Discussion

Understanding how ACC influences fire-season onset in California is critical for disaster risk reduction efforts. Previous analyses to understand onset have generally focused on the onset of fire weather but not fire occurrence. Fire-weather indices are indicative of the atmospheric evaporative demand and near-surface soil moisture, and therefore serve as proxies for fuel moisture. But they do not capture complex ecohydrological processes and feedbacks, and do not fully represent mechanisms relevant to fire-season onset (*e.g.*, *Holden et al.* 2018). Our

results based on fire occurrence data present an estimate of onset that is physically consistent with variations in surface and subsurface water budgets and fuel moisture in distinct climate regimes of California.

Our results highlight a geographical divide across California in the contributions of climate change versus internal variability to onset trends. A large, onset-promoting influence of ACC in Northern California stems from the strong influence of temperature on snow melt (*Bales et al.*, 2006; *Westerling et al.*, 2006) and evapotranspiration (*Goulden and Bales*, 2014, 2019). Climate-change-driven warming in California has already emerged from the interannual temperature variability (*USGCRP*, 2023). This indicates a continuing shift in the distribution of the onset in Northern California beyond the envelope of natural variability.

There is a large natural variability in precipitation in California (*Dettinger et al.*, 2011), and there is large uncertainty regarding the sign of the anthropogenic precipitation change (*Langenbrunner and Neelin*, 2017). This makes the detection and separation of the climate change component of precipitation very difficult (*McKinnon and Deser*, 2021) and implies a large uncertainty in the estimates of the ACC contribution. More subtle changes in precipitation characteristics, such as a shortening of the wet season (*Swain*, 2021) and a decrease in precipitation frequency (*Gershunov et al.*, 2019; *Holden et al.*, 2018) could also influence statistics of aggregate fire behavior, such as onset. ACC also alters the precipitation partitioning in California, shifting from snow-dominant to rain-dominant (*Gergel et al.*, 2017), thus modifying the snow-climate relationships identified in this study. In future work, climate-based modeling of onset presented in this study could be modified to incorporate these nonlinear changes in precipitation characteristics.

The climate control of fire-onset is ubiquitous across California, in ecoregions with varying vegetation characteristics, from deserts to forests. However, assessments of fire-onset date aggregated across an ecoregion may give more weight to the more fuel-abundant areas within the ecoregion. Future analysis should more rigorously evaluate the role of land-cover type in modulating the effect of fuel moisture on fire-season onset. Other fuel characteristics

can also have interannual variability (*e.g.*, *Koontz et al.* 2020). For example, wet years can promote fuel growth in fuel-limited regions (*Williams et al.*, 2019; *Keeley and Syphard*, 2019); meanwhile, drought leads to tree mortality, which may further increase fire risk beyond that expected from fuel drying alone (*Millar and Stephenson*, 2015).

Climate variability shapes fuel availability, ignition efficiency, and fuel combustibility, irrespective of the ignition sources (*Abatzoglou and Williams*, 2016; *Scott et al.*, 2013; *Rao et al.*, 2023). However, most fire ignitions in California are caused by human activities, which have major impacts on the number and seasonality of wildfires in the state, particularly by widening the fire-season beyond the summer months when lightning is most common (*Keeley and Syphard*, 2018; *Balch et al.*, 2017). We attempted to remove the possible influence from trends in human ignitions by removing fires from regions that have a positive trend in nighttime light, a well-known proxy for human population density. However, it is important to acknowledge the caveat that human influence on fire ignition extends beyond areas illuminated at night. Fires can be ignited by human activities or equipment in regions far from urban areas, indicating that the relationship between human presence and fire ignitions is more complex than what nighttime light data alone can reveal. This complexity might be one of the reasons why climate alone cannot fully explain the observed trend in fire-onset in multiple ecoregions.

Our analysis provides a framework for understanding the mechanisms through which climate conditions control fire onset. The ACC component in predicting onset is indicative of what is to come, as ACC-driven warming trends continue. Thus, our findings have major implications for wildfire disaster prevention and management strategies in coming seasons and years.

Acknowledgements. This research was funded by the University of California Laboratory Fees Research Program (LRF-18-542511) and Department of Energy's HyperFACETS (DE-SC0016605) project. GDM, JN and AH acknowledge the support from the Regional and Global Model Analysis Program for the Office of Science of the U.S. Department of Energy through the Program for Climate Model Diagnosis and Intercomparison. GDM acknowledge the valuable discussions on dynamical adjustment with Stephen Po-Chedley.

4.5 Figures

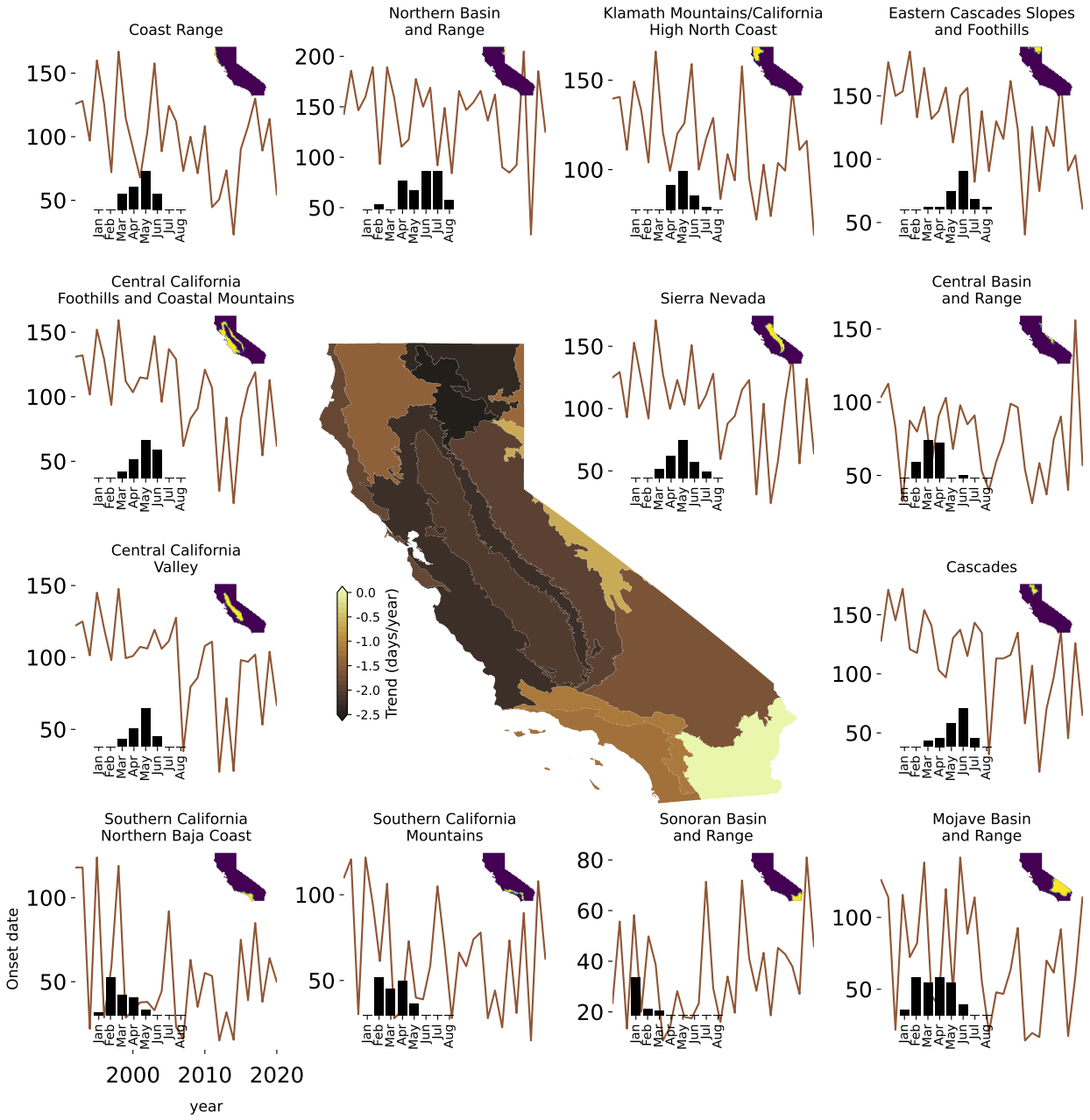

Figure 4.1: Trends in fire-season onset during 1992-2020. Fire-season onset timeseries defined as the 5th percentile of the cumulative distribution of the occurrence day (Julian date, shown on y-axis) of all fires of each year, for each ecoregion. The subpanel inset histogram shows the distribution of the detrended onset date in months January (Jan) to August (Aug).

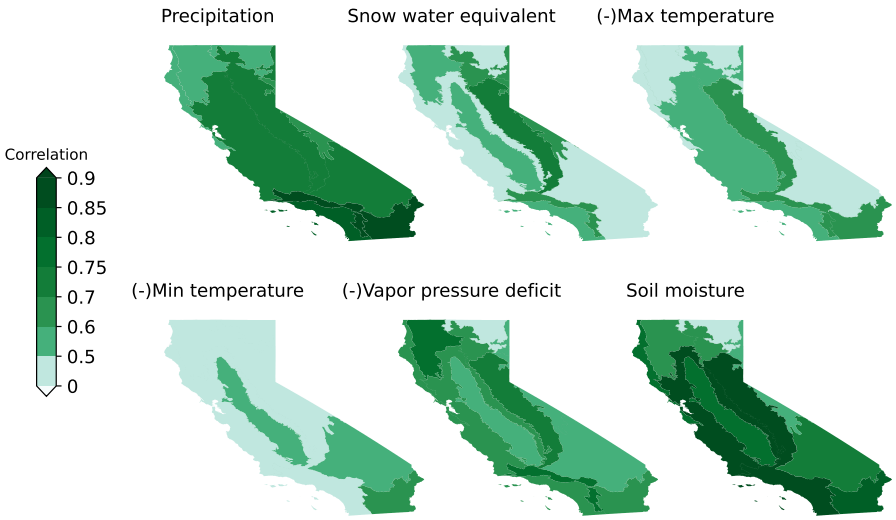

Figure 4.2: Relationship between climate variable and fire-onset. Correlation between detrended fire-onset and detrended precipitation, snow water equivalent, maximum temperature, minimum temperature, vapor pressure deficit, and soil moisture. For maximum and minimum temperature and vapor pressure deficit, the correlation is multiplied by -1 in the figure. Correlation is calculated against the given variable, averaged over each antecedent 3-month running period (DJF, JFM, etc.) to onset and the strongest correlation for each variable, among all seasons, is shown here.

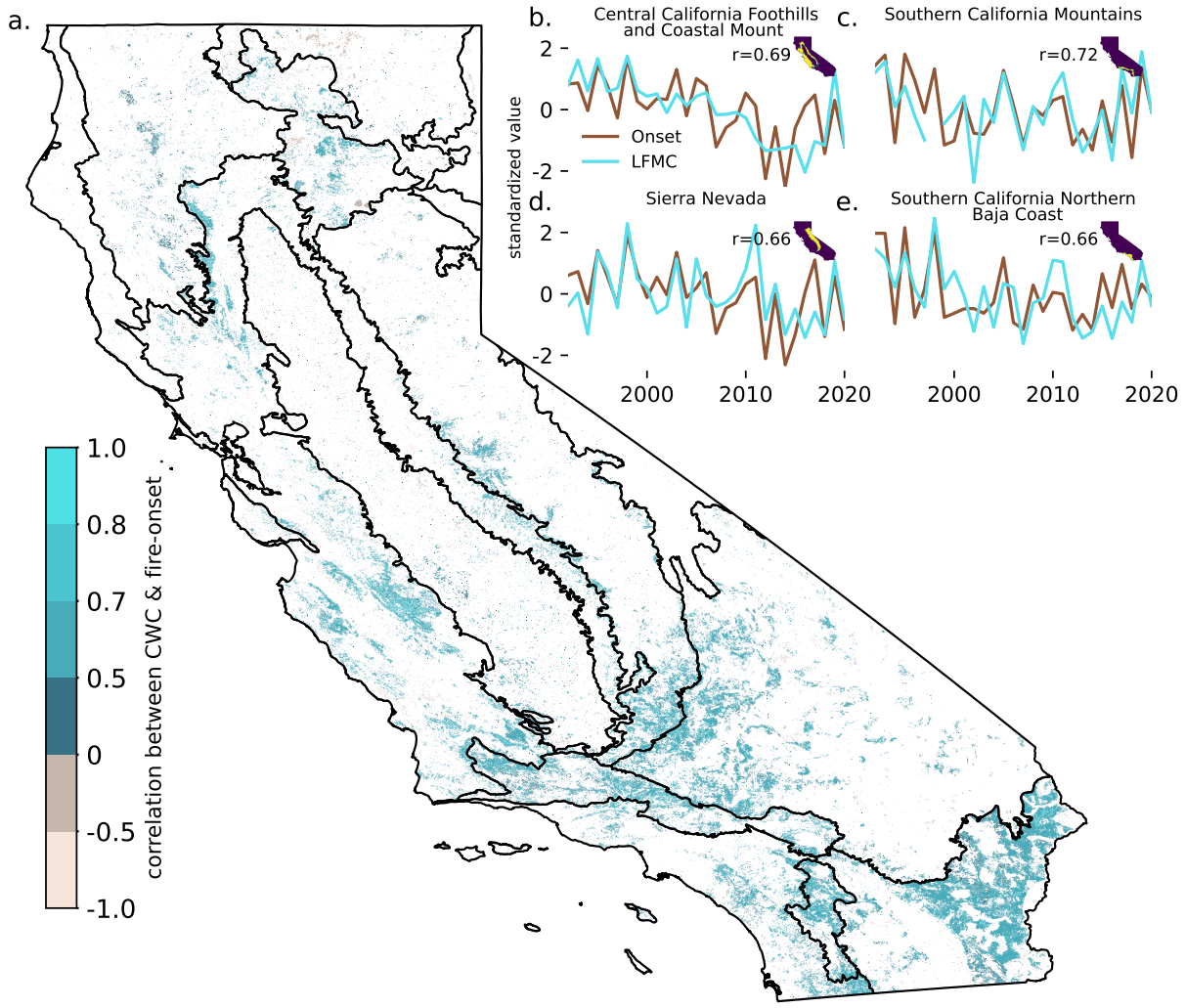

Figure 4.3: Relationship between fire-season onset and measures of vegetation moisture. (a.) Correlation between fire-season onset and reconstructed canopy water content (CWC) using remote sensing and environmental data (*Asner et al.*, 2016; *Brodrick et al.*, 2019) for the period 1992-2017. Each grid cell value represents the correlation between that grid cell's canopy water record and the fire-onset record for the ecoregion that the grid cell lies within. (b-e) Timeseries of the fire-season onset and representative live fuel moisture content (LFMC) measurements during 1992-2020 for Central California Foothills and Coastal Mountains (b), Southern California Mountains (c), Sierra Nevada (d), and Southern California Northern Baja Coast (e). Correlation between onset and LFMC (r) is shown in panels b-e. Only statistically significant values after controlling for a false discovery rate (Benjamini Hochberg 1995) of 20% (with a corresponding p value of 0.04) are shown.

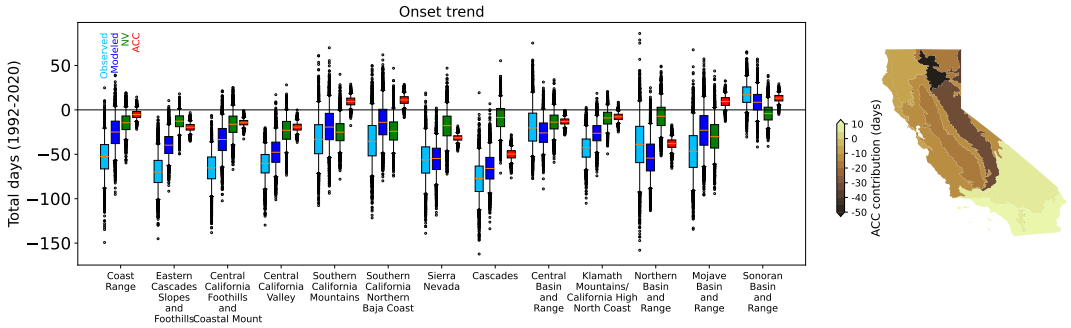

Figure 4.4: Influence of natural variability and climate change on observed trend in onset. Trends of observed onset from 1992-2020 (Observed, light blue), and onset modeled using total climate variability and trend (Modeled, dark blue), natural variability (NV, green) and anthropogenic climate change component of climate variables (ACC, red). Modeled trend distributions are created by considering the uncertainty of regression model and trend estimation, yielding 2900 values per region (Methods). Boxplots indicate the median (orange horizontal line) and the interquartile range. Whiskers show the percentiles 2.5 and 97.5. Outliers are shown by circles. Right panel shows the mean ACC contribution for each region.

Appendix

4.A Supplement

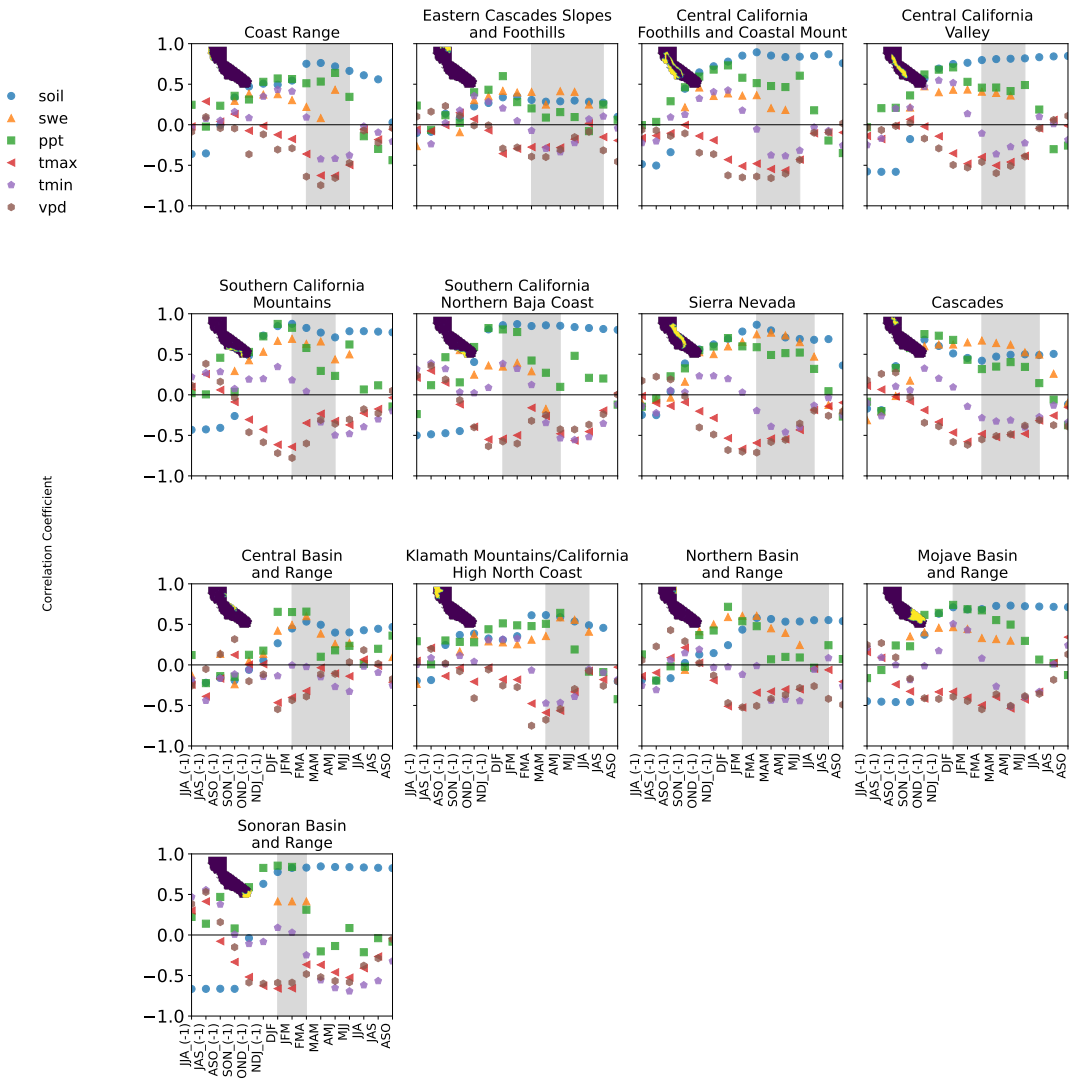

Figure 4.A.1: Relationship between climate variable and onset. Correlation between detrended onset and precipitation (ppt), snow water equivalent (swe), maximum temperature (tmax), minimum temperature (tmin), vapor pressure deficit (vpd), and soil moisture (soil) in the given seasons. The gray shaded area shows the seasons when the onset has occurred in the past in the region.

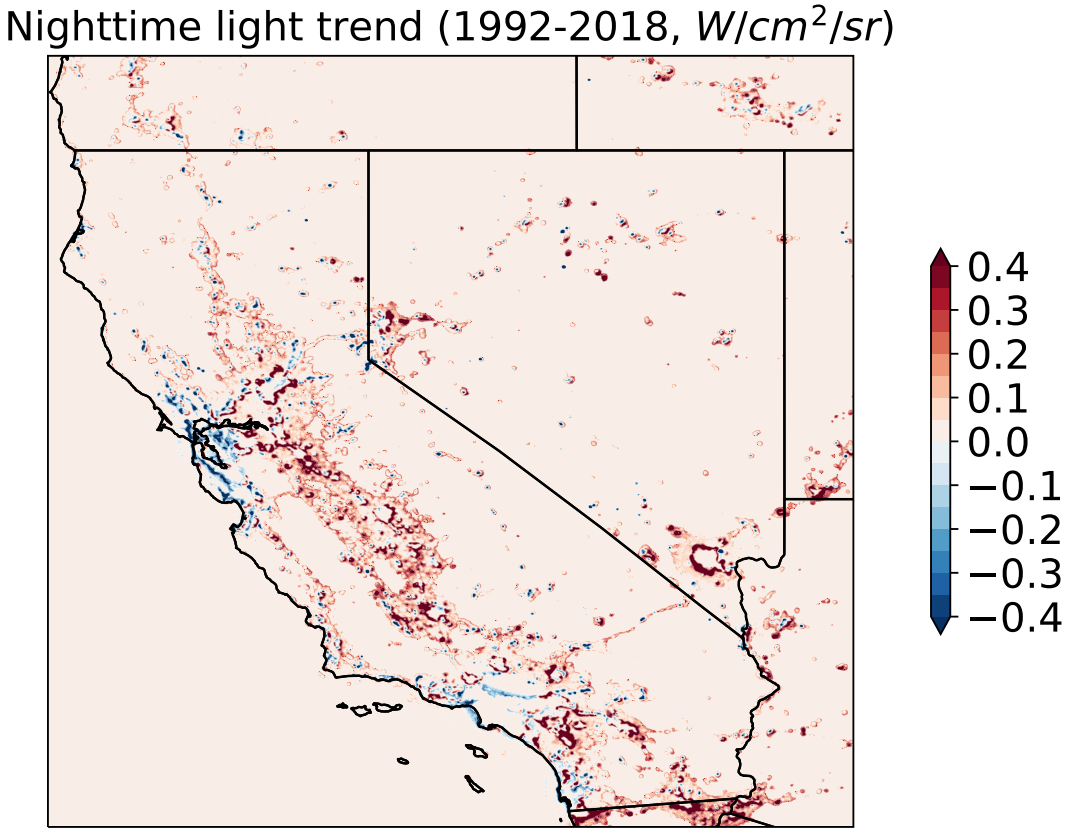

Figure 4.A.2: Nighttime light trend for 1992-2018.

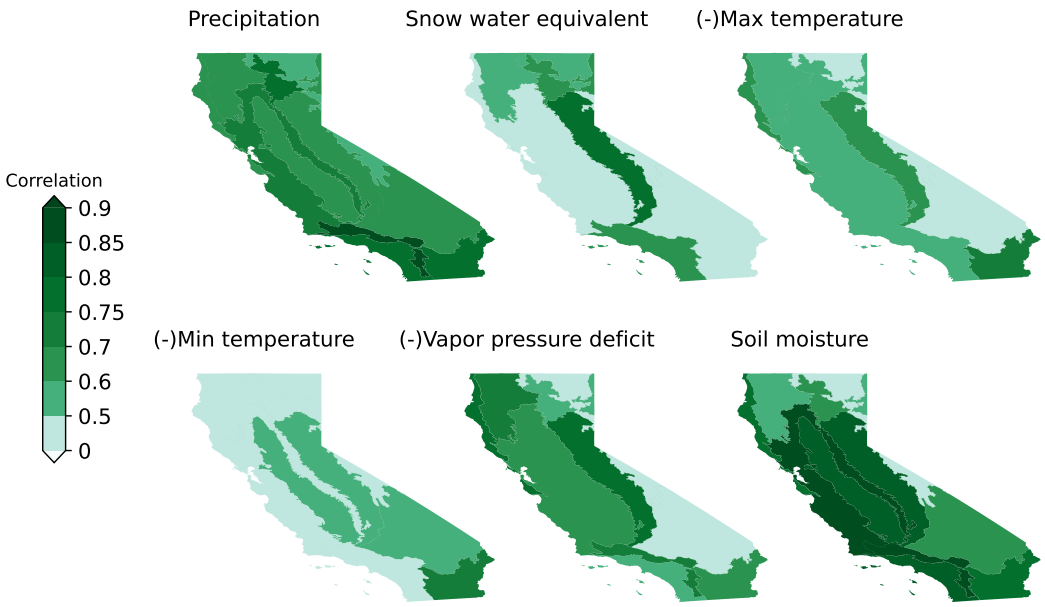

Figure 4.A.3: Same as Figure 2 but after removing fires from regions with a positive trend in nighttime light during 1992-2018.

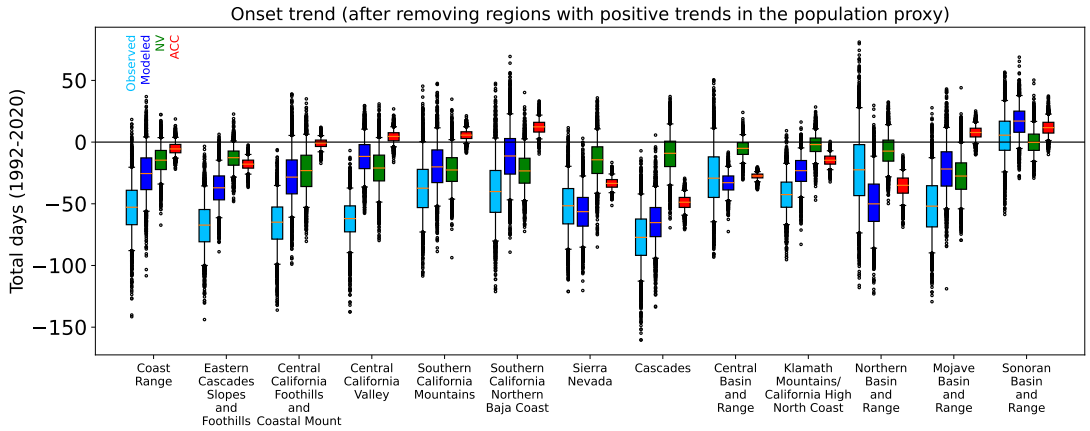

Figure 4.A.4: Same as Figure 4.4 but after removing fires from regions with a positive trend in nighttime light during 1992-2018.

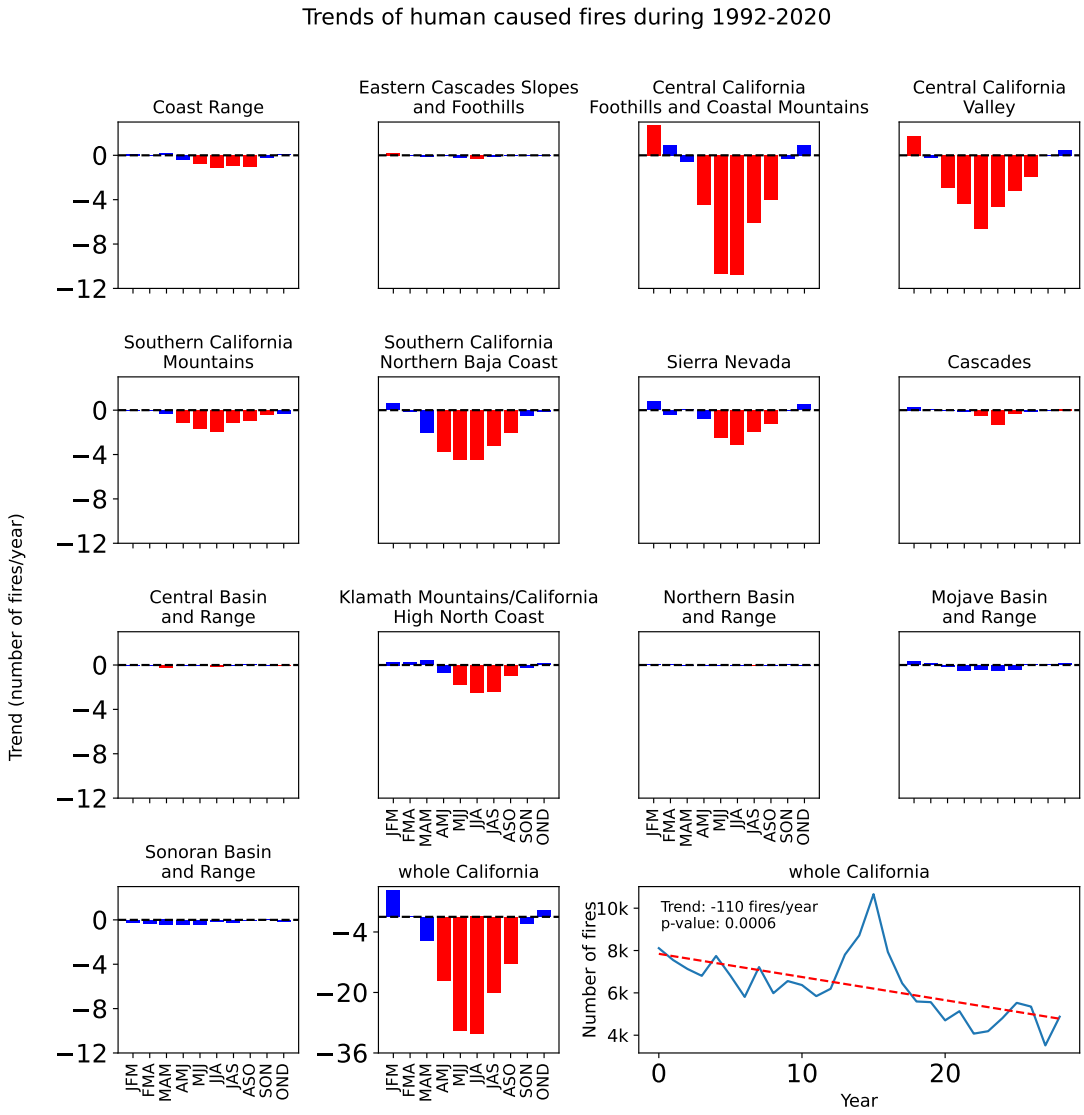

Figure 4.A.5: Trends in the number of human-caused fires during 1992-2020. Trends that are at least marginally significant (p-value<0.1) are shown in red. Note that the y-axis range is different for the bottom-middle panel, which represent data for whole California.Bottom right panel shows the timeseries of annual fire frequency (blue solid line) and the linear trend (red dashed line). Magnitude and the statistical significance of the trend is annotated.

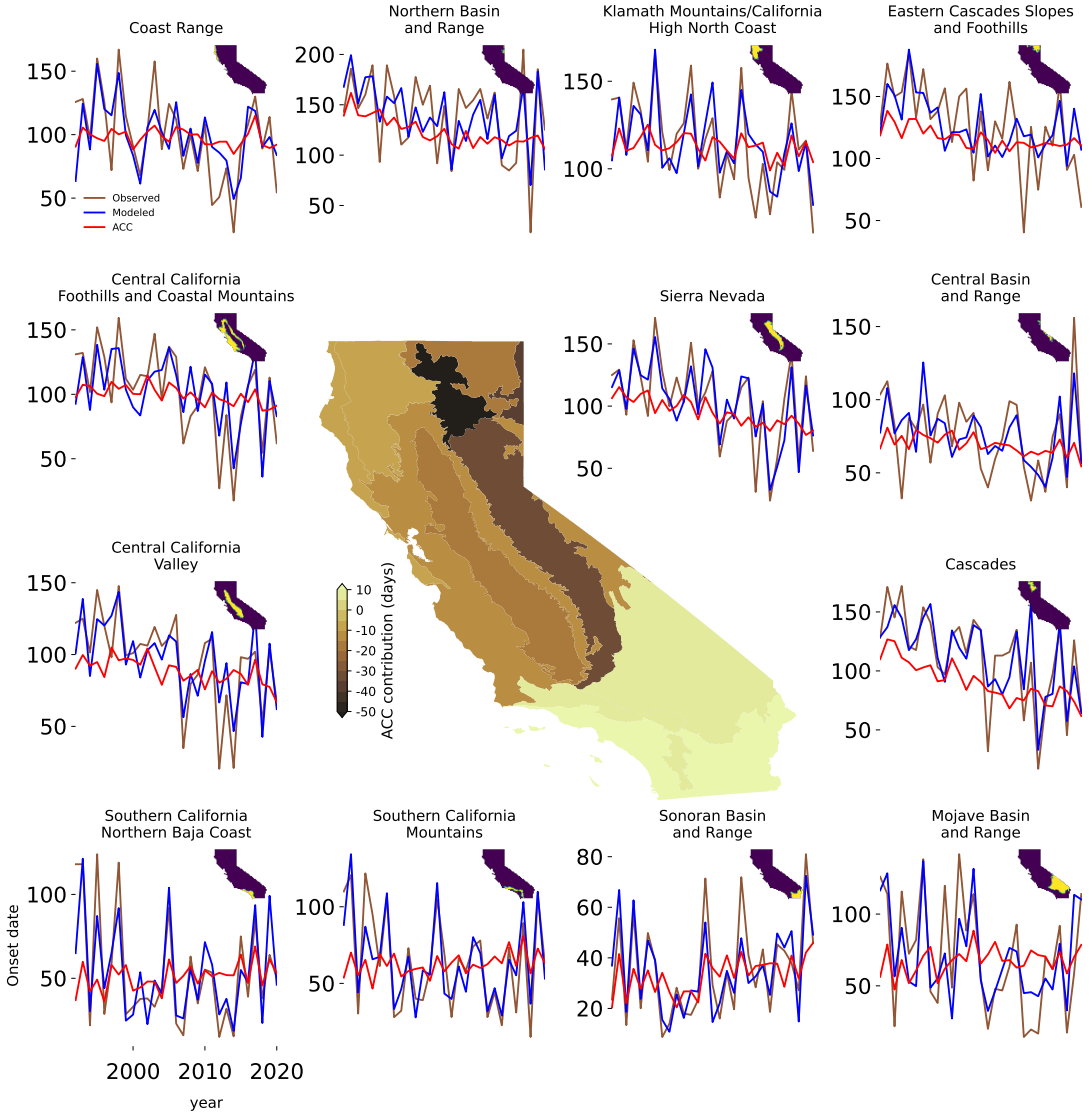

Figure 4.A.6: Observed and modeled onset timeseries and the climate change contribution to the onset trend during 1992-2020. Timeseries of observed onset (Observed, brown), onset modeled using climate (Modeled, blue) and the climate change component of the modeled onset (ACC, red) for each ecoregion. Middle panel shows the total contribution (days) from ACC to the observed onset trend during 1992-2020.

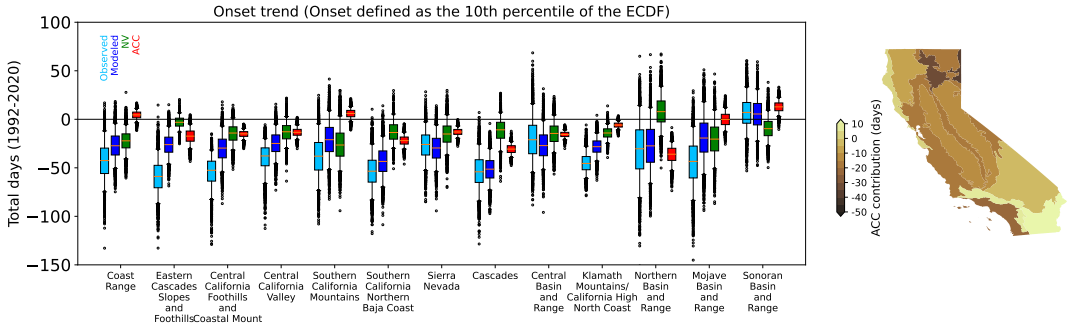

Figure 4.A.7: Same as Figure 4.4 but for fire-onset defined as the 10th percentile of the empirical cumulative distribution function of the discovery dates of fires during each calendar year.

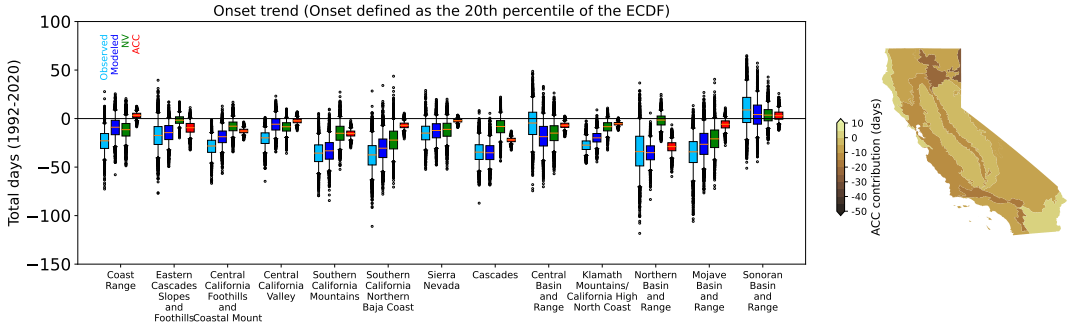

Figure 4.A.8: Same as Figure 4.4 but for fire-onset defined as the 20th percentile of the empirical cumulative distribution function of the discovery dates of fires during each calendar year.

Table 4.A.1: Causal effect network-based modeling of fire-onset using climate drivers. Precipitation (ppt), snow water equivalent (swe) maximum temperature (tmax), minimum temperature (tmin), and vapor pressure deficit (vpd) are used as climate drivers. In the equations, lag1 indicates the previous year.

	Region	R2	Model Equation
1	Coast Range	0.527	Onset = 98.79 + 29.65*ppt__lag1_NDJ - 11.12*vpd__AMJ - 16.85*ppt__lag1_OND
2	Eastern Cascades Slopes and Foothills	0.398	Onset = 126.85 + 16.61*ppt__DJF + 4.58*ppt__lag1_JJA - 10.22*tmin__lag1_JJA
3	Central California Foothills and Coastal Mount	0.584	Onset = 102.85 + 18.26*ppt__lag1_NDJ - 14.87*vpd__DJF - 2.92*ppt__lag1_SON
4	Central California Valley	0.679	Onset = 96.26 + 16.97*ppt__DJF + 3.84*ppt__lag1_NDJ + 6.62*ppt__lag1_OND - 9.88*tmin__lag1_JJA
5	Southern California Mountains	0.777	Onset = 64.47 + 30.58*ppt__DJF - 4.20*ppt__lag1_NDJ + 0.64*ppt__lag1_OND + 7.10*tmax__lag1_DJF - 3.72*vpd__lag1_DJF
6	Southern California Northern Baja Coast	0.712	Onset = 53.59 + 20.28*ppt__DJF + 6.91*ppt__lag1_NDJ + 4.51*tmax__lag1_DJF
7	Sierra Nevada	0.758	Onset = 104.11 - 11.89*vpd__FMA - 14.22*vpd__DJF + 14.97*ppt__lag1_NDJ + 6.83*tmax__lag1_NDJ - 7.59*tmin__lag1_JJA
8	Cascades	0.706	Onset = 111.77 - 15.65*vpd__DJF + 19.78*ppt__lag1_OND - 19.21*tmin__lag1_JJA
9	Central Basin and Range	0.529	Onset = 76.11 + 11.59*ppt__FMA + 5.62*ppt__DJF - 6.15*tmax__DJF - 5.31*tmin__lag1_JAS
10	Klamath Mountains/California High North Coast	0.617	Onset = 115.21 - 9.17*ppt__AMJ - 6.50*vpd__FMA + 5.94*ppt__lag1_NDJ + 6.86*ppt__lag1_JJA - 5.98*ppt__lag1_FMA
11	Northern Basin and Range	0.565	Onset = 139.72 + 16.87*ppt__DJF - 10.07*vpd__DJF - 14.18*ppt__lag1_DJF - 16.40*tmin__lag1_JJA
12	Mojave Basin and Range	0.639	Onset = 70.95 + 21.01*ppt__FMA + 8.74*ppt__DJF + 8.83*ppt__lag1_OND
13	Sonoran Basin and Range	0.766	Onset = 35.27 + 10.28*ppt__lag1_NDJ + 3.65*ppt__lag1_OND + 2.48*tmax__lag1_JAS + 7.78*vpd__lag1_DJF - 0.70*tmax__lag1_DJF

CHAPTER 5

Recent California tree mortality portends future increase in drought-driven forest die-off

[**Madakumbura, G. D.**, Goulden, M.L., Hall, A., Fu, R., Moritz, M.A., Koven, C.D., Kueppers, L.M., Norlen, C.A. and Randerson, J.T., 2020. Recent California tree mortality portends future increase in drought-driven forest die-off. *Environmental Research Letters*, 15(12), p.124040. https://doi.org/10.1088/1748-9326/abc719]

Abstract

Vegetation tolerance to drought depends on an array of site-specific environmental and plant physiological factors. This tolerance is poorly understood for many forest types despite its importance for predicting and managing vegetation stress. We analyzed the relationships between precipitation variability and forest die off in California's Sierra Nevada and introduce a new measure of drought tolerance that emphasizes plant access to subsurface moisture buffers. We applied this metric to California's severe 2012-2015 drought, and show that it predicted the patterns of tree mortality. We then examined future climate scenarios, and found that the probability of droughts that lead to widespread die-off increases three-fold by the end of the 21st century. Our analysis shows that tree mortality in the Sierra Nevada will likely accelerate in the coming decades and that forests in the Central and Northern Sierra

Nevada that largely escaped mortality in 2012-2015 are vulnerable to die-off .

5.1 Introduction

Droughts are among the worst climate hazards society faces, creating economic losses of tens to hundreds of billion US dollars per year (*Mishra and Singh*, 2010; *Commission*, 2012). Forests are especially vulnerable to drought in a warming world, as higher temperatures increase atmospheric moisture demand, evapotranspiration and soil drying and tree die-off (*Allen et al.*, 2010; *Williams et al.*, 2013; *Allen et al.*, 2015; *Fettig et al.*, 2019). Future droughts are projected to become longer, more severe and frequent in many regions (*Wehner et al.*, 2011; *Seneviratne et al.*, 2012; *Madakumbura et al.*, 2019), with consequent impacts on vegetation structure and function. An improved understanding of forest response to drought is needed to better predict the impact of climate change on forested ecosystems at large scales. Such capabilities would help forest managers anticipate patterns of tree vulnerability to drought and proactively allocate resources and time at local and landscape scales (*Heinimann*, 2010; *Keenan*, 2015).

Studies investigating the causes of tree die off have advanced our knowledge of forest tolerance to drought, and the underlying interactions of biological, physiological and environmental factors. Robust statistical relationships between drought induced tree mortality and various metrics of drought intensity have often revealed ecological thresholds (*Anderegg et al.*, 2015; *Paz-Kagan et al.*, 2017; *Young et al.*, 2017; *Goulden and Bales*, 2019). These plant physiological and environmental predictors of mortality reflect the processes and properties that mediate the translation of precipitation deficit to physiological damage and ultimate tree death (*Anderegg et al.*, 2013).

The patterns of die-off ultimately depend on both drought intensity and duration, and processes that occur over a range of timescales (*McDowell et al.*, 2008). The biological response to drought stress has been investigated intensively at the scale of individual plants

based on theoretical (*McDowell et al.*, 2008) and experimental (*Barbeta and Peñuelas*, 2016) analyses, but studies that focus on multidecadal records and at landscape scales and larger are scarce. Given potentially large spatial variations in drought tolerance and drought severity across landscapes, such larger scale studies are needed. For example, while large variation in vegetation stress and tree mortality were noted across the Sierra Nevada landscape during California's 2012-2015 drought, but it is unclear whether the variation arises from forest drought tolerance (*e.g.*, water availability or plant physiological factors) or drought severity.

Comparisons of drought duration and remotely-sensed vegetation properties can provide an opportunity to investigate plant response and tolerance to drought at large spatial scales. The Normalized Difference Vegetation Index (NDVI) shows strong responses to droughts lasting 2-4 months in arid and humid biomes, and 8-10 months in semiarid and sub humid biomes in the world (*Vicente-Serrano et al.*, 2013). In a regional setting, a comparison between California forest water balance and canopy density, as measured by canopy water content (CWC) (*Asner et al.*, 2016), showed a comparatively long time scale response, with coniferous vegetation tolerating drought for several years before accelerated die-off (*Brodrick et al.*, 2019). Despite the insights from such comparisons, the controlling factors (*e.g.*, environmental and tree physiological properties) behind drought tolerance have not been fully explored. Efforts to forecast the long-term impact of drought are also complicated by the likelihood that climate, environmental conditions, and vegetation distributions may be different in the coming century (*Kelly and Goulden*, 2008; *Parks et al.*, 2018; *Holsinger et al.*, 2019).

Here we explore the timescale of drought response for coniferous forests in California's Sierra Nevada (*Myers et al.*, 2000; *Bales et al.*, 2011). This region experienced a severe drought in 2012-15 that was followed by widespread die-off in 2015-16. We used data from pre-2012 to identify the duration of drought that was best correlated with anomalies in canopy density time series as measured by the Normalized Difference Moisture Index (NDMI) (hereafter referred to as the drought sensitivity timescale or DST). We then investigate how

the pre-2012 DST interacted with drought severity to produce the observed spatial and temporal patterns of die off during the 2012-2015 drought. Finally, we use output from state-of-the-art global climate simulations to examine how changes in multi-year droughts may amplify future die-off episodes.

5.2 Data

5.2.1 Vegetation Indices

We used vegetation indices NDMI, NDVI, and CWC in this study. NDVI and NDMI were derived from Landsat 5, 7 and 8 surface reflectance and brightness temperature images. Data were obtained from USGS (https://espa.cr.usgs.gov) for the period 1984 to 2017 after being regridded to a resolution of 0.0002695^{o} (approximately 30 m). Snow- and cloud-affected pixels were removed using the Landsat collection 1 pixel-quality data layers. We used late growing season NDMI (Aug-Oct) in this study. Further details of the derivation of NDMI and NDVI can be found in ref. *Goulden and Bales* (2019). Dry season (July-Aug) CWC data at 30-m resolution (derived in ref. *Brodrick et al.* 2019) was obtained from `https://doi.pangaea.de/10.1594/PANGAEA.897276`.

As a direct measurement of tree mortality, we used the number of dead trees from the Aerial Detection Survey data from the USFS (`https://www.fs.usda.gov/detail/r5/forest-grasslandhealth/?cid=fsbdev3_046696`). We re-projected and rasterized the dead trees per acre (DTPA) '1' product in this geodatabase.

5.2.2 Historical climate data

To derive drought indices, we used high resolution monthly precipitation (PR) data (*Flint and Flint*, 2012), potential evapotranspiration (PET) and climatic water deficit (CWD) from the Basin Characterization Model (*Flint et al.*, 2013), a high resolution physically-based

hydrologic model developed for California (https://ca.water.usgs.gov/projects/reg_hydro/basin-characterization-model.html#provisional). Data from 1980-2016 were used at 270 m resolution. Annual mean NDVI was used to calculate the total evapotranspiration (ET) of water year from an exponential relation between ET and NDVI. This relation is derived from in situ measurements of ET, as in ref. *Goulden and Bales* (2019).

5.2.3 Future climate projections

To assess future drought conditions, we used monthly precipitation for the period 1850-2015 from historical simulations and from 2016-2100 for SSP2-4.5, SSP3-7.0 and SSP5-8.5 warming scenarios (*O'Neill et al.*, 2016) from ten of the state-of-the-art global climate models (GCMs) (Supplementary Table 1) participating in Coupled Model Intercomparison Project Phase 6 (CMIP6) (*Eyring et al.*, 2016). We selected available models with two or more ensemble members for all three scenarios at the time of analysis. In total, 90 ensemble members per scenario, were used. Use of a large ensemble dataset allows the sampling of extreme conditions without using statistical resampling methods (*Swain et al.*, 2018).

5.2.4 Predictors of DTPA

We carried out regression analysis to explain the spatial variations of dead trees per acre. Apart from climate and vegetation variables explained above, the following variables were extracted for the analyses: To represent resource competition (*Young et al.*, 2017), tree basal area data were obtained from the LEMMA group (https://lemma.forestry.oregonstate.edu/data). Soil plant available water content (AWC) was obtained from the US General Soil Map database (http://websoilsurvey.nrcs.usda.gov) by extracting the variable aws0150wta (units: cm). Subsurface drying can be directly linked to the amount of evapotranspiration exceeding the precipitation (*Goulden and Bales*, 2019). To represent the vegetation-induced subsurface moisture use, we use the mean evapotranspiration as a predictor variable.

5.2.5 Conifer fraction and fire

We limited the analysis to conifer dominated forests in the Sierra Nevada. To mask out non-conifer-dominated regions, we used the existing vegetation classification maps from the USFS (`https://www.fs.usda.gov/detail/r5/landmanagement/resourcemanagement`). From the vegetation classification maps, we selected pixels with vegetation types: Sierran mixed conifer, Ponderosa pine, montane hardwood-conifer, lodgepole pine, red fir, white fir, sub-alpine conifer, Jeffrey pine, Douglas fir, Eastside pine and pinyon-Juniper. We removed fire-impacted pixels from 1980 through 2016 from the analysis by using the fire history data product from California's Fire and Resource Assessment Program (`http://frap.fire.ca.gov/data/frapgisdata-sw-fireperimeters_download`).

5.2.6 Elevation data

Elevation data were obtained from USGS NED 1 arcsec digital elevation map (`https://viewer.nationalmap.gov/basic/`).

All vector data used in this study were first rasterized and all data were reprojected to World Geodetic System 1984 using ArcGIS 10.7 (`https://desktop.arcgis.com/en/`) and the GDAL library (`https://gdal.org/`). All analyses (except for future projection from climate models) were done after bilinearly interpolating to the resolution of climate data (270m) using the Climate Data Operator library (*Schulzweida*, 2017).

5.3 Methods

5.3.1 Calculation of drought indices

We consider four drought indices. Standardized precipitation index (SPI; **?**), cumulative precipitation minus evapotranspiration (PR-ET), standardized precipitation-evapotranspiration index (SPEI) and CWD. Using observed data, we calculated drought indices with integration

periods from one to six years. The cutoff of six years was chosen considering the most significant multi-year droughts during the historical period in California (https://water.ca.gov/Water-Basics/Drought). All the years here are "water years", defined as starting from October of the previous year and ending in September of the corresponding year. For example, the 4-year SPI corresponding to 2015 would be calculated from the standardized PR from Oct-2011 to Sep-2015 (i.e. water years 2012 to 2015). PR-ET and CWD were calculated in a similar manner to SPI and SPEI, but instead of standardizing, we calculated the cumulative PR-ET and CWD during the drought integration period. Such cumulative moisture deficits have been linked with physiological thresholds of tree mortality (*Anderegg et al.*, 2015; *Goulden and Bales*, 2019).

For CMIP6 ensembles, historical and future time series of each ensemble member for each grid cell were first merged to obtain a time-series spanning 1850 to 2100. SPI for 4-year integration periods was calculated from these time series.

5.3.2 Calculation of DST

To determine DST, we calculated temporal correlations between vegetation and drought indices for each pixel (for the period 1983-2011), and retained the timescale with the maximum correlation: First, the vegetation anomaly was obtained for NDMI and CWC by removing the long term median (1984-2011 for NDMI and 1990-2011 for CWC). This can be considered to be the vegetation change *e.g.*, dNDMI and dCWC). For CWD the long term (1980-2011) median was also removed (but not for SPI, SPEI and PR-ET, since they are already in anomaly form). Considering the documented delayed response of NDMI and CWC to drought (ref. *Goulden and Bales* 2019, Figure 5.A.1), a lag of 1-year was imposed between drought and vegetation anomalies in the correlation calculations. For example, in the case of dNDMI and SPI, the 1984-2012 dNDMI timeseries was correlated with the 1983-2011 water year SPI timeseries. The drought anomaly time-series were obtained for various timescales from the four drought indices and the above steps were repeated, *e.g.*, 4-year Pr-ET in 2015 is

the cumulative 2012-2015 PR-ET and the corresponding vegetation anomaly for that year is 2016 dNDMI and dCWC. Finally, the timescale giving the maximum positive correlation between vegetation anomalies and SPI, SPEI and PR-ET (or for CWD, the minimum negative correlation) was obtained as the drought timescale having maximum influence on vegetation, similar to the methodology used in ref. *Vicente-Serrano et al.* (2013). Only pixels where the correlation was significant at 80% were plotted in figures and used for analysis.

5.3.3 Random Forest Model

A random forest (RF) regression analysis was carried out to examine drivers of DTPA. RF is a non-parametric supervised machine learning algorithm (*Breiman*, 2001). It has the advantage of handling nonlinear interactions between variables. RF is widely used in ecological studies to identify the key components of complex processes and their relative importance (*Bond-Lamberty et al.*, 2014; *Kane et al.*, 2015; *Byer and Jin*, 2017; *Paz-Kagan et al.*, 2017; *Schwalm et al.*, 2017; *Anderegg et al.*, 2018). Predictor variables were selected based on previous studies: For drought-induced precipitation deficit we used the 4-year SPI of 2015 and mean evapotranspiration (*Goulden and Bales*, 2019). For the temperature anomaly and atmospheric moisture demand, we used mean PET during the drought (i.e. impact of the drought-induced temperature anomaly) (*Williams et al.*, 2013; *Allen et al.*, 2015). For resource competition, we used basal area (*Young et al.*, 2017). For forest drought tolerance, we used DST. For capacity limitation, we used AWC (*Klos et al.*, 2018) (Figure 5.A.2-5.A.3). The final random forest regression model was found to have R^2 value of 0.64. For additional details of the RF regression analysis, see the Supplementary Methods.

5.3.4 Statistical analysis and significance tests

The Pearson correlation coefficient was calculated in temporal correlation analyses. A two-tailed Student's t-test was applied to calculate p-values and statistical significance, including that of the difference in means of different scenarios of the multimodel GCM ensembles.

To obtain large geographic scale patterns of the DST from the pixel-wise analysis conducted using high resolution (270m) data, spatial smoothing was conducted. For spatial smoothing, K Nearest Neighbor (KNN) regression was applied using the python package scikit-learn (`https://scikit-learn.org/stable/`). The KNN regression algorithm employs a user-specified distance measure and a threshold K to find the nearest K neighbors to each item. It then assigns the value based on the average. The K value (the distance between points during the spatial smoothing) was taken to be 250 pixels (an approximate distance of 70 km). This was chosen as a compromise between smoothing and retaining small scale spatial features (Figure 5.A.4).

5.4 Results

5.4.1 Spatial patterns and the interpretation of DST

The drought sensitivity timescale (DST) was calculated across the Sierra Nevada (see Figure 5.3 for geographic domain) based on the relationship between SPI and NDMI (Figure 5.1a). Different forest types in the Sierra Nevada have different DST values, with mesic stands having DSTs around 3-4 years (see Supplementary Discussion). The longest drought time scales (>4 years) are seen in an elevation band around 1500-2500 m and a latitude range of 36-39°N. Lower or higher elevation forests generally have shorter timescales (<2 years), depending on latitude. The timescale generally decreases with increasing elevation south of 38.5°N. Alternative combinations of drought and canopy moisture indices revealed time scales that agreed with the spatial distribution by the SPI-NDMI analysis (Figure 5.A.5-5.A.7).

A simple interpretation of DST is that it represents the number of years required to empty a previously full, subsurface water storage under steady rate conditions. If this interpretation is correct, we should be able to multiply the mean drawdown rate by DST to predict subsurface water storage depth. We can quantify the subsurface storage depth as the maximum rootzone drying during the recent past (2003-2010) (*Maeda et al.*, 2015; *Wang-*

Erlandsson et al., 2016) (see Supplementary Discussion). Carrying out the multiplication described above, we find that the simple interpretation of DST holds remarkably well for Sierran forests (Figure 5.A.8). We further explore the drivers of DST and its interpretation in Supplementary Discussion. DST may be shaped by complicated environmental, climate and biological processes across temporal and spatial scales, but preliminary analysis shows that the factors thought to control plant water drawdown (*Fellows and Goulden*, 2017) such as mean precipitation, evapotranspiration, potential evapotranspiration, plant available water content, can account for DST variation (from a random forest regression model with R^2=0.79, Figure 5.A.9, see Supplementary Discussion). This confirms that DST reflects the plant accessible subsurface water buffer.

5.4.2 Usefulness of DST as a vegetation stress predictor

We investigated the relationship between pre-2012 DST and the subsequent trajectory of vegetation stress and mortality over the 2012-2015 drought. The triangles in Figure 5.1b-d show the progressive deepening of drought with elevation. This is measured by the normalized precipitation minus evapotranspiration (PR-ET; see triangles in Figure 5.1b-d) of each water year, accumulated since the beginning of the drought in 2012. Cumulative PR-ET during a drought can be linked to subsurface drying (*Goulden and Bales*, 2019). Cumulative PR-ET deficits in three water years (2012-2014) were severe, as shown by negative values in all elevation bins below 2700 m. By 2014, the PR-ET deficit had become extraordinarily large below 2700 m. Figure 5.1b-d represent the antecedent drought conditions affecting vegetation in the subsequent year, as portrayed in the companion panels (Figure 5.1e-g). Figure 5.1e-g show DST as a function of elevation, i.e. a collapsed version of Figure 5.1a. In 2013, the year after the beginning of the drought, there were only modest losses of canopy moisture at all elevations (Figure 5.1e). By 2014 canopy moisture loss increased for elevations where the normalized cumulative PR-ET was negative (Figure 5.1f), and by 2015 extreme canopy loss was seen at these elevations (Figure 5.1g).

In 2013, after one year of drought, some elevations showed moderate vegetation stress (Figure 5.1e), but no systematic relationship between DST and vegetation stress. However, as the drought lengthened, vegetation stress became most apparent at those elevations where DST is lowest and drought severity is high, i.e. orange/reddish dots in Figure 5.1f. (Elevations above about 2700 m are characterized by a low DST, but they did not experience severe drought and hence remained unaffected.) By 2015, after an even longer period of extreme precipitation deficit (at least 3 years), even elevations with the longest DST also showed signs of extreme canopy moisture loss. Only the highest elevations avoided moisture loss (Figure 5.1b-d). Canopy moisture loss precedes tree mortality and could ultimately trigger it (*Brodrick and Asner*, 2017; *Paz-Kagan et al.*, 2017; *Goulden and Bales*, 2019). The predictive power of DST for vegetation conditions is apparent in directly measured tree mortality, as shown in Figure 5.1e-g. Very low tree mortality is seen in 2013, similar to the background rate (*Byer and Jin*, 2017). By 2014 values were slightly higher for those elevations with signs of vegetation stress, and relatively low DST values (orange-reddish dots in Figure 5.1f). By 2015 a dramatic increase in tree mortality is seen everywhere except the highest elevations.

These results suggest that both DST and drought severity are useful predictors of the progression of vegetation stress during drought. To test this conclusion further, we examine the geographical variation in tree mortality at lower elevations of the Sierra Nevada (Figure 5.1a). Figure 5.2b shows the observed DTPA at the end of the drought. In the low elevations of the Southern Sierra, where DST is low (Figure 5.1a, Figure 5.A.6), the die-off is high. By contrast, the low elevations of the Northern Sierra, where DST is similarly low, little tree mortality occurred. Clearly the early signs of vegetation stress at low elevations (Figure 5.1f), and the higher levels of eventual tree mortality (Figure 5.1g) came from the southern portion of the Sierra Nevada. This spatial pattern appears to reflect the greater precipitation shortfall in the south relative to the north (Figure 5.2a).

To test this hypothesis, we predicted the spatial distribution of tree die-off assuming the

entire Sierra Nevada faced a precipitation deficit as large as that seen in the southern part (i.e. 4-year SPI=-2.5). The hypothetical distribution is generated with a model of DTPA based on random forest regression. As predictors, we use direct and indirect factors contributing to drought severity (4-year SPI, mean potential evaporation during the drought, mean evapotranspiration, basal area) and drought tolerance to tree die-off (DST, plant available water capacity) (model R^2=0.64). The model predicts that mesic and dry forests in central and northwestern regions of the Sierra Nevada (Figure 5.1a) suffer marked tree die-off (Figure 5.2c), consistent with their low DST values. Thus, differences in drought severity can account for the differences in tree mortality in those low elevation zones where DTS is comparably low.

To assess the potential of droughts similar to the 2012-2015 California drought in the future, we analyze future projections of multiyear precipitation variability in California simulated by ten state-of the art GCMs (see Supplementary table 1) participating in the CMIP6 (*Eyring et al.*, 2016). The simulated changes in 4-year SPI occurrence from historical (1969-2019) to future (2050-2100) under a "no emissions reduction policy" warming scenario, SSP585 (*Eyring et al.*, 2016; *O'Neill et al.*, 2016), are shown in Figure 5.3. Under climate change, the precipitation distribution shifts systematically, resulting in increased probability of severe multi-year droughts (Figure 5.3a). Examining scenarios associated with lower greenhouse gas emissions (Figure 5.3b), we see that the probability of severe droughts similar to 2012-2015 increases with growing emissions. But even for the lowest emissions scenarios, this increase in frequency is statistically significant at 99% compared to the historical simulations. We also note that the future may bring droughts even more severe than that in 2012-2015, as seen in the emergence of 4-year SPI anomalies more negative than -2.0 in the SSP585 scenario (Figure 5.3a). Such deep droughts would bring very dry conditions to large swaths of the Sierra Nevada, killing trees over areas with low DST, as in the hypothetical case of Figure 5.2c.

5.5 Discussion and Conclusions

Using multiple drought and vegetation indices spanning many decades, we obtain a drought sensitivity timescale, DST, which can also be interpreted as the plant water buffer. We find that forests on the low-elevation western slopes and high-elevation eastern slopes of the Sierra Nevada have the shortest DST, and hence the least tolerance to drought. When DST is combined with drought severity, it can be used to map the progression of vegetation stress during the 2012-2015 drought. The low elevation slopes were the first to respond to the drought as it deepened, consistent with their low DST values. However, the largest ultimate response, and the greatest tree mortality, occurred in the southern low elevations. We demonstrate that this enhanced response can be explained by the spatial patterns of drought severity. The low elevation forests in the central and northern Sierra Nevada are also vulnerable to drought and would have likely experienced extensive dieback if the 2012-2015 drought had extended further north.

Previous work suggests interannual precipitation variability in California will increase in the future (*Swain et al.*, 2018). This work, combined with the results shown here demonstrating the connection between tree mortality and multi-year drought, raise the question of whether Sierra Nevada forests will experience greater tree mortality in the future. We found that multi-year droughts in California will increase with increasing greenhouse gasses based on state-of-the-art climate model simulations from the CMIP6 project (*Eyring et al.*, 2016). The distribution of multi-year precipitation anomalies shifts to a drier regime, and the likelihood of a 4-year drought as deep (or deeper) than the 2012-2015 event increases by up to a factor of three by the end of the century. These results imply a future increase in the likelihood of tree mortality in the Sierra Nevada, especially in areas with a short DST. The low-elevation central and northern Sierran forests did not exhibit die-off in the 2012-2015 event; but this does not mean they are not vulnerable to drought. Future droughts will almost certainly be distributed differently in space from the 2012-2015 event (as were the pre-2012 droughts which allowed us to diagnose the sensitivity of the low-elevation central

and northern forests with low DST).

We note that the warmer temperatures accompanying these projected droughts (*Dai*, 2011, 2013), and that a limitation of our study is that our estimates of future drought ignore this warming effect. Warming will increase potential and actual evapotranspiration, which will further increase drought when precipitation is low; thus, our estimates represent a lower range of possible increases to drought intensity. Conversely, it is possible that plant physiological responses to elevated CO_2 may mitigate tree mortality impacts of drought, though it is unclear how much tolerance to mortality such responses confer (*Swann et al.*, 2016; *Sperry et al.*, 2019). Lastly, future climate projections are based on coarse resolution GCMs, and the spatial patterns of climate variables in this region of complex topography are inadequately represented. Future research can refine our analysis using downscaled climate model data, as well as state-of-the-art land surface and vegetation models to simulate evapotranspiration changes and physiological responses to CO_2.

Our results imply future changes in Sierra Nevada ecology. Previous work has shown that projected changes in mean climate would be associated with shifts in vegetation distribution (*Holsinger et al.*, 2019). Changes in mean conditions may lead to a decline in Sierra Nevada forests assuming current vegetation types migrate to new preferred climate zones (*Parks et al.*, 2018). These ecological transitions may be accelerated by changes in extreme events. Previous work has shown that tree mortality markedly impacts subsequent species composition and forest structure (*e.g.*, *Cobb et al.* 2017). Future increases in forest-die-off frequency and magnitude would likewise be associated with large impacts. The increase in tree mortality may increase fuel load and wildfire risk (*Ruthrof et al.*, 2016; *Stephens et al.*, 2018). Our results point to the low elevation western slopes of the Sierra Nevada as a hotspot of increasing dieoff. Conversely, other sub-regions with high drought tolerance may be more tolerant to ecological change, and may even become refugia (*Morelli et al.*, 2016; *McLaughlin et al.*, 2017). The drought timescale metric and results we show potentially provide information that may aid conservation planning.

Acknowledgements. We acknowledge the World Climate Research Programme's Working Group on Coupled Modelling, which is responsible for CMIP6, and we thank the climate modelling groups for producing and making available their model output. We also thank the Earth System Grid Federation (ESGF) for archiving the data and providing access, and various funding agencies who support CMIP6 and ESGF. This research was funded by the University of California Laboratory Fees Research Program. CDK is supported by the Department of Energy, Office of Science, Office of Biological and Environmental Research through the Early Career Research Program administered by the Regional and Global Model Analysis Program. GDM would like to thank Neil Berg for assistance and discussions on early ideas of this paper.

5.6 Figures

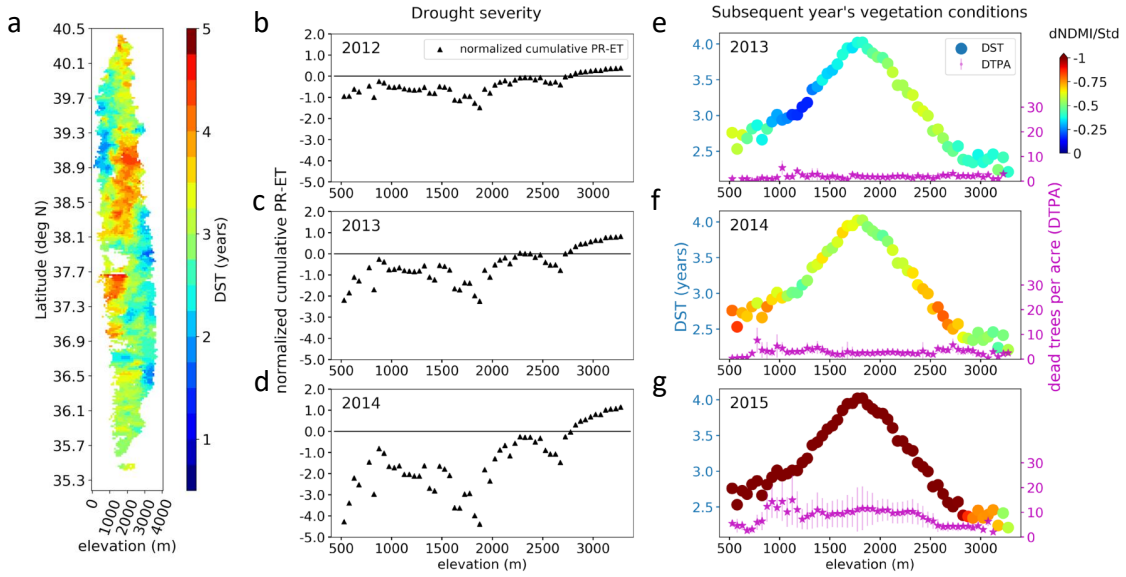

Figure 5.1: Relationships among DST, drought conditions, and vegetation condition change during the 2012-2015 drought in Sierra Nevada, California. a, Spatial patterns of the drought sensitivity timescale (DST; years) associated with the NDMI anomaly during 1983-2011 period for SPI. Only regions dominated by conifers, unimpaired from wildfires, and with a statistically significant maximum correlation between NDMI and SPI of over 80% are shown. b-d, Drought conditions, elevation binned. The normalized cumulative precipitation minus evapotranspiration (PR-ET) for each water year since the start of the drought, 2012. Cumulative PR-ET of each year was normalized by the 1980-2011 mean PR-ET. e-g, Vegetation conditions associated with the year after the year shown directly to the left in panels b-d; the elevation-binned change in NDMI, dNDMI, divided by standard deviation (circles with the colorbar), and dead trees per acre (DTPA, magenta stars). dNDMI was calculated with respect to 2009-2011 mean NDMI as in ref. *Goulden and Bales* (2019). Error bars represent ±0.5 of the standard deviation. For panels b-g, the elevation bin width is 50 m, and the x-axis is the mean elevation value of each elevation bin. In panels b-g, only cold, mesic and dry forests (see Supplementary Discussion) were included for this analysis. The few grid cells where the mean PR-ET was less than zero were removed from data shown in panels b-g.

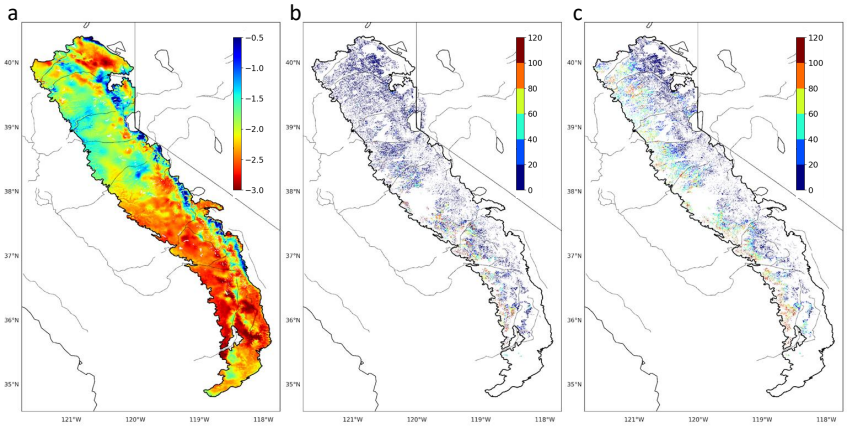

Figure 5.2: Precipitation deficit and tree die-off in Sierra Nevada, California. a, The 4-year Standardized precipitation Index (SPI) of 2015. b, Observed dead trees per acre during the 2012-2015 drought (DTPA), calculated as the maximum number of dead trees observed at any time in areal detection surveys done by USFS during the summers of 2013-2016. c, Dead trees per acre predicted using the random forest model (see Methods) for a 4-year drought with a uniform 4-year SPI of -2.5 over whole Sierra Nevada forests. In b and c, only the regions dominated by conifers, unimpaired by wildfires, and which have a statistical significance for the maximum correlation between NDMI and SPI over 80% are shown.

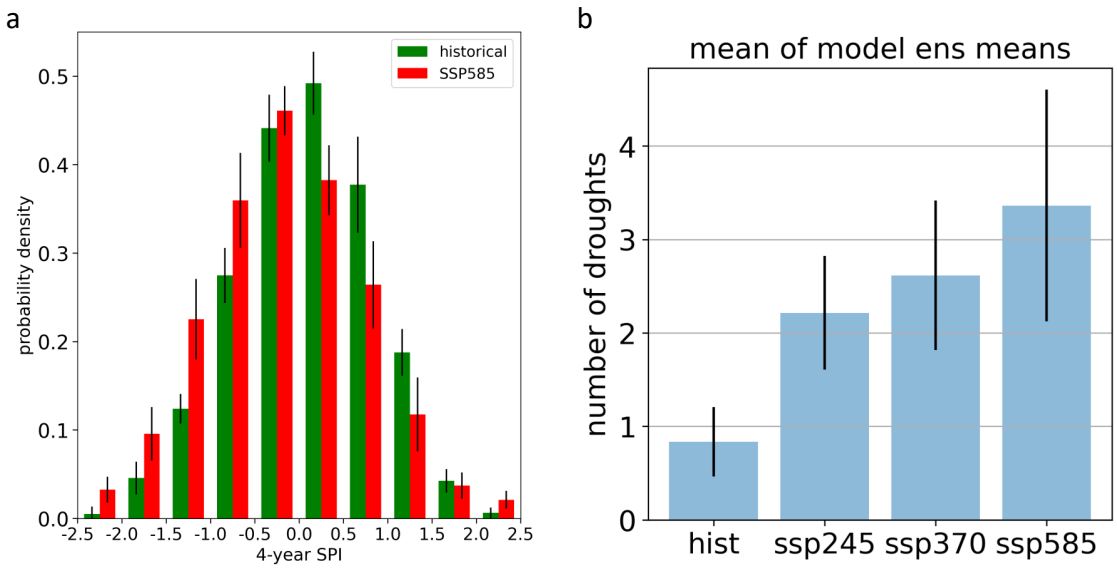

Figure 5.3: Future projections of precipitation and increase in extreme droughts in California. a, Historical (1969-2019) and projected future (2050-2100) distributions of 4-year SPI from available CMIP6 models for California. The future projection is based on the forcing scenario SSP5-8.5. For each model, all 4-year SPI values from all ensembles were averaged over California, pooled together, and binned for the SPI range -2.5 to 2.5. The bin width is 0.5. The multimodel mean and the standard deviation of each bin are shown. b, Historical (1969-2019) and projected future (2050-2100) frequency of droughts severe than the 2012-2015 drought from the available CMIP6 models, based on 4-year SPI. Three future forcing scenarios spanning a large range of future emissions outcomes are shown (SSP2-4.5, SSP3-7.0 and SSP5-8.5). Error bars represent ±0.5 of the standard deviation. The California area-averaged observed 4-year SPI for the recent drought was taken as -1.71 from the west-wide drought tracker (`https://wrcc.dri.edu/wwdt/`).

Appendix

5.A Supplement

5.A.1 Interpretation of DTS

To test the simple hypothesis that the DST represents the ratio between possible maximum subsurface storage depth and dry season plant water uptake, the following data were obtained. California dry season soil water drawdown calculated using a spatially resolved water balance model (*Fellows and Goulden*, 2017) was used. Monthly satellite-derived (Moderate Resolution Imaging Spectroradiometer) evapotranspiration calculated using Operational Simplified Surface Energy Balance model (*Senay et al.*, 2013) was obtained at 30 arc seconds for 2003-2010.

Following the methodology used in ref. *Wang-Erlandsson et al.* (2016), an approximate subsurface storage depth estimation was done by calculating the running estimate of monthly rootzone reservoir deficit. The deficit is controlled by the difference between outflow from the system (i,e, evapotranspiration) and inflow to the system (i.e. precipitation), for each pixel for 2003-2010. This period was selected considering the availability of monthly observed ET data, and to limit the analysis to pre-drought conditions. Excess inflow is assumed to be removed from the system as runoff or deep drainage. The maximum of this deficit is taken as the estimate of subsurface storage. This method does not include all internal and external water fluxes. This method may not be accurate for regions where the ignored components such as runoff have a larger influence. However, this method has been shown to provide reasonably accurate estimates (*Wang-Erlandsson et al.*, 2016) and therefore is adequate as a first estimate in our study (Figure 5.A.8).

5.A.2 Possible controlling factors of DTS

Given the above simple interpretation of DTS, potential drivers of DTS were chosen under the hypothesis that DTS represents the plant water buffer. The plant water buffer is mainly controlled by the soil capacity to hold plant available water (*Klos et al.*, 2018) (represented by available water capacity or AWC), amount of water supply (represented by mean precipitation or PR), atmospheric evaporative demand (mean potential evapotranspiration or PET) and vegetation water utilization (*Fellows and Goulden*, 2017) (mean evapotranspiration or ET) (Figure 5.A.3). A random forest regression analysis show that overall, the DTS variable is well accounted for (R^2=0.79) by these four environmental, climate and vegetation drivers (see Supplementary Methods below for more details on the regression model). Among the four drivers, AWC has the greatest relative importance (30.7%), followed by PR (28.9%), ET (22.5%) and PET (17.9%) (Figure 5.A.9).

Figure 5.A.5 illustrates relationships among DTS and the four drivers for each forest type individually. In cold forests, DTS increases with all four drivers (see also Figure 5.A.11). These forests are likely water-limited, and very likely storage-limited, due to factors such as a Pleistocene glaciation and cold temperature limits to soil weathering (*Fellows and Goulden*, 2017). Therefore, the water buffer is limited by water availability, and increases with AWC and PR. In mesic forests, PR is higher than cold forests. They have the longest DTS (around 4 years). While AWC, PET and ET increase with PR in mesic forests, DTS shows a slight decrease towards the highest PR levels. This may be a consequence of significantly larger atmospheric water demand. In dry forests, DTS ranges between that of cold and mesic forests, with a mean value around 2 to 3 years. Dry forests have the highest PR and AWC values, similar to mesic forests. But dry forests also have the highest median PET. Even though PR could be stored in these soils with a relatively high AWC, high PET and ET means the drawdown is consistently higher. There is consequently little water in the deepest soil layers. Thus, the plants are likely not adapted to utilize the full AWC, effectively reducing the size of the water buffer. This has the effect of reducing DTS, and DTS values for dry forests are

in between those of cold and mesic forests. The arguments above are consistent with the idea that plant rooting depth is strongly linked to the magnitude and seasonality of environmental and climate variables (*Guswa*, 2008; *Kleidon and Heimann*, 1998) and hence is included implicitly in our analysis. These simple but robust results showing drought resistance control by environmental, climate and vegetation drivers is supported by theoretical, observational and modeling studies. These studies also link variables related to water availability to plant resistance to drought (*Fellows and Goulden*, 2017; *McDowell et al.*, 2019; *Tai et al.*, 2017; *McLaughlin et al.*, 2017).

5.A.3 Supplementary Methods

We present here some further details of our methods, for the purposes of reproducibility.

Random forest regression : An ensemble of decision trees is created by the algorithm, which separates the training data into subpopulations based on the maximum information gained (*Breiman*, 2001). We used Python scikit-learn package for the RF calculations. For RF hyperparameters, we selected the maximum number of levels in each decision tree ('max˙depth'). This gave the maximum coefficient of determination (R^2) value for the training set, using scikit-learn GridSearchCV option, with 5 cross validations. The maximum number of features considered during node splitting ('max˙features') was set to 'sqrt'. Default parameters in the model were otherwise used. RF model fitting was done for a randomly selected portion of the data (70%), leaving the remaining 30% for testing. Model accuracy was calculated as the R^2 for the test data set. The importance of the predictors (feature importance) was calculated as the out-of-bag permutation importance. Here the reduction of baseline accuracy measure (R^2) is used as the importance of that feature, after performing permutation for each feature. For this we used the PermutationImportance function of the Python package ELI5 (https://eli5.readthedocs.io/en/latest/overview.html). We normalized the feature importance to have a sum of 1 (Figure 5.A.9-5.A.11). Partial dependence plots were obtained for each regressor to interpret the relationship with the dependent variable

(Figure 5.A.10).

All relevant climate and environmental variables used here were checked for multicollinearity prior to regression analysis. Spearman rank correlation was calculated between all variables to avoid high collinearity (absolute correlation>0.5, following ref. *Paz-Kagan et al.* 2017). Next, a variance inflation factor (VIF) was calculated for regressor variable sets and confirmed that each variable has a VIF less than 2.

Vegetation reclassification: To examine DST of broader vegetation classes in Sierra Nevada, a vegetation reclassification was carried out. Gridded vegetation data were obtained from LANDFIRE dataset (*Rollins*, 2009) and the Existing Vegetation Type layer was reclassified into five broad categories: mesic, cold, dry, shrubland/grassland and sparse/barren, following the classification presented in ref. *Parks et al.* (2018).

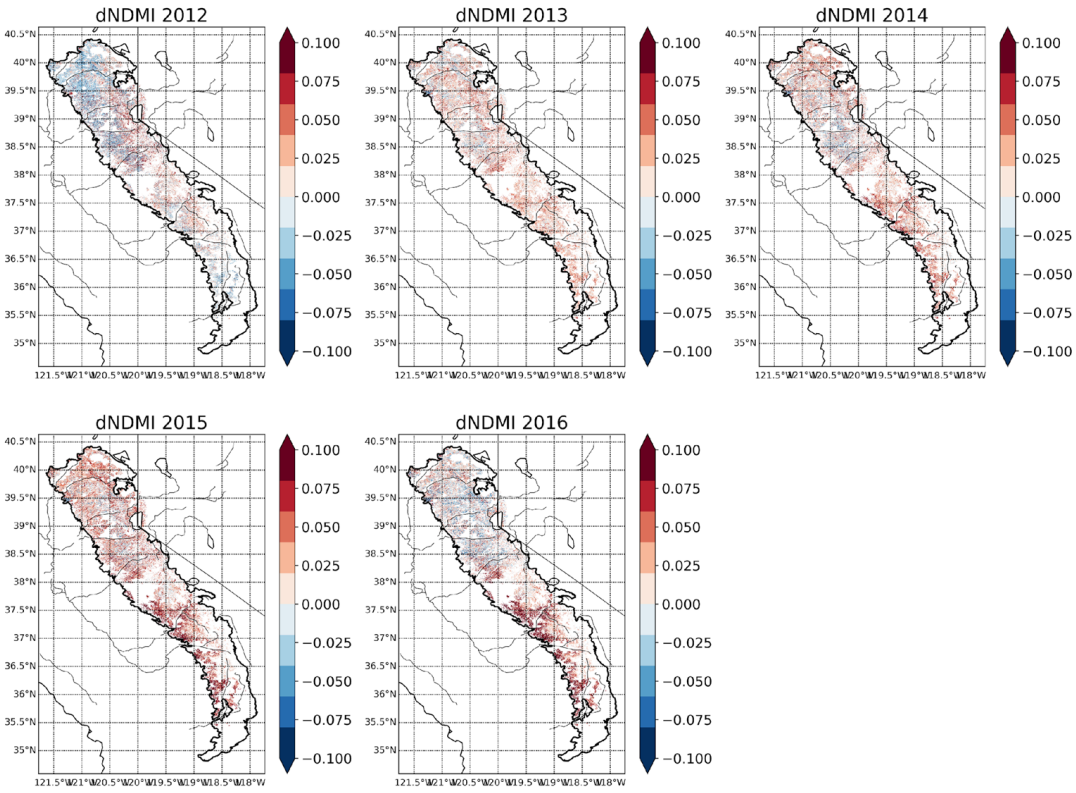

Figure 5.A.1: 2012-2015 drought induced NDMI change. NDMI anomaly with respect to 2009-2011 mean during 2012-2016.

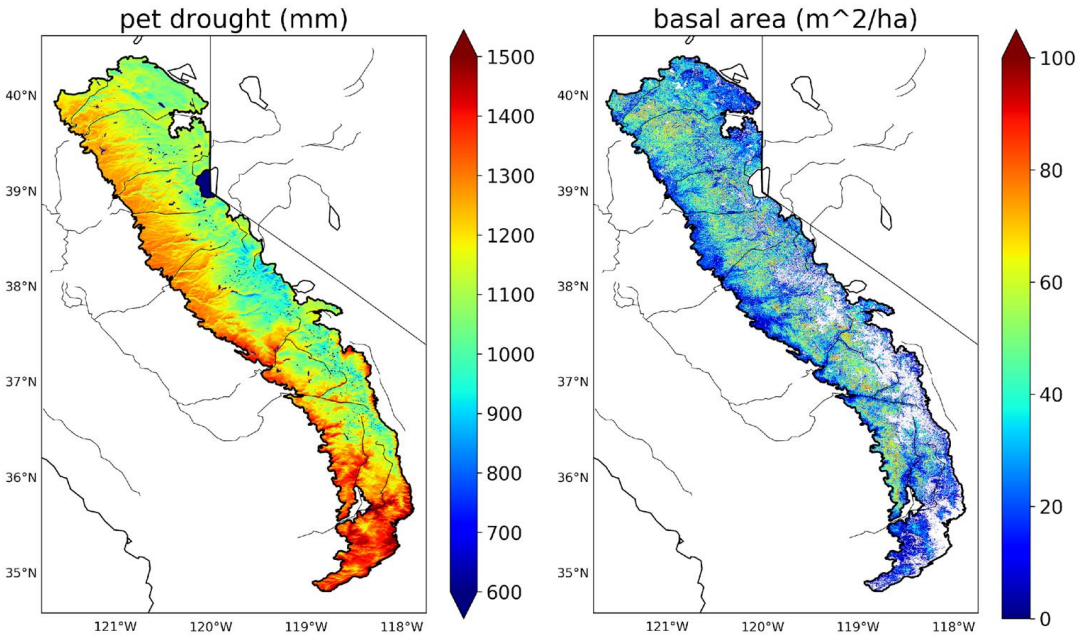

Figure 5.A.2: Correlates of the random forest model for DTPA. Mean pet during the drought (left), mean basal area (right).

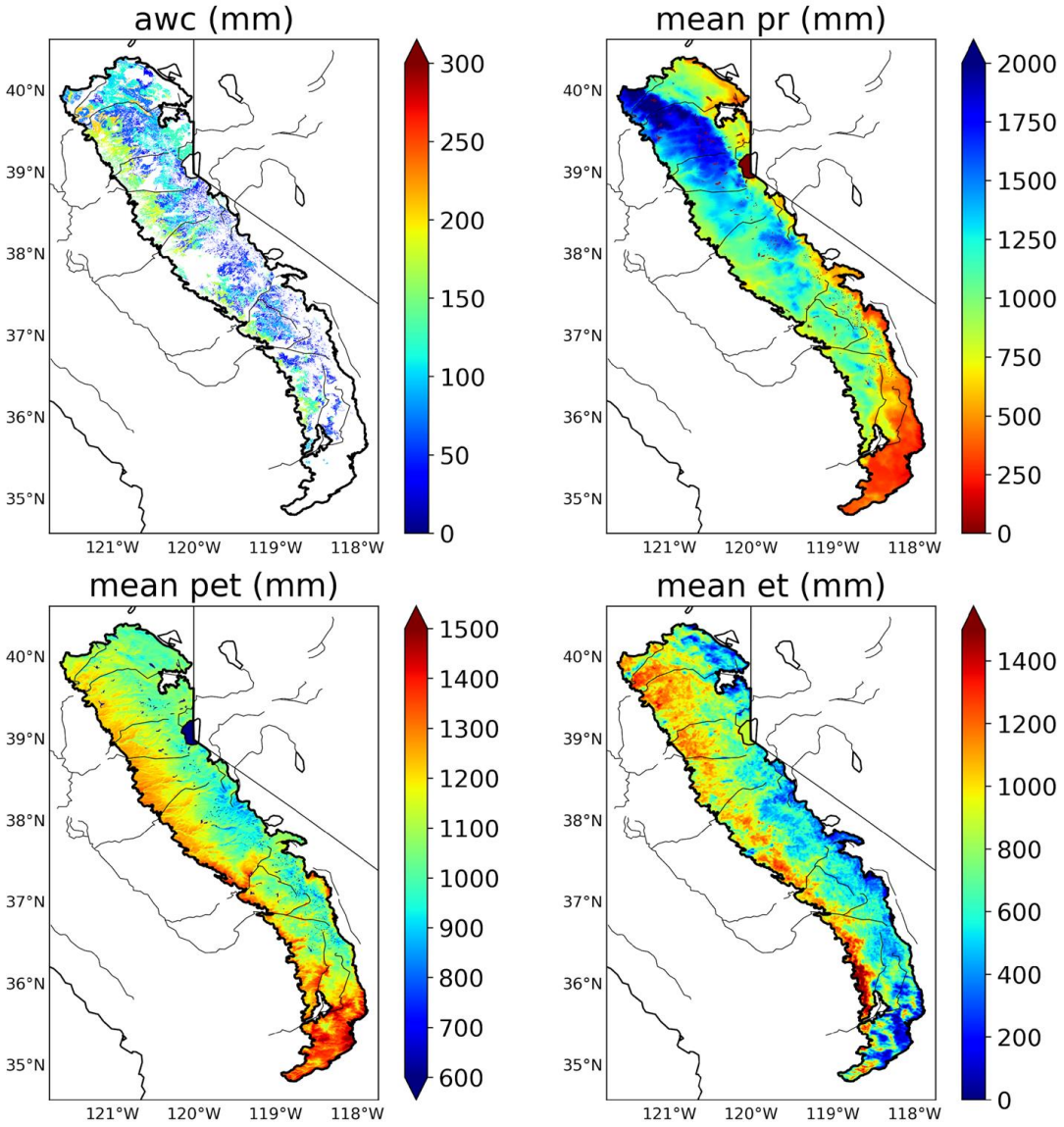

Figure 5.A.3: Correlates of the random forest model for DST. awc (top left), mean pr (top right), mean pet (bottom left), mean et (bottom right). awc and mean et are used for modeling DTPA as well.

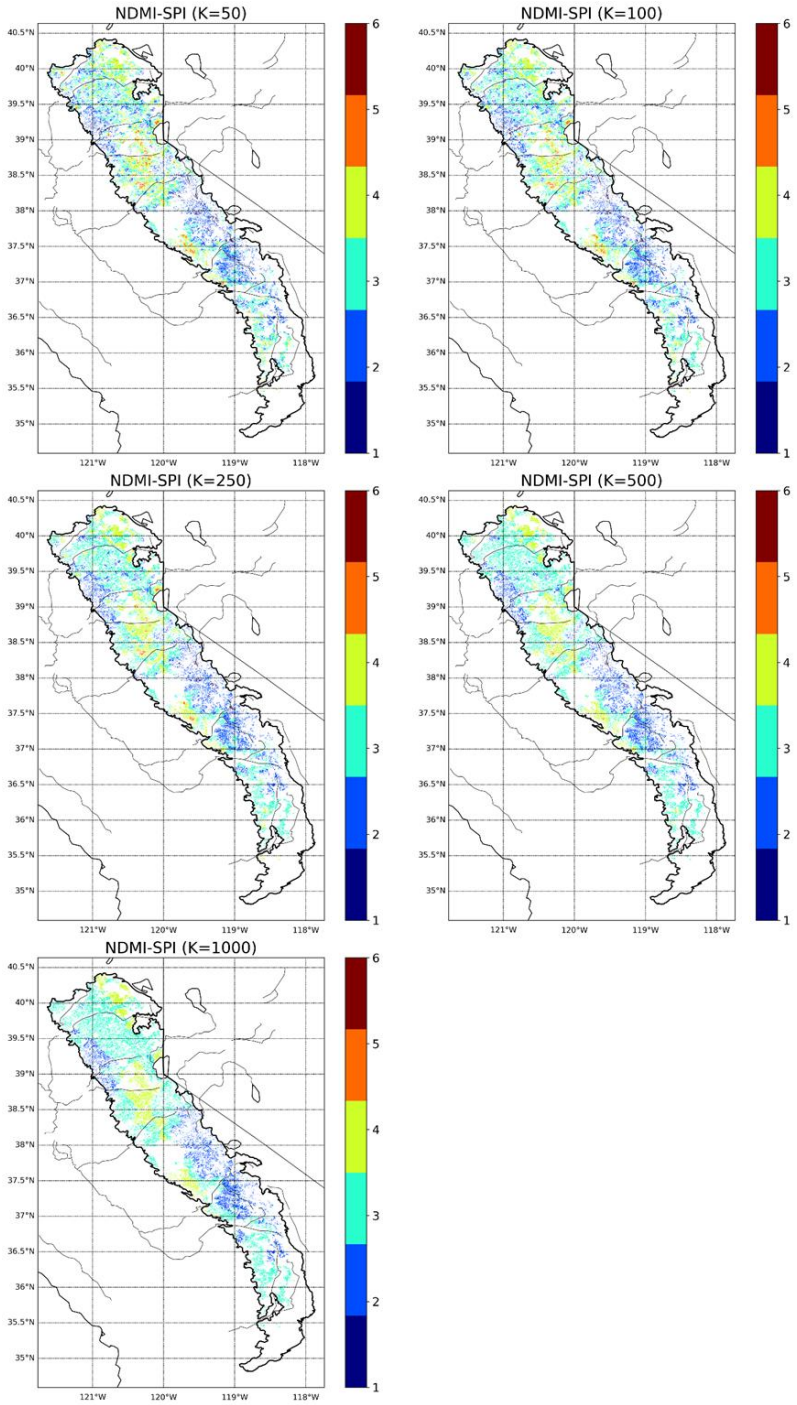

Figure 5.A.4: Spatial smoothing of DST. DST for SPI and NDMI, for different K values used for spatial smoothing using KNN algorithm.

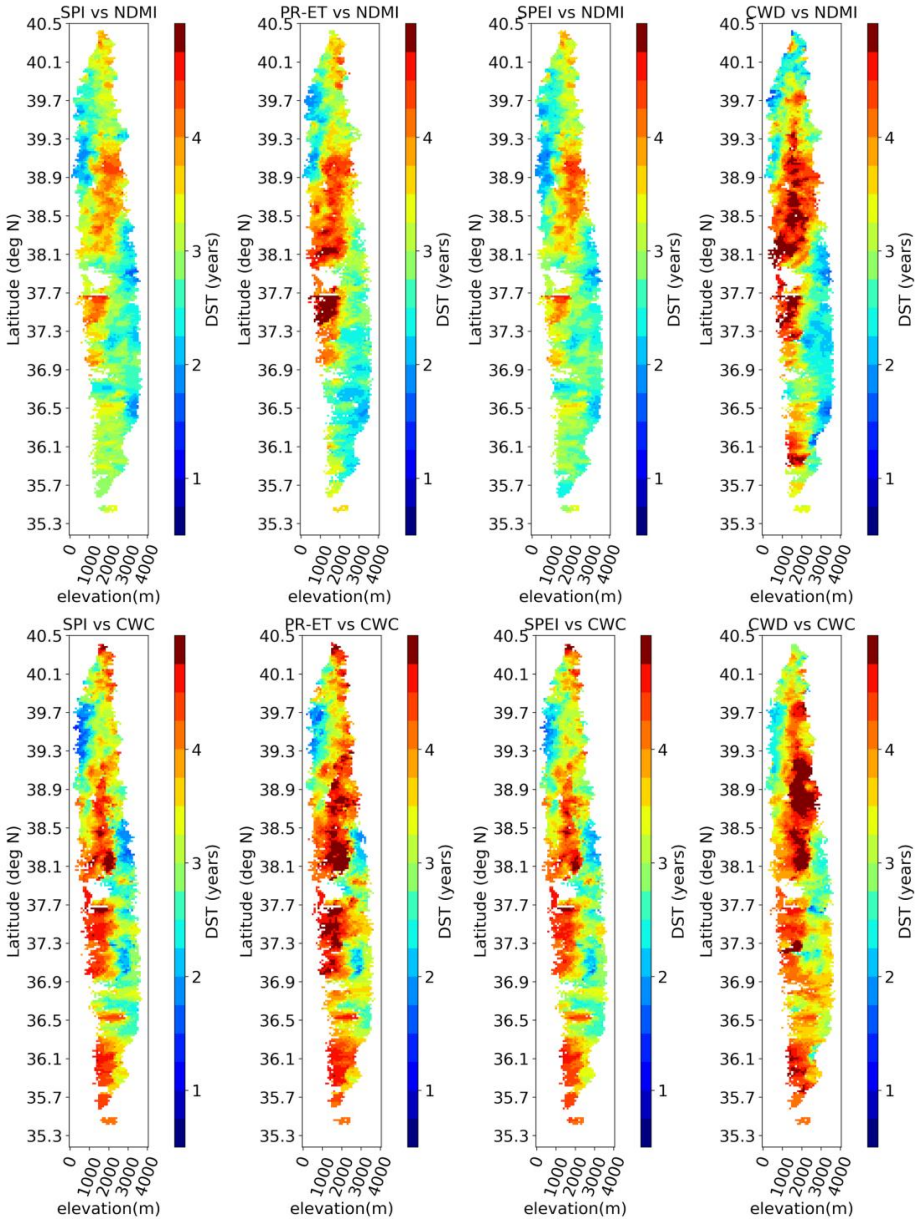

Figure 5.A.5: Spatial patterns of DST. For drought metrics standardized precipitation index (SPI), cumulative precipitation minus evapotranspiration (PR-ET), climatic water Deficit (CWD) and standardized precipitation evapotranspiration index (SPEI) and NDMI (left panels), CWC (right panels), binned with respect to elevation and latitude. Only grid cells where the correlation is significant at 80% are shown and used for rest of the analyses.

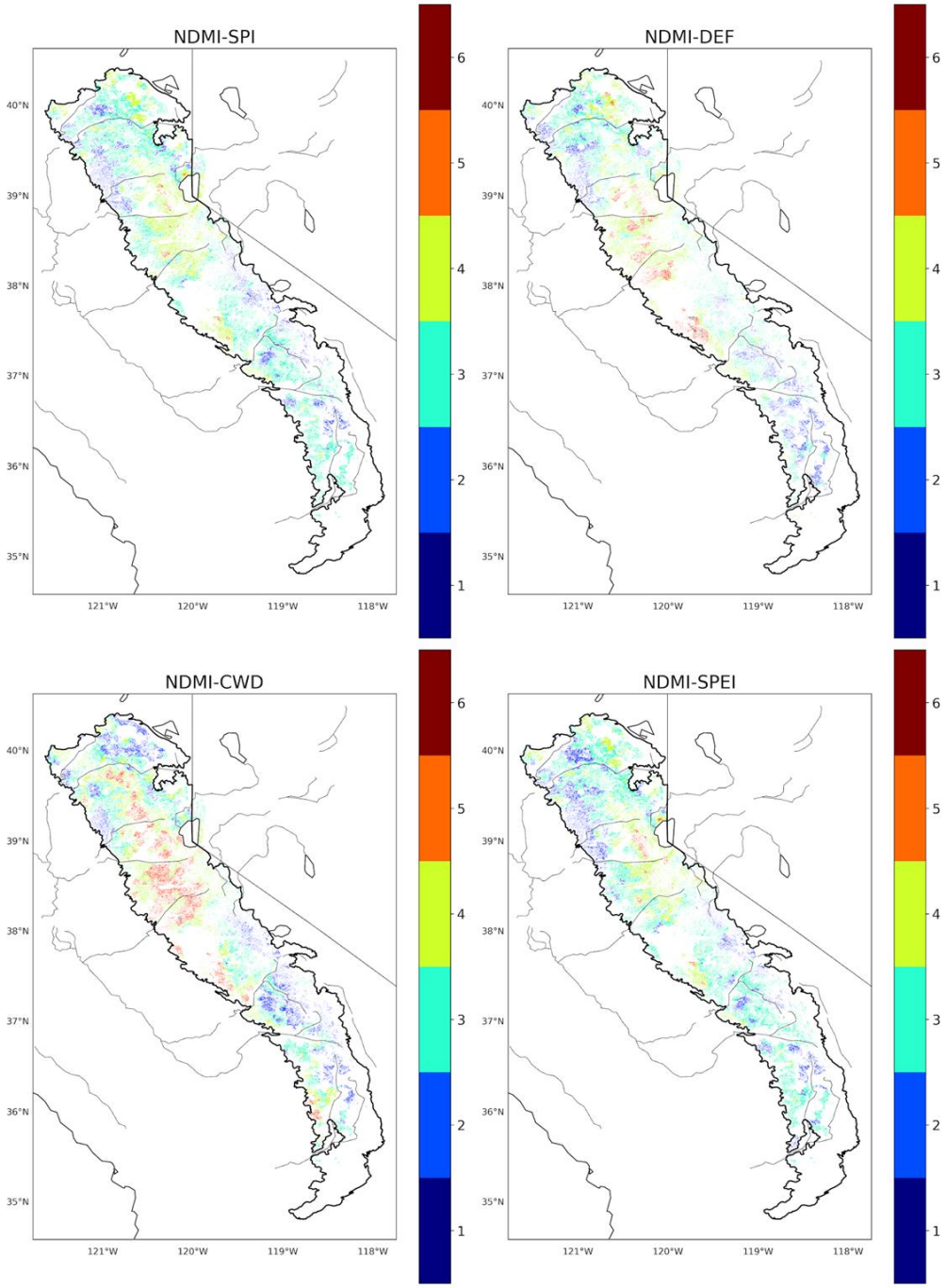

Figure 5.A.6: Spatial maps of DST. DST (years) associated with the NDMI anomaly during 1983-2011 period for SPI, cumulative PR-ET (DEF), CWD, SPEI. Only grid cells where the correlation is significant at 80% are shown and used for rest of the analyses.

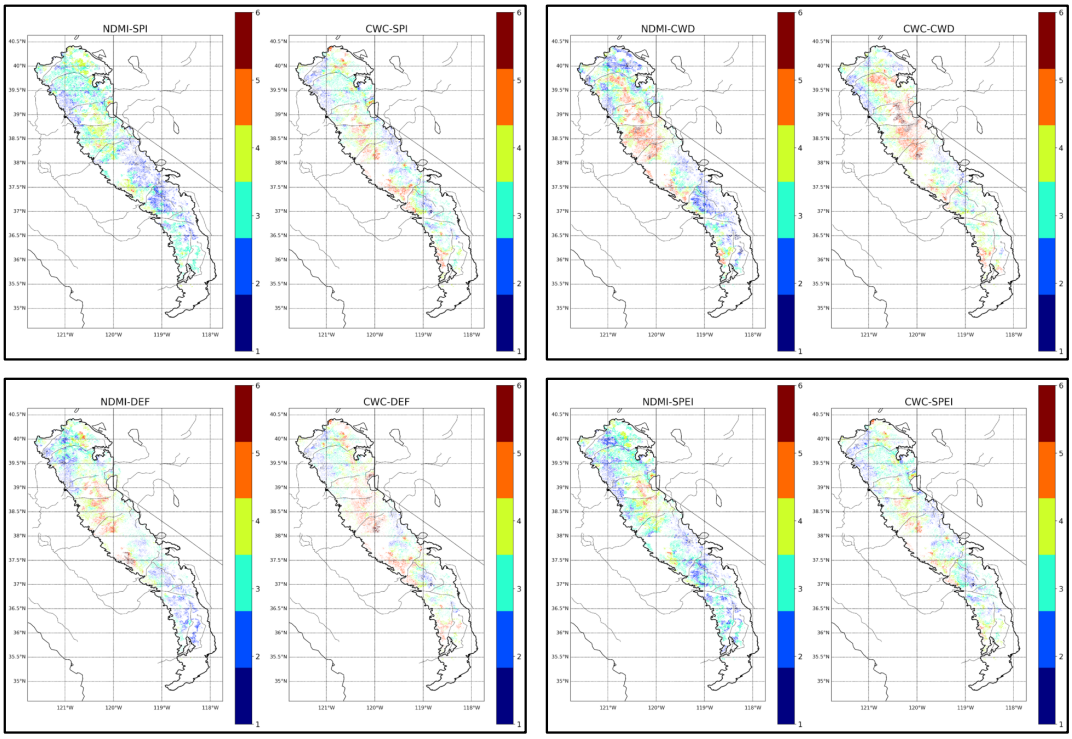

Figure 5.A.7: Comparison between NDMI and CWC. Maximum drought timescale (DST ; years) comparison between NDMI and CWC Only grids where the correlation is significant at 80% are shown and used for rest of the analyses.

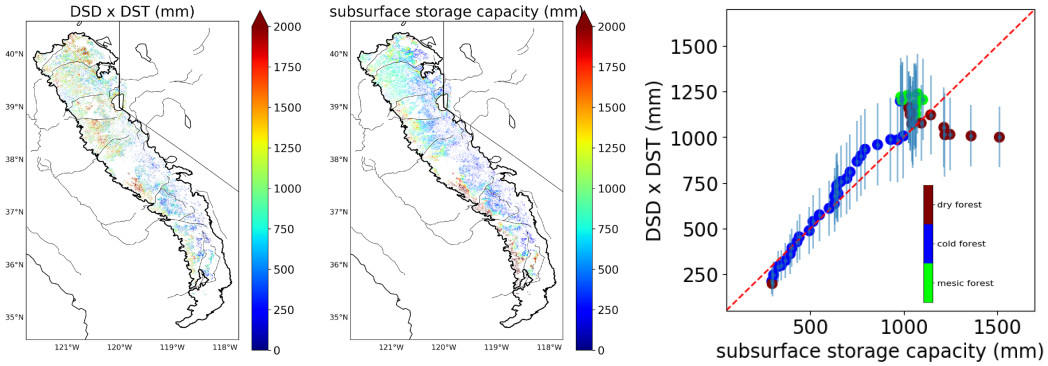

Figure 5.A.8: Simple interpretation of DTS. Mean dry season water drawdown (DSD ; mm) calculated in ref. *Fellows and Goulden* (2017) (left), sub surface storage capacity (mm) calculated following the methodology in ref. *Wang-Erlandsson et al.* (2016) (middle), comparison between DSD multiplied by DST and sub surface storage capacity, binned by elevation (left). Error bars represent ±0.5 of the standard deviation. Red dashed line is the 1:1 line. Color of the markers show the median vegetation class for each bin.

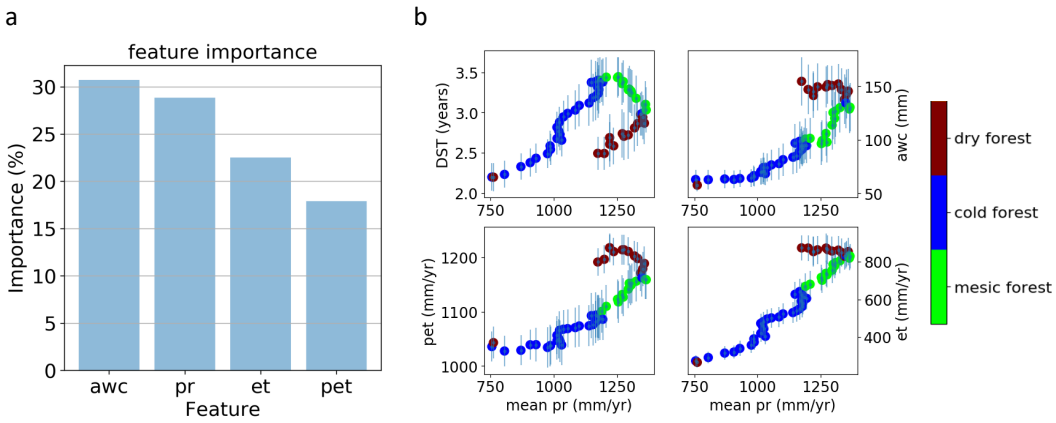

Figure 5.A.9: a, Feature importance for the possible drivers of DST from Random Forest regression. Predictor variables used are: plant available water content (awc), mean precipitation (pr), mean evapotranspiration (et) and mean potential evapotranspiration (pet). b, Relationships between DST and mean pr binned by elevation (top left), the relationship between mean awc and mean pr binned by elevation (top right), the relationship between mean pet and pr binned by elevation (bottom left)), and the relationship between et and pr binned by elevation (bottom right). Elevation binning was done for 50 m elevation bins. Bins with items less than 100 were excluded. Scatter plot values and the color of the markers show the mean value of each variable and median vegetation class for each bin, respectively. Error bars represent ±0.5 of the standard deviation.

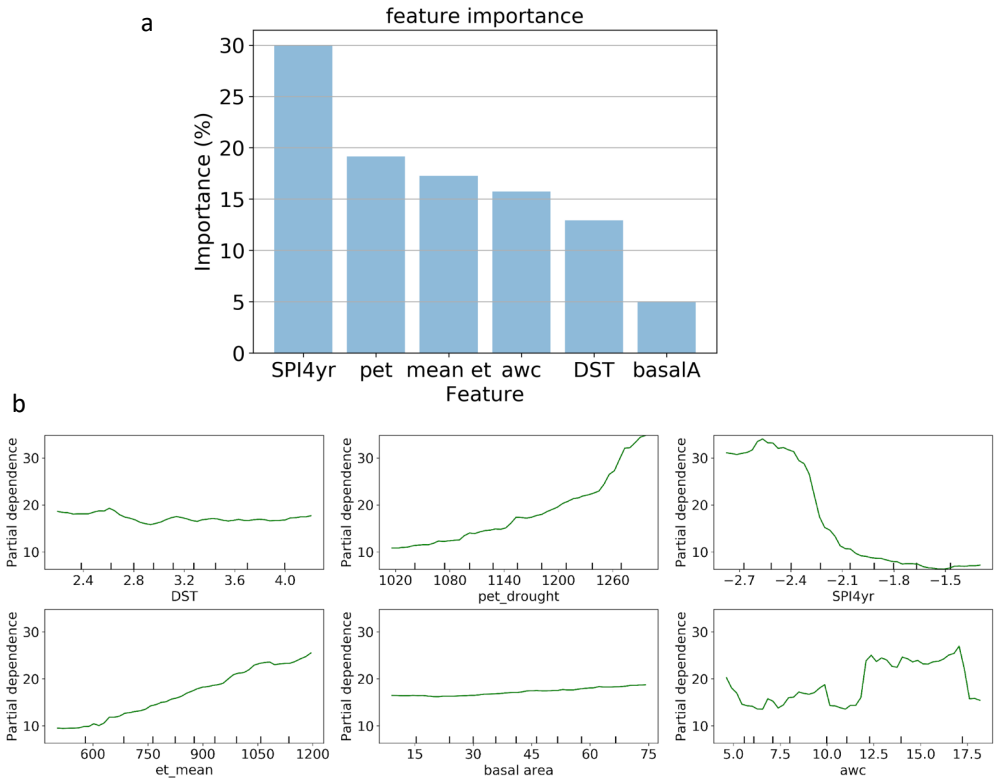

Figure 5.A.10: Random Forest regression model for modeling tree mortality. a, The feature importance for the possible drivers of DTPA from Random Forest regression. The predictor variables used for the regression are: 4 year SPI of 2015 (SPI4yr), mean potential evapotranspiration during the 2012-2015 drought (pet), mean evapotranspiration (mean˙et), plant available water content (awc), maximum drought timescale (DST) and basal area (basalA). b, DTPA from Random Forest regression based partial dependence of DTPA on drivers DST, mean PET during the drought, SPI 4-year, mean et, basal area and AWC.

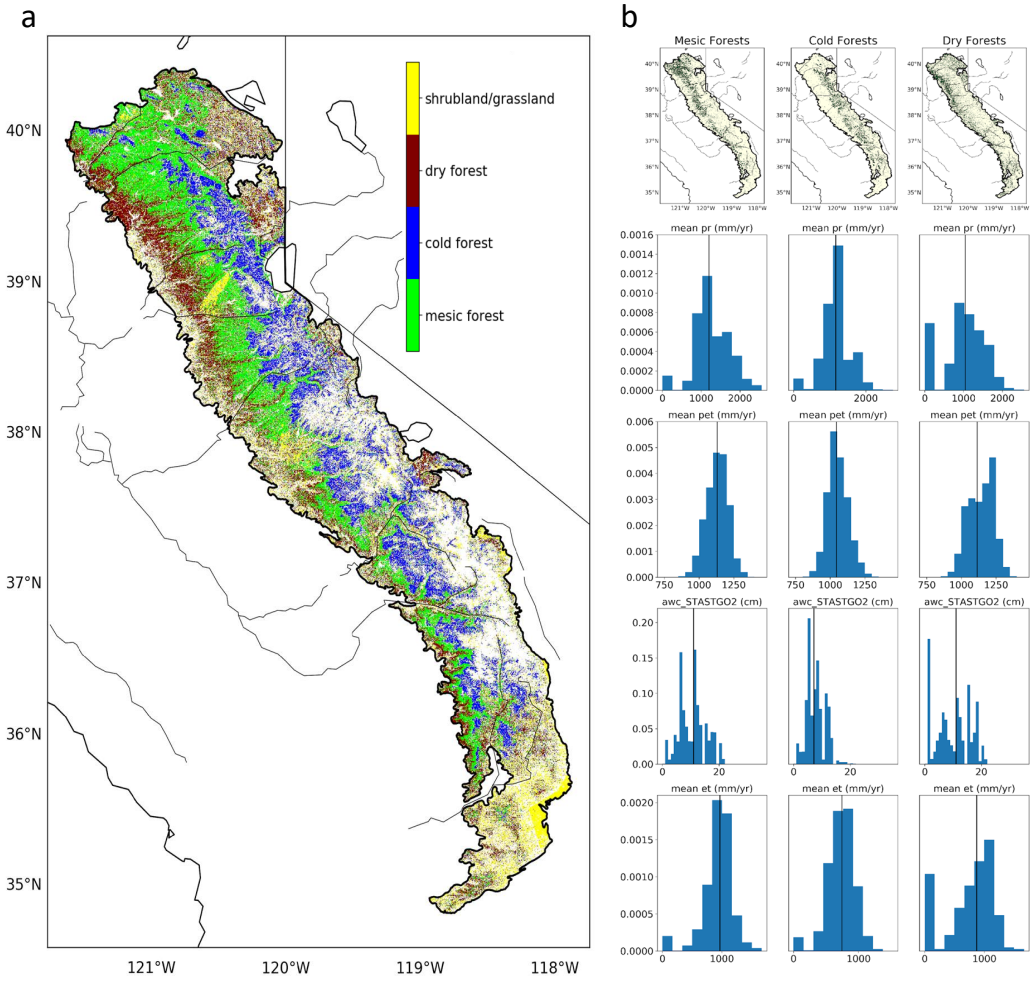

Figure 5.A.11: Broader vegetation types of Sierra Nevada. a, Pacific Southwest National Forests. Data US Forest Service Forest Datasets (`https://www.fs.usda.gov/main/r5/landmanagement/gis`) (left). Broader vegetation classes for Sierra Nevada (right). White regions inside Sierra Nevada boundary represent open water, perennial ice/snow, barren land, sparsely vegetated, non vegetated or open water. b, Broader vegetation classes for Sierra; Mesic, Cold and Dry forest spatial distribution and the mean PR, mean PET, AWC and ET histograms for each vegetation type. Left, middle and right columns represent Mesic, Cold and Dry forests, respectively.

Table 5.A.1: Coupled Model Intercomparison Project version 6 models used in this study and their ensemble members.

Model	Ensembles used
ACCESS-ESM1-5	rNi1p1f1 (N = 1 to 3)
CanESM5	rNi1p1f1, rNi1p2f1 (N = 1 to 25)
CanESM5-CanOE	rNi1p2f1 (N = 1 to 3)
CNRM-CM6-1	rNi1p1f2 (N = 1 to 6)
CNRM-ESM2-1	rNi1p1f2 (N = 1 to 5)
EC-Earth3-Veg	rNi1p1f1 (N = 1, 2)
GISS-E2-1-G	rNi1p1f2, rNi1p3f1 (N = 1)
IPSL-CM6A-LR	rNi1p1f1 (N = 1 to 4, 6, 14)
MIROC6	rNi1p1f1 (N = 1 to 3)
MPI-ESM1-2-LR	rNi1p1f1 (N = 1 to 10)

CHAPTER 6

Final conclusions and future work

6.1 Final conclusions

This dissertation delves into the changes of the hydrologic cycle due to climate change and climate variability, focusing particularly on precipitation patterns and their implications for human and ecological systems. It leverages data-driven methods to parse out the signal of climate change from the noise of climate variability and model uncertainties across different spatial and temporal scales. Employing a range of ML techniques, from linear regression models to complex neural networks, previous chapters aim to discern the climate change signal in historical and future precipitation patterns globally and at a continental level, alongside investigating the effects of climate variability and change on wildfire characteristics and drought impacts on forests within California's ecosystems. Chapter 2 provides evidence of an anthropogenic fingerprint in historical precipitation data, overcoming limitations of previous studies by harnessing spatiotemporal data variability. Chapter 3 shifts focus to future precipitation projections, introducing an ML framework to constrain uncertainties in atmospheric circulation dynamics, thus refining regional precipitation forecasts. Chapter 4 and 5 examine the historical and projected impacts of climate change on wildfire onset and forest drought resilience in California, highlighting the critical role of climate in driving these phenomena and underscoring the potential of ML models to predict and manage future environmental challenges.

6.2 Future work

This dissertation applies various ML frameworks to understand the changes in the hydrologic cycle and the impacts of these changes and variability. The following follow-up analyses are either in progress or being planned as future work:

1. The signal detection method used in Chapter 2 focuses on global-level signals. Current work involves modeling the complete, spatiotemporally resolved global forced signal using advanced ML techniques and multi-model large ensembles of climate model simulations (*Deser et al.*, 2020). A large ensemble can provide the spatiotemporal forced response as the ensemble mean, allowing for training an ML algorithm to model the forced response from raw data, which includes internal variability and climate model uncertainty.

2. The emergent constraint presented in Chapter 3 can be followed up with analyses designed to elucidate the model parameter choices leading to the spread in the Atmospheric Turnover Circulation (ATOC). The moist static energy balance and the gross moist stability framework, which show promise, will be considered for this.

3. Wildfire season onset in California is examined in detail in Chapter 4, and an attribution study was carried out for the variability and change of the historical onset time series. In follow-up studies, other temporal characteristics of the fire season, such as the fire season's end, will be examined.

4. Chapter 4 demonstrated a decrease in human ignitions across California's ecoregions throughout the year. We are conducting a study to investigate the spatial footprint of this change in human ignitions and the possible reasons behind this temporal change.

5. The drought sensitivity timescale introduced in Chapter 5 has the potential to identify drought refugia. Future studies will include a detailed analysis of this aspect of California's ecosystem.

Answering the above research questions with the aid of ML techniques will deepen our understanding of how climate change and climate variability manifest in climate simula-

tions. Moreover, these analyses will shed light on the societally relevant impacts of these changes, ultimately contributing to more informed decision-making processes and adaptation strategies.

Bibliography

Abatzoglou, J. T., and C. A. Kolden (2011), Climate change in western us deserts: Potential for increased wildfire and invasive annual grasses, *Rangeland Ecology Management*, *64*(5), 471–478, doi:10.2111/REM-D-09-00151.1.

Abatzoglou, J. T., and A. P. Williams (2016), Impact of anthropogenic climate change on wildfire across western us forests, *Proceedings of the National Academy of Sciences of the United States of America*, *113*(42), 11,770–11,775, doi:10.1073/pnas.1607171113.

Abatzoglou, J. T., S. Z. Dobrowski, S. A. Parks, and K. C. Hegewisch (2018), Terraclimate, a high-resolution global dataset of monthly climate and climatic water balance from 1958-2015, *Scientific Data*, *5*, Article 170,191, doi:10.1038/sdata.2017.191.

Alexander, L. V., M. Bador, R. Roca, S. Contractor, M. Donat, and P. Nguyen (2020), Intercomparison of annual precipitation indices and extremes over global land areas from in situ, space-based and reanalysis products, *Environmental Research Letters*, *15*(5), 055,002, doi:10.1088/1748-9326/ab79e2.

Allan, R. P., and B. J. Soden (2008), Atmospheric warming and the amplification of precipitation extremes, *Science*, *321*(5895), 1481–1484, doi:10.1126/science.1160787.

Allan, R. P., M. Barlow, M. P. Byrne, A. Cherchi, H. Douville, H. J. Fowler, T. Y. Gan, A. G. Pendergrass, D. Rosenfeld, A. L. Swann, and L. J. Wilcox (2020), Advances in understanding large-scale responses of the water cycle to climate change, *Annals of the New York Academy of Sciences*, *1472*(1), 49–75.

Allen, C. D., D. D. Breshears, and N. G. McDowell (2015), On underestimation of global vulnerability to tree mortality and forest die-off from hotter drought in the anthropocene, *Ecosphere*, *6*, 1–55, doi:10.1890/ES15-00203.1.

Allen, C. D., et al. (2010), A global overview of drought and heat-induced tree mortality reveals emerging climate change risks for forests, *Forest Ecology and Management*, *259*, 660–684, doi:10.1016/j.foreco.2009.09.001.

Allen, M. R., and W. J. Ingram (2002), Constraints on future changes in climate and the hydrologic cycle, *Nature*, *419*(6903), 224–232.

Anderegg, L. D. L., W. R. L. Anderegg, and J. A. Berry (2013), Not all droughts are created equal: Translating meteorological drought into woody plant mortality, *Tree Physiology*, *33*, 701–712, doi:10.1093/treephys/tpt044.

Anderegg, W. R. L., A. Flint, C. Huang, L. Flint, J. A. Berry, F. W. Davis, J. S. Sperry, and C. B. Field (2015), Tree mortality predicted from drought-induced vascular damage, *Nature Geoscience*, *8*, 367–371, doi:10.1038/ngeo2400.

Anderegg, W. R. L., et al. (2018), Hydraulic diversity of forests regulates ecosystem resilience during drought, *Nature*, *561*, 538–541, doi:10.1038/s41586-018-0539-7.

Asner, G. P., P. G. Brodrick, C. B. Anderson, N. Vaughn, D. E. Knapp, and R. E. Martin (2016), Progressive forest canopy water loss during the 2012-2015 california drought, *Proceedings of the National Academy of Sciences of the United States of America*, *113*(2), E249–E255, doi:10.1073/pnas.1523397113.

Bach, S., A. Binder, G. Montavon, F. Klauschen, K.-R. Müller, and W. Samek (2015), On pixel-wise explanations for non-linear classifier decisions by layer-wise relevance propagation, *Plos One*, *10*(7), e0130,140, doi:10.1371/journal.pone.0130140.

Bador, M., L. V. Alexander, S. Contractor, and R. Roca (2020), Diverse estimates of annual maxima daily precipitation in 22 state-of-the-art quasi-global land observation datasets, *Environmental Research Letters*, *15*(3), 035,005, doi:10.1088/1748-9326/ab6a22.

Balch, J. K., B. A. Bradley, J. T. Abatzoglou, R. C. Nagy, E. J. Fusco, and A. L. Mahood (2017), Human-started wildfires expand the fire niche across the united states, *Proceedings*

of the National Academy of Sciences of the United States of America, *114*(11), 2946–2951, doi:10.1073/pnas.1617394114.

Bales, R. C., N. P. Molotch, T. H. Painter, M. D. Dettinger, R. Rice, and J. Dozier (2006), Mountain hydrology of the western united states, *Water Resources Research*, *42*(8), W08,432, doi:10.1029/2005WR004387.

Bales, R. C., J. J. Battles, Y. Chen, M. H. Conklin, E. Holst, K. L. O'Hara, P. Saksa, and W. Stewart (2011), Forests and water in the sierra nevada: Sierra nevada watershed ecosystem enhancement project, report number 11.1.

Barbeta, A., and J. Peñuelas (2016), Sequence of plant responses to droughts of different timescales: lessons from holm oak (quercus ilex) forests, *Plant Ecology and Diversity*, *9*, 321–338, doi:10.1080/17550874.2016.1212288.

Barnes, E., B. Toms, J. Hurrell, I. Ebert-Uphoff, C. Anderson, and D. Anderson (2020), Indicator patterns of forced change learned by an artificial neural network, *Journal of Advances in Modeling Earth Systems*, *12*(9), e2020MS002,195.

Barnes, E. A., J. W. Hurrell, I. Ebert-Uphoff, C. Anderson, and D. Anderson (2019), Viewing forced climate patterns through an ai lens, *Geophysical Research Letters*, *46*, 13,389–13,398, doi:10.1029/2019GL084944.

Bass, B., J. Norris, C. Thackeray, and A. Hall (2022), Natural variability has concealed increases in western us flood hazard since the 1970s, *Geophysical Research Letters*, *49*(7), e2021GL096,529, doi:10.1029/2021GL096529.

Bayr, T., D. Dommenget, T. Martin, and S. Power (2014), The eastward shift of the walker circulation in response to global warming and its relationship to enso variability, *Climate Dynamics*, *43*, 2747–2763.

Beck, H. E., E. F. Wood, M. Pan, C. K. Fisher, D. G. Miralles, A. I. van Dijk, and R. F. Adler (2018), Mswep v2 global 3-hourly 0.1° precipitation: Methodology and quantitative

assessment, *Bulletin of the American Meteorological Society*, *100*, 473–500, doi:10.1175/BAMS-D-17-0138.1.

Bindoff, N. L., et al. (2013), *Detection and attribution of climate change: From global to regional*, pp. 867–952, Cambridge University Press, Cambridge, UK and New York.

Bond-Lamberty, B., A. V. Rocha, K. Calvin, B. Holmes, C. Wang, and M. L. Goulden (2014), Disturbance legacies and climate jointly drive tree growth and mortality in an intensively studied boreal forest, *Global Change Biology*, *20*, 216–227, doi:10.1111/gcb.12404.

Bony, S., G. Bellon, D. Klocke, S. Sherwood, S. Fermepin, and S. Denvil (2013), Robust direct effect of carbon dioxide on tropical circulation and regional precipitation, *Nature Geoscience*, *6*(6), 447–451.

Borodina, A., E. M. Fischer, and R. Knutti (2017), Models are likely to underestimate increase in heavy rainfall in the extratropical regions with high rainfall intensity, *Geophysical Research Letters*, *44*, 7401–7409, doi:10.1002/2017GL074530.

Bowman, D. M. J. S., G. J. Williamson, J. T. Abatzoglou, C. A. Kolden, M. A. Cochrane, and A. M. S. Smith (2017), Human exposure and sensitivity to globally extreme wildfire events, *Nature Ecology Evolution*, *1*(3), 0058, doi:10.1038/s41559-016-0058.

Bowman, D. M. J. S., C. A. Kolden, J. T. Abatzoglou, F. H. Johnston, G. R. van der Werf, and M. Flannigan (2020), Vegetation fires in the anthropocene, *Nature Reviews Earth Environment*, *1*(10), 500–515, doi:10.1038/s43017-020-0085-3.

Breiman, L. (2001), Random forests, *Machine Learning*, *45*, 5–32, doi:10.1023/A:1010933404324.

Brodrick, P. G., and G. P. Asner (2017), Remotely sensed predictors of conifer tree mortality during severe drought, *Environmental Research Letters*, *12*, 115,013, doi:10.1088/1748-9326/aa8eef.

Brodrick, P. G., L. D. L. Anderegg, and G. P. Asner (2019), Forest drought resistance at large geographic scales, *Geophysical Research Letters*, *46*(7), 3603–3613, doi:10.1029/2018GL081108.

Brown, P. T., H. Hanley, A. Mahesh, C. Reed, S. J. Strenfel, S. J. Davis, A. K. Kochanski, and C. B. Clements (2023), Climate warming increases extreme daily wildfire growth risk in california, *Nature*, *621*(7980), 760–766, doi:10.1038/s41586-023-06444-3.

Byer, S., and Y. Jin (2017), Detecting drought-induced tree mortality in sierra nevada forests with time series of satellite data, *Remote Sensing*, *9*, 929, doi:10.3390/rs9090929.

Byrne, S. M., M. A. Merrifield, M. L. Carter, D. R. Cayan, R. E. Flick, A. Gershunov, and S. N. Giddings (2023), Southern california winter precipitation variability reflected in 100-year ocean salinity record, *Communications Earth Environment*, *4*(1), 58, doi:10.1038/s43247-023-00803-8.

Böhle, M., F. Eitel, M. Weygandt, and K. Ritter (2019), Layer-wise relevance propagation for explaining deep neural network decisions in mri-based alzheimer's disease classification, *Frontiers in Aging Neuroscience*, *11*, 194, doi:10.3389/fnagi.2019.00194.

Cai, W., A. Santoso, G. Wang, S. Yeh, S. An, K. Cobb, M. Collins, E. Guilyardi, F. Jin, J. Kug, and M. Lengaigne (2015), Enso and greenhouse warming, *Nature Climate Change*, *5*(9), 849–859.

Chadwick, R., I. Boutle, and G. Martin (2013), Spatial patterns of precipitation change in cmip5: Why the rich do not get richer in the tropics, *Journal of Climate*, *26*(11), 3803–3822.

Chemke, R. (2022), Large hemispheric differences in the hadley cell strength variability due to ocean coupling, *npj Climate and Atmospheric Science*, *5*(1), 1.

Chemke, R., and L. Polvani (2019), Opposite tropical circulation trends in climate models and in reanalyses, *Nature Geoscience*, *12*(7), 528–532.

Chemke, R., and J. Yuval (2023), Human-induced weakening of the northern hemisphere tropical circulation, *Nature*, *617*(7961), 529–532.

Chen, B., and Y. Jin (2022), Spatial patterns and drivers for wildfire ignitions in california, *Environmental Research Letters*, *17*(5), 054,025, doi:10.1088/1748-9326/ac60da.

Chou, C., and C. Chen (2010), Depth of convection and the weakening of tropical circulation in global warming, *Journal of Climate*, *23*(11), 3019–3030.

Chou, C., J. Neelin, C. Chen, and J. Tu (2009), Evaluating the "rich-get-richer" mechanism in tropical precipitation change under global warming, *Journal of Climate*, *22*(8), 1982–2005.

Chou, C., T. Wu, and P. Tan (2013), Changes in gross moist stability in the tropics under global warming, *Climate Dynamics*, *41*, 2481–2496.

Cobb, R. C., et al. (2017), Ecosystem dynamics and management after forest die-off: a global synthesis with conceptual state-and-transition models, *Ecosphere*, *8*, e02,034, doi: 10.1002/ecs2.2034.

Commission, E. (2012), Report on the review of the european water scarcity and drought policy.

Contractor, S., M. G. Donat, L. V. Alexander, M. Ziese, A. Meyer-Christoffer, U. Schneider, E. Rustemeier, A. Becker, I. Durre, and R. S. Vose (2020), Rainfall estimates on a gridded network (regen)—a global land-based gridded dataset of daily precipitation from 1950–2013, *Hydrology and Earth System Sciences*, *24*(2), 919–943, doi: 10.5194/hess-24-919-2020.

Corvec, S., and C. Fletcher (2017), Changes to the tropical circulation in the mid-pliocene and their implications for future climate, *Climate of the Past*, *13*(2), 135–147.

Costello, M., M. Vale, W. Kiessling, S. Maharaj, J. Price, and G. Talukdar (2022), *Cross-chapter paper 1: Biodiversity hotspots*, pp. 2123–2161.

Countryman, C. M., and W. A. Dean (1979), Measuring moisture content in living chaparral: A field user's manual, *General technical report psw-36*, USDA Forest Service.

Cox, P., C. Huntingford, and M. Williamson (2018), Emergent constraint on equilibrium climate sensitivity from global temperature variability, *Nature*, *553*(7688), 319–322.

Crimmins, A., J. Balbus, J. Gamble, C. Beard, J. Bell, D. Dodgen, R. Eisen, N. Fann, M. Hawkins, S. Herring, L. Jantarasami, D. Mills, S. Saha, M. Sarofim, J. Trtanj, and L. Ziska (2016), *The impacts of climate change on human health in the United States: A Scientific Assessment*, US Global Change Research Program, Washington, DC, doi: 10.7930/J0R49NQX.

Dai, A. (2011), Drought under global warming: a review, *Wiley Interdisciplinary Reviews: Climate Change*, *2*, 45–65, doi:10.1002/wcc.81.

Dai, A. (2013), Increasing drought under global warming in observations and models, *Nature Climate Change*, *3*, 52–58, doi:10.1038/nclimate1633.

Dennison, P. E., D. A. Roberts, S. H. Peterson, and J. Rechel (2005), Use of normalized difference water index for monitoring live fuel moisture, *International Journal of Remote Sensing*, *26*(5), 1035–1042, doi:10.1080/0143116042000273998.

Dennison, P. E., S. C. Brewer, J. D. Arnold, and M. A. Moritz (2014), Large wildfire trends in the western united states, 1984–2011, *Geophysical Research Letters*, *41*(8), 2928–2933, doi:10.1002/2014GL059576.

Deser, C., F. Lehner, K. B. Rodgers, T. Ault, T. L. Delworth, P. N. DiNezio, A. Fiore, C. Frankignoul, J. C. Fyfe, D. E. Horton, J. E. Kay, R. Knutti, N. S. Lovenduski, J. Marotzke, K. A. McKinnon, S. Minobe, J. Randerson, J. A. Screen, I. R. Simpson, and

M. Ting (2020), Insights from earth system model initial-condition large ensembles and future prospects, *Nature Climate Change*, *10*(4), 277–286, doi:10.1038/s41558-020-0731-2.

Dettinger, M. D., F. M. Ralph, T. Das, P. J. Neiman, and D. R. Cayan (2011), Atmospheric rivers, floods and the water resources of california, *Water*, *3*(2), 445–478, doi:10.3390/w3020445.

Dobrescu, A., M. V. Giuffrida, and S. A. Tsaftaris (2019), Understanding deep neural networks for regression in leaf counting, in *Proceedings of the IEEE Conference on Computer Vision and Pattern Recognition Workshops*, pp. 2600–2608, IEEE, Long Beach, CA, USA.

Doerr, S. H., and C. Santín (2016), Global trends in wildfire and its impacts: Perceptions versus realities in a changing world, *Philosophical Transactions of the Royal Society B: Biological Sciences*, *371*(1696), 20150,345, doi:10.1098/rstb.2015.0345.

Donat, M. G., A. L. Lowry, L. V. Alexander, P. A. O'Gorman, and N. Maher (2016), More extreme precipitation in the world's dry and wet regions, *Nature Climate Change*, *6*, 508–513.

Donat, M. G., O. Angélil, and A. M. Ukkola (2019), Intensification of precipitation extremes in the world's humid and water-limited regions, *Environmental Research Letters*, *14*(6), 065,003, doi:10.1088/1748-9326/ab1c8e.

Dong, L., L. Leung, F. Song, and J. Lu (2021), Uncertainty in el niño-like warming and california precipitation changes linked by the interdecadal pacific oscillation, *Nature Communications*, *12*(1), 6484.

Duffy, M., and P. O'Gorman (2023), Intermodel spread in walker circulation responses linked to spread in moist stability and radiation responses, *Journal of Geophysical Research: Atmospheres*, *128*(1), e2022JD037,382.

Dunn, R. J., L. V. Alexander, M. G. Donat, X. Zhang, M. Bador, N. Herold, et al. (2020), Development of an updated global land in situ-based data set of temperature and precipitation extremes: Hadex3, *Journal of Geophysical Research: Atmospheres*, *125*(16), e2019JD032,263.

Easterling, D. R., K. E. Kunkel, M. F. Wehner, and L. Sun (2016), Detection and attribution of climate extremes in the observed record, *Weather and Climate Extremes*, *11*, 17–27.

Ebert-Uphoff, I., S. Samarasinghe, and E. Barnes (2019), Thoughtfully using artificial intelligence in earth science, *Eos*, *100*, doi:10.1029/2019EO135235.

Elvidge, C. D., K. E. Baugh, J. B. Dietz, T. Bland, P. C. Sutton, and H. W. Kroehl (1999), Radiance calibration of dmsp-ols low-light imaging data of human settlements, *Remote Sensing of Environment*, *68*(1), 77–88, doi:10.1016/S0034-4257(98)00098-4.

Eyring, V., S. Bony, G. A. Meehl, C. Senior, B. Stevens, R. J. Stouffer, and K. E. Taylor (2015), Overview of the coupled model intercomparison project phase 6 (cmip6) experimental design and organisation, *Geoscientific Model Development Discussion*, *8*(12), 10,539–10,583, doi:10.5194/gmdd-8-10539-2015.

Eyring, V., S. Bony, G. Meehl, C. Senior, B. Stevens, R. Stouffer, and K. Taylor (2016), Overview of the coupled model intercomparison project phase 6 (cmip6) experimental design and organization, *Geoscientific Model Development*, *9*(5), 1937–1958.

Faivre, N., Y. Jin, M. L. Goulden, and J. T. Randerson (2014), Controls on the spatial pattern of wildfire ignitions in southern california, *International Journal of Wildland Fire*, *23*(6), 799–811, doi:10.1071/WF13136.

Fan, C., and D. Dommenget (2024), The weakening of the tropical circulation is caused by the lifting of the tropopause height, *Climate Dynamics*, *62*(1), 187–201.

Fellows, A. W., and M. L. Goulden (2017), Mapping and understanding dry season soil water drawdown by california montane vegetation, *Ecohydrology*, *10*, e1772, doi:10.1002/eco.1772.

Fettig, C. J., L. A. Mortenson, B. M. Bulaon, and P. B. Foulk (2019), Tree mortality following drought in the central and southern sierra nevada, california, u.s., *Forest Ecology and Management*, *432*, 164–178, doi:10.1016/j.foreco.2018.09.006.

Fischer, E., U. Beyerle, and R. Knutti (2013), Robust spatially aggregated projections of climate extremes, *Nature Climate Change*, *3*(12), 1033–1038.

Flint, L. E., and A. L. Flint (2012), Downscaling future climate scenarios to fine scales for hydrologic and ecological modeling and analysis, *Ecological Processes*, *1*, 1–15, doi:10.1186/2192-1709-1-2.

Flint, L. E., A. L. Flint, J. H. Thorne, and R. Boynton (2013), Fine-scale hydrologic modeling for regional landscape applications: The california basin characterization model development and performance, *Ecological Processes*, *2*, 1–21, doi:10.1186/2192-1709-2-25.

Forkel, M., W. Dorigo, G. Lasslop, E. Chuvieco, S. Hantson, A. Heil, I. Teubner, K. Thonicke, and S. P. Harrison (2019), Recent global and regional trends in burned area and their compensating environmental controls, *Environmental Research Communications*, *1*(5), 051,005, doi:10.1088/2515-7620/ab25d2.

Gastineau, G., L. Li, and H. Le Treut (2009), The hadley and walker circulation changes in global warming conditions described by idealized atmospheric simulations, *Journal of Climate*, *22*(14), 3993–4013.

Gelaro, R., W. McCarty, M. Suárez, R. Todling, A. Molod, L. Takacs, C. Randles, A. Darmenov, M. Bosilovich, R. Reichle, and K. Wargan (2017), The modern-era retrospective analysis for research and applications, version 2 (merra-2), *Journal of Climate*, *30*(14), 5419–5454.

Gergel, D. R., B. Nijssen, J. T. Abatzoglou, D. P. Lettenmaier, and M. R. Stumbaugh (2017), Effects of climate change on snowpack and fire potential in the western usa, *Climatic Change*, *141*(2), 287–299, doi:10.1007/s10584-017-1899-y.

Gershunov, A., T. Shulgina, R. E. S. Clemesha, K. Guirguis, D. W. Pierce, M. D. Dettinger, D. A. Lavers, D. R. Cayan, S. D. Polade, J. Kalansky, and F. M. Ralph (2019), Precipitation regime change in western north america: The role of atmospheric rivers, *Scientific Reports*, *9*(1), 9944, doi:10.1038/s41598-019-46169-w.

Gillett, N., F. Zwiers, A. Weaver, and P. Stott (2003), Detection of human influence on sea-level pressure, *Nature*, *422*(6929), 292–294.

Goulden, M. L., and R. C. Bales (2014), Mountain runoff vulnerability to increased evapotranspiration with vegetation expansion, *Proceedings of the National Academy of Sciences of the United States of America*, *111*(39), 14,071–14,075, doi:10.1073/pnas.1319316111.

Goulden, M. L., and R. C. Bales (2019), California forest die-off linked to multi-year deep soil drying in 2012–2015 drought, *Nature Geoscience*, *12*(8), 632–637, doi:10.1038/s41561-019-0388-5.

Grigorescu, I., L. Cordero-Grande, A. D. Edwards, J. V. Hajnal, M. Modat, and M. Deprez (2019), Investigating image registration impact on preterm birth classification: An interpretable deep learning approach, in *Smart Ultrasound Imaging and Perinatal, Preterm and Paediatric Image Analysis*, pp. 104–112, Springer, Cham.

Guswa, A. J. (2008), The influence of climate on root depth: A carbon cost-benefit analysis, *Water Resources Research*, *44*, 1–11, doi:10.1029/2007WR006384.

Hall, A., and X. Qu (2006), Using the current seasonal cycle to constrain snow albedo feedback in future climate change, *Geophysical Research Letters*, *33*(3).

Hall, A., P. Cox, C. Huntingford, and S. Klein (2019), Progressing emergent constraints on future climate change, *Nature Climate Change*, *9*(4), 269–278.

Hamed, K. H., and A. R. Rao (1998), A modified mann-kendall trend test for autocorrelated data, *Journal of Hydrology*, *204*, 182–196.

Handmer, J., et al. (2012), *Changes in impacts of climate extremes: Human systems and ecosystems*, pp. 231–290, Cambridge University Press, Cambridge, UK and New York.

Hanes, C. C., X. Wang, P. Jain, M. A. Parisien, J. M. Little, and M. D. Flannigan (2019), Fire-regime changes in canada over the last half century, *Canadian Journal of Forest Research*, *49*(3), 256–269, doi:10.1139/cjfr-2018-0293.

Hawkins, E., D. Frame, L. Harrington, M. Joshi, A. King, M. Rojas, and R. Sutton (2020), Observed emergence of the climate change signal: from the familiar to the unknown, *Geophysical Research Letters*, *47*(6), e2019GL086,259.

He, J., and B. Soden (2016), The impact of sst biases on projections of anthropogenic climate change: A greater role for atmosphere-only models?, *Geophysical Research Letters*, *43*(14), 7745–7750.

Hegerl, G., and F. Zwiers (2011), Use of models in detection and attribution of climate change, *Wiley Interdisciplinary Reviews: Climate Change*, *2*(4), 570–591.

Heinimann, H. R. (2010), A concept in adaptive ecosystem management-an engineering perspective, *Forest Ecology and Management*, *259*, 848–856, doi:10.1016/j.foreco.2009.11.006.

Held, I. M., and B. J. Soden (2006), Robust responses of the hydrological cycle to global warming, *Journal of Climate*, *19*(21), 5686–5699.

Herold, N., A. Behrangi, and L. V. Alexander (2017), Large uncertainties in observed daily precipitation extremes over land, *Journal of Geophysical Research: Atmospheres*, *22*, 668–681, doi:10.1002/2016JD025842.

Hersbach, H., et al. (2020), The era5 global reanalysis, *Quarterly Journal of the Royal Meteorological Society*, *146*(730), 1999–2049, doi:10.1002/qj.3803.

Holden, Z. A., A. Swanson, C. H. Luce, W. M. Jolly, M. Maneta, J. W. Oyler, D. A. Warren, R. Parsons, and D. Affleck (2018), Decreasing fire season precipitation increased recent western us forest wildfire activity, *Proceedings of the National Academy of Sciences of the United States of America*, *115*(36), E8349–E8357, doi:10.1073/pnas.1802316115.

Holsinger, L., S. A. Parks, M. Parisien, C. Miller, E. Batllori, and M. A. Moritz (2019), Climate change likely to reshape vegetation in north america's largest protected areas, *Conservation Science and Practice*, *1*, 1–17, doi:10.1111/csp2.14.

Hwang, Y., and D. Frierson (2013), Link between the double-intertropical convergence zone problem and cloud biases over the southern ocean, *Proceedings of the National Academy of Sciences*, *110*(13), 4935–4940.

Intergovernmental Panel on Climate Change (2022), *Climate Change 2022 – The Physical Science Basis*, 1055–1210 pp., Cambridge University Press, doi:10.1017/9781009157896.010, water Cycle Changes.

Jin, Y., M. L. Goulden, N. Faivre, S. Veraverbeke, F. Sun, A. Hall, M. S. Hand, S. Hook, and J. T. Randerson (2015), Identification of two distinct fire regimes in southern california: Implications for economic impact and future change, *Environmental Research Letters*, *10*(9), 094,005, doi:10.1088/1748-9326/10/9/094005.

Jolly, W. M., M. A. Cochrane, P. H. Freeborn, Z. A. Holden, T. J. Brown, G. J. Williamson, and D. M. J. S. Bowman (2015), Climate-induced variations in global wildfire danger from 1979 to 2013, *Nature Communications*, *6*, 7537, doi:10.1038/ncomms8537.

Kanamitsu, M., W. Ebisuzaki, J. Woollen, S.-K. Yang, J. Hnilo, M. Fiorino, and G. L. Potter (2002), Ncep-doe amip-ii reanalysis (r-2), *Bulletin of the American Meteorological Society*, *83*, 1631–1643.

Kane, V. R., J. A. Lutz, C. Alina Cansler, N. A. Povak, D. J. Churchill, D. F. Smith, J. T. Kane, and M. P. North (2015), Water balance and topography predict fire and forest structure patterns, *Forest Ecology and Management*, *338*, 1–13, doi:10.1016/j.foreco.2014.11.009.

Keeley, J. E., and A. D. Syphard (2018), Historical patterns of wildfire ignition sources in california ecosystems, *International Journal of Wildland Fire*, *27*(12), 781–799, doi:10.1071/WF18026.

Keeley, J. E., and A. D. Syphard (2019), Twenty-first century california, usa, wildfires: Fuel-dominated vs. wind-dominated fires, *Fire Ecology*, *15*(1), 24, doi:10.1186/s42408-019-0041-0.

Keeley, J. E., J. Guzman-Morales, A. Gershunov, A. D. Syphard, D. Cayan, D. W. Pierce, M. Flannigan, and T. J. Brown (2021), Ignitions explain more than temperature or precipitation in driving santa ana wind fires, *Science Advances*, *7*(30), eabd5058, doi:10.1126/sciadv.abd5058.

Keenan, R. J. (2015), Climate change impacts and adaptation in forest management: a review, *Annals of Forest Science*, *72*, 145–167, doi:10.1007/s13595-014-0446-5.

Kelly, A. E., and M. L. Goulden (2008), Rapid shifts in plant distribution with recent climate change, *Proceedings of the National Academy of Sciences of the United States of America*, *105*, 11,823–26, doi:10.1073/pnas.0802891105.

Kharin, V., F. Zwiers, X. Zhang, and M. Wehner (2013), Changes in temperature and precipitation extremes in the cmip5 ensemble, *Climatic Change*, *119*(2), 345–357, doi:10.1007/s10584-013-0705-8.

Khorshidi, M. S., P. E. Dennison, M. R. Nikoo, A. Aghakouchak, C. H. Luce, and M. Sadegh (2020), Increasing concurrence of wildfire drivers tripled megafire critical danger days

in southern california between 1982 and 2018, *Environmental Research Letters*, *15*(10), 1040b5, doi:10.1088/1748-9326/abae9e.

Kim, H. (2017), Global soil wetness project phase 3 atmospheric boundary conditions (experiment 1), Data Integration and Analysis System (DIAS), doi:10.20783/DIAS.501.

King, A. D., M. G. Donat, E. M. Fischer, E. Hawkins, L. V. Alexander, D. J. Karoly, et al. (2015), The timing of anthropogenic emergence in simulated climate extremes, *Environmental Research Letters*, *10*(9), 094,015, doi:10.1088/1748-9326/10/9/094015.

Kirchmeier-Young, M. C., and X. Zhang (2020), Human influence has intensified extreme precipitation in north america, *Proceedings of the National Academy of Sciences of the United States of America*, *117*(24), 13,308–13,313, doi:10.1073/PNAS.1921628117.

Kleidon, A., and M. Heimann (1998), A method of determining rooting depth from a terrestrial biosphere model and its impacts on the global water and carbon cycle, *Global Change Biology*, *4*(3), 275–286, doi:10.1046/j.1365-2486.1998.00152.x.

Klos, P. Z., et al. (2018), Subsurface plant-accessible water in mountain ecosystems with a mediterranean climate, *WIREs Water*, *5*, 1277, doi:10.1002/wat2.1277.

Kobayashi, S., et al. (2015), The jra-55 reanalysis: General specifications and basic characteristics, *Journal of the Meteorological Society of Japan*, *93*(1), 5–48, doi:10.2151/jmsj.2015-001.

Koontz, M. J., M. P. North, C. M. Werner, S. E. Fick, and A. M. Latimer (2020), Local forest structure variability increases resilience to wildfire in dry western u.s. coniferous forests, *Ecology Letters*, *23*(3), 483–494, doi:10.1111/ele.13447.

Krawchuk, M. A., and M. A. Moritz (2014), Burning issues: Statistical analyses of global fire data to inform assessments of environmental change, *Environmetrics*, *25*(6), 472–481, doi:10.1002/env.2287.

Kretschmer, M., D. Coumou, J. F. Donges, and J. Runge (2016), Using causal effect networks to analyze different arctic drivers of midlatitude winter circulation, *Journal of Climate*, *29*(11), 4069–4081, doi:10.1175/JCLI-D-15-0654.1.

Kwiatkowski, L., L. Bopp, O. Aumont, P. Ciais, P. Cox, C. Laufkötter, Y. Li, and R. Séférian (2017), Emergent constraints on projections of declining primary production in the tropical oceans, *Nature Climate Change*, *7*(5), 355–358.

Langenbrunner, B., and J. D. Neelin (2017), Pareto-optimal estimates of california precipitation change, *Geophysical Research Letters*, *44*(24), 12,436–12,446, doi:10.1002/2017GL075226.

Lapuschkin, S. (2019), Opening the machine learning black box with layer-wise relevance propagation, Ph.D. thesis, Technische Universität Berlin.

Li, X., and Y. Zhou (2017), Urban mapping using dmsp/ols stable night-time light: A review, *International Journal of Remote Sensing*, *38*(21), 6030–6046, doi:10.1080/01431161.2016.1274451.

Li, X., Y. Zhou, M. Zhao, and X. Zhao (2020), A harmonized global nighttime light dataset 1992–2018, *Scientific Data*, *7*(1), 168, doi:10.1038/s41597-020-0510-y.

Lu, J., G. A. Vecchi, and T. Reichler (2007), Expansion of the hadley cell under global warming, *Geophysical Research Letters*, *34*, L06,805, doi:10.1029/2006GL028443.

L'Heureux, M., S. Lee, and B. Lyon (2013), Recent multidecadal strengthening of the walker circulation across the tropical pacific, *Nature Climate Change*, *3*(6), 571–576.

Ma, J., S. Xie, and Y. Kosaka (2012), Mechanisms for tropical tropospheric circulation change in response to global warming, *Journal of Climate*, *25*(8), 2979–2994.

Ma, J., R. Chadwick, K. Seo, C. Dong, G. Huang, G. Foltz, and J. Jiang (2018), Responses of

the tropical atmospheric circulation to climate change and connection to the hydrological cycle, *Annual Review of Earth and Planetary Sciences*, *46*, 549–580.

Ma, J., L. Zhou, G. Foltz, X. Qu, J. Ying, H. Tokinaga, C. Mechoso, J. Li, and X. Gu (2020), Hydrological cycle changes under global warming and their effects on multiscale climate variability, *Annals of the New York Academy of Sciences*, *1472*(1), 21–48.

Madakumbura, G., C. Thackeray, J. Norris, N. Goldenson, and A. Hall (2021), Anthropogenic influence on extreme precipitation over global land areas seen in multiple observational datasets, *Nature Communications*, *12*(1), 3944.

Madakumbura, G. D., H. Kim, N. Utsumi, H. Shiogama, E. M. Fischer, Seland, J. F. Scinocca, D. M. Mitchell, Y. Hirabayashi, and T. Oki (2019), Event-to-event intensification of the hydrologic cycle from 1.5 c to a 2 c warmer world, *Scientific Reports*, *9*(1), 3483.

Madakumbura, G. D., M. L. Goulden, A. Hall, R. Fu, M. A. Moritz, C. D. Koven, L. M. Kueppers, C. A. Norlen, and J. T. Randerson (2020), Recent california tree mortality portends future increase in drought-driven forest die-off, *Environmental Research Letters*, *15*(9), 094,016, doi:10.1088/1748-9326/abc719.

Madakumbura, G. D., J. Norris, C. Thackeray, S. Po-Chedley, F. Ahmed, and A. Hall (2024a), Emergent constraint on future changes in the tropical atmospheric circulation, doi:10.21203/rs.3.rs-3908042/v1, in review at Nature Climate Change.

Madakumbura, G. D., M. A. Moritz, K. McKinnon, A. P. Williams, B. Rahimi, S. Bass, J. Norris, R. Fu, and A. Hall (2024b), Climate change drives earlier wildfire season onset in california, doi:10.21203/rs.3.rs-3908042/v1, in review at Nature Geoscience.

Maeda, E. E., H. Kim, L. E. O. C. Aragão, J. S. Famiglietti, and T. Oki (2015), Disruption of hydroecological equilibrium in southwest amazon mediated by drought, *Geophysical Research Letters*, *42*, 7546–7553, doi:10.1002/2015GL065252.

Maher, P., G. Vallis, S. Sherwood, M. Webb, and P. Sansom (2018), The impact of parameterized convection on climatological precipitation in atmospheric global climate models, *Geophysical Research Letters*, *45*(8), 3728–3736.

Marvel, K., B. I. Cook, C. J. Bonfils, P. J. Durack, J. E. Smerdon, and A. P. Williams (2019), Twentieth-century hydroclimate changes consistent with human influence, *Nature*, *569*(7754), 59–65.

McDowell, N. G., et al. (2008), Mechanisms of plant survival and mortality during drought: why do some plants survive while others succumb to drought?, *New Phytologist*, *178*, 719–739, doi:10.1111/j.1469-8137.2008.02436.x.

McDowell, N. G., et al. (2019), Mechanisms of a coniferous woodland persistence under drought and heat, *Environmental Research Letters*, *14*, doi:10.1088/1748-9326/ab0921.

McKinnon, K. A., and C. Deser (2021), The inherent uncertainty of precipitation variability, trends, and extremes due to internal variability, with implications for western u.s. water resources, *Journal of Climate*, *34*(24), 9605–9622, doi:10.1175/JCLI-D-21-0251.1.

McLaughlin, B. C., D. D. Ackerly, P. Z. Klos, J. Natali, T. E. Dawson, and S. E. Thompson (2017), Hydrologic refugia, plants, and climate change, *Global Change Biology*, *23*, 2942–2961, doi:10.1111/gcb.13629.

Meinshausen, M., et al. (2011), The rcp greenhouse gas concentrations and their extensions from 1765 to 2300, *Climatic Change*, *109*(1-2), 213–241, doi:10.1007/s10584-011-0156-z.

Merlis, T. (2015), Direct weakening of tropical circulations from masked co2 radiative forcing, *Proceedings of the National Academy of Sciences*, *112*(43), 13,167–13,171.

Millar, C. I., and N. L. Stephenson (2015), Temperate forest health in an era of emerging megadisturbance, *Science*, *349*(6250), 823–826, doi:10.1126/science.aaa9933.

Min, S. K., X. B. Zhang, F. W. Zwiers, and G. C. Hegerl (2011), Human contribution to more-intense precipitation extremes, *Nature*, *470*, 378–381, doi:10.1038/nature09763.

Minnich, R. A. (2018), *California fire climate*, 11–25 pp., University of California Press.

Mishra, A. K., and V. P. Singh (2010), A review of drought concepts, *Journal of Hydrology*, *391*, 202–216, doi:10.1016/j.jhydrol.2010.07.012.

Mitas, C., and A. Clement (2005), Has the hadley cell been strengthening in recent decades?, *Geophysical Research Letters*, *32*(3).

Montavon, G., W. Samek, and K. R. Müller (2018), Methods for interpreting and understanding deep neural networks, *Digital Signal Processing*, *73*, 1–15.

Montavon, G., A. Binder, S. Lapuschkin, W. Samek, and K. R. Müller (2019), *Layer-wise relevance propagation: an overview*, pp. 193–209, Springer, Cham, doi:10.1007/978-3-030-28954-6_10.

Mora, C., A. G. Frazier, R. J. Longman, R. S. Dacks, M. M. Walton, E. J. Tong, J. J. Sanchez, L. R. Kaiser, Y. O. Stender, J. M. Anderson, C. M. Ambrosino, I. Fernandez-Silva, L. M. Giuseffi, and T. W. Giambelluca (2013), The projected timing of climate departure from recent variability, *Nature*, *502*(7470), 183–187, doi:10.1038/nature12540.

Morelli, T. L., et al. (2016), Managing climate change refugia for climate adaptation, *PLoS One*, *11*, e0159,909, doi:10.1371/journal.pone.0159909.

Moritz, M. A., M. A. Parisien, E. Batllori, M. A. Krawchuk, J. Van Dorn, D. J. Ganz, and K. Hayhoe (2012), Climate change and disruptions to global fire activity, *Ecosphere*, *3*(6), art49, doi:10.1890/ES11-00345.1.

Myers, N., R. Mittermeier, C. Mittermeier, G. Da Fonseca, and J. Kent (2000), Biodiversity hotspots for conservation priorities, *Nature*, *403*(6772), 853–858.

National Interagency Coordination Center, N. (2021), Outlooks, verified 7 March 2024.

Nelson, J. (2000), Prediction of diurnal change in 10-h fuel stick moisture content, *Canadian Journal of Forest Research*, *30*(7), 1071–1087, doi:10.1139/x00-032.

Norris, J., G. Chen, and J. D. Neelin (2019), Thermodynamic versus dynamic controls on extreme precipitation in a warming climate from the community earth system model large ensemble, *Journal of Climate*, *32*(4), 1025–1045.

Norris, J., A. Hall, D. Chen, C. W. Thackeray, and G. D. Madakumbura (2021), Assessing the representation of synoptic variability associated with california extreme precipitation in cmip6 models, *Journal of Geophysical Research: Atmospheres*, *126*(6), e2020JD033,497, doi:10.1029/2020JD033938.

Norris, J., A. Hall, C. Thackeray, D. Chen, and G. Madakumbura (2022a), Evaluating hydrologic sensitivity in cmip6 models: Anthropogenic forcing versus enso, *Journal of Climate*, *35*(21), 6955–6968.

Norris, J., D. Chen, A. Hall, and C. Thackeray (2022b), Moisture-budget drivers of global projections of meteorological drought from multiple gcm large ensembles, *Journal of Geophysical Research: Atmospheres*, *127*(24), e2022JD037,745.

O'Gorman, P., and T. Schneider (2009), The physical basis for increases in precipitation extremes in simulations of 21st-century climate change, *Proceedings of the National Academy of Sciences of the United States of America*, *106*(35), 14,773–14,777, doi:10.1073/pnas.0907610106.

Omernik, J. M., and G. E. Griffith (2014), Ecoregions of the conterminous united states: Evolution of a hierarchical spatial framework, *Environmental Management*, *54*(6), 1249–1266, doi:10.1007/s00267-014-0364-1.

O'Neill, B. C., C. Tebaldi, D. P. Van Vuuren, V. Eyring, P. Friedlingstein, G. Hurtt, R. Knutti, E. Kriegler, J. F. Lamarque, J. Lowe, G. A. Meehl, R. Moss, K. Riahi, and

B. M. Sanderson (2016), The scenario model intercomparison project (scenariomip) for cmip6, *Geoscientific Model Development*, *9*(9), 3461–3482, doi:10.5194/gmd-9-3461-2016.

O'Gorman, P. (2012), Sensitivity of tropical precipitation extremes to climate change, *Nature Geoscience*, *5*(10), 697–700.

O'Gorman, P. A., and C. J. Muller (2010), How closely do changes in surface and column water vapor follow clausius–clapeyron scaling in climate change simulations?, *Environmental Research Letters*, *5*(2), 025,207.

Paik, S., S. K. Min, X. Zhang, M. G. Donat, A. D. King, and Q. Sun (2020), Determining the anthropogenic greenhouse gas contribution to the observed intensification of extreme precipitation, *Geophysical Research Letters*, *47*(12), e2019GL086,875.

Parks, S. A., L. M. Holsinger, C. Miller, and M. A. Parisien (2018), Analog-based fire regime and vegetation shifts in mountainous regions of the western us, *Ecography*, *41*, 910–21, doi:10.1111/ecog.03432.

Paz-Kagan, T., P. G. Brodrick, N. R. Vaughn, A. J. Das, N. L. Stephenson, K. R. Nydick, and G. P. Asner (2017), What mediates tree mortality during drought in the southern sierra nevada, *Ecological Applications*, *27*, 2443–57, doi:10.1002/eap.1602.

Pfahl, S., P. A. O'Gorman, and E. M. Fischer (2017), Understanding the regional pattern of projected future changes in extreme precipitation, *Nature Climate Change*, *7*(6), 423–427, doi:10.1038/nclimate3287.

Po-Chedley, S., J. Fasullo, N. Siler, Z. Labe, E. Barnes, C. Bonfils, and B. Santer (2022), Internal variability and forcing influence model–satellite differences in the rate of tropical tropospheric warming, *Proceedings of the National Academy of Sciences*, *119*(47), e2209431,119.

Rao, K., A. P. Williams, N. S. Diffenbaugh, M. Yebra, C. Bryant, and A. G. Konings (2023), Dry live fuels increase the likelihood of lightning-caused fires, *Geophysical Research Letters*, *50*(15), e2023GL100,478, doi:10.1029/2022GL100975.

Ribes, A., F. W. Zwiers, J.-M. Azais, and P. Naveau (2017), A new statistical approach to climate change detection and attribution, *Climate Dynamics*, *48*(1-2), 367–386.

Roberts, D. A., P. E. Dennison, S. Peterson, S. Sweeney, and J. Rechel (2006), Evaluation of airborne visible/infrared imaging spectrometer (aviris) and moderate resolution imaging spectrometer (modis) measures of live fuel moisture and fuel condition in a shrubland ecosystem in southern california, *Journal of Geophysical Research: Biogeosciences*, *111*(G4), G04S02, doi:10.1029/2005JG000113.

Roca, R., L. V. Alexander, G. Potter, M. Bador, R. Jucá, S. Contractor, M. G. Bosilovich, and S. Cloché (2019), Frogs: A daily $1^\circ \times 1^\circ$ gridded precipitation database of rain gauge, satellite and reanalysis products, *Earth System Science Data*, *11*(3), 1017–1035, doi:10.5194/essd-11-1017-2019.

Rohde, R., and Z. Hausfather (2020), The berkeley earth land/ocean temperature record, *Earth System Science Data*, *12*(4), 3469–3479.

Rollins, M. G. (2009), Landfire: A nationally consistent vegetation, wildland fire, and fuel assessment, *International Journal of Wildland Fire*, *18*, 235–249, doi:10.1071/WF08088.

Runge, J., V. Petoukhov, J. F. Donges, J. Hlinka, N. Jajcay, M. Vejmelka, D. Hartman, N. Marwan, M. Paluš, and J. Kurths (2015), Identifying causal gateways and mediators in complex spatio-temporal systems, *Nature Communications*, *6*, 8502, doi:10.1038/ncomms9502.

Runge, J., P. Nowack, M. Kretschmer, S. Flaxman, and D. Sejdinovic (2019), Detecting and quantifying causal associations in large nonlinear time series datasets, *Science Advances*, *5*(11), eaau4996, doi:10.1126/sciadv.aau4996.

Ruthrof, K. X., J. Fontaine, G. Matusick, D. Breshears, D. Law, S. Powell, and G. Hardy (2016), How drought-induced forest die-off alters microclimate and increases fuel loadings and fire potentials, *International Journal of Wildland Fire*, *25*, 819–830, doi:10.1071/WF15209.

Saha, S., S. Moorthi, H.-L. Pan, et al. (2010), The ncep climate forecast system reanalysis, *Bulletin of the American Meteorological Society*, *91*(8), 1015–1057, doi:10.1175/2010BAMS3001.1.

Samek, W., G. Montavon, A. Vedaldi, L. K. Hansen, and K. R. Müller (Eds.) (2019), *Explainable AI: Interpreting, explaining and visualizing deep learning*, Springer Nature.

Scheff, J., and D. M. Frierson (2012), Robust future precipitation declines in cmip5 largely reflect the poleward expansion of model subtropical dry zones, *Geophysical Research Letters*, *39*, L18,704, doi:10.1029/2012GL052910.

Schoennagel, T., J. K. Balch, H. Brenkert-Smith, P. E. Dennison, B. J. Harvey, M. A. Krawchuk, N. Mietkiewicz, P. Morgan, M. A. Moritz, R. Rasker, M. G. Turner, and C. Whitlock (2017), Adapt to more wildfire in western north american forests as climate changes, *Proceedings of the National Academy of Sciences of the United States of America*, *114*(18), 4582–4590, doi:10.1073/pnas.1617464114.

Schulzweida, U. (2017), *CDO User's Guide*.

Schwalm, C. R., et al. (2017), Global patterns of drought recovery, *Nature*, *548*, 202–205, doi:10.1038/nature23021.

Scott, A. C., D. M. J. S. Bowman, W. J. Bond, S. J. Pyne, and M. E. Alexander (2013), *Fire on Earth: An Introduction*, John Wiley Sons.

Seager, R., and N. Henderson (2013), Diagnostic computation of moisture budgets in the era-interim reanalysis with reference to analysis of cmip-archived atmospheric model data, *Journal of Climate*, *26*(20), 7876–7901.

Seager, R., N. Naik, and G. A. Vecchi (2010), Thermodynamic and dynamic mechanisms for large-scale changes in the hydrological cycle in response to global warming, *Journal of Climate*, *23*(17), 4651–4668.

Sen, P. K. (1968), Estimates of the regression coefficient based on kendall's tau, *Journal of the American Statistical Association*, *63*, 1379–1389.

Senay, G. B., et al. (2013), Operational evapotranspiration mapping using remote sensing and weather datasets: A new parameterization for the sseb approach, *Journal of the American Water Resources Association*, *49*, 577–591, doi:10.1111/jawr.12057.

Seneviratne, S. I., et al. (2012), *Changes in climate extremes and their impacts on the natural physical environment*, pp. 109–230, Cambridge University Press, Cambridge, doi:10.1017/CBO9781139177245.006.

Shepherd, T. G. (2014), Atmospheric circulation as a source of uncertainty in climate change projections, *Nature Geoscience*, *7*, 703–708, doi:10.1038/ngeo2253.

Shiu, C. J., S. C. Liu, C. Fu, A. Dai, and Y. Sun (2012), How much do precipitation extremes change in a warming climate?, *Geophysical Research Letters*, *39*(17).

Short, K. C. (2022), Spatial wildfire occurrence data for the united states, 1992-2020 [fpa˙fod˙20221014], doi:10.2737/RDS-2013-0009.6.

Shrestha, S., and B. Soden (2023), Anthropogenic weakening of the atmospheric circulation during the satellite era, *Geophysical Research Letters*, *50*(22), e2023GL104,784.

Siler, N., C. Proistosescu, and S. Po-Chedley (2019), Natural variability has slowed the decline in western u.s. snowpack since the 1980s, *Geophysical Research Letters*, *46*(1), 346–355, doi:10.1029/2018GL081080.

Sillmann, J., V. V. Kharin, F. W. Zwiers, X. Zhang, and D. Bronaugh (2013), Climate

extremes indices in the cmip5 multimodel ensemble: Part 2. future climate projections, *Journal of Geophysical Research: Atmospheres*, *118*, 2473–2493, doi:10.1002/jgrd.50188.

Simpson, I., K. McKinnon, F. Davenport, M. Tingley, F. Lehner, A. Al Fahad, and D. Chen (2021), Emergent constraints on the large-scale atmospheric circulation and regional hydroclimate: Do they still work in cmip6 and how much can they actually constrain the future?, *Journal of Climate*, *34*(15), 6355–6377.

Sippel, S., N. Meinshausen, E. Fischer, E. Székely, and R. Knutti (2020), Climate change now detectable from any single day of weather at global scale, *Nature Climate Change*, *10*(1), 35–41.

Slivinski, L., G. Compo, J. Whitaker, P. Sardeshmukh, B. Giese, C. McColl, R. Allan, X. Yin, R. Vose, H. Titchner, and J. Kennedy (2019), Towards a more reliable historical reanalysis: Improvements for version 3 of the twentieth century reanalysis system, *Quarterly Journal of the Royal Meteorological Society*, *145*(724), 2876–2908.

Smoliak, B. V., J. M. Wallace, P. Lin, and Q. Fu (2015), Dynamical adjustment of the northern hemisphere surface air temperature field: Methodology and application to observations, *Journal of Climate*, *28*(4), 1613–1629, doi:10.1175/JCLI-D-14-00111.1.

Sohn, B., S. Lee, E. Chung, and H. Song (2016), The role of the dry static stability for the recent change in the pacific walker circulation, *Journal of Climate*, *29*(8), 2765–2779.

Sperry, J. S., M. D. Venturas, H. N. Todd, A. T. Trugman, W. R. L. Anderegg, Y. Wang, and X. Tai (2019), The impact of rising co2 and acclimation on the response of us forests to global warming, *Proceedings of the National Academy of Sciences of the United States of America*, *116*, 25,734–25,744, doi:10.1073/pnas.1913072116.

Stephens, S. L., B. M. Collins, C. J. Fettig, M. A. Finney, C. M. Hoffman, E. E. Knapp, M. P. North, H. Safford, and R. B. Wayman (2018), Drought, tree mortality, and wildfire in forests adapted to frequent fire, *Bioscience*, *68*, 77–88, doi:10.1093/biosci/bix146.

Stott, P., N. Gillett, G. Hegerl, D. Karoly, D. Stone, X. Zhang, and F. Zwiers (2010), Detection and attribution of climate change: A regional perspective, *Wiley Interdisciplinary Reviews: Climate Change*, *1*, 192–211, doi:10.1002/wcc.34.

Strydom, S., and M. J. Savage (2017), Potential impacts of climate change on wildfire dynamics in the midlands of kwazulu-natal, south africa, *Climatic Change*, *143*(3-4), 385–397, doi:10.1007/s10584-017-2019-8.

Sun, Q., C. Miao, Q. Duan, H. Ashouri, S. Sorooshian, and K. L. Hsu (2018), A review of global precipitation data sets: Data sources, estimation, and intercomparisons, *Reviews of Geophysics*, *56*, 79–107, doi:10.1002/2017RG000574.

Sun, Y., S. Solomon, A. Dai, and R. Portmann (2006), How often does it rain?, *Journal of Climate*, *19*(6), 916–934, doi:10.1175/JCLI3672.1.

Swain, D. L. (2021), A shorter, sharper rainy season amplifies california wildfire risk, *Geophysical Research Letters*, *48*(5), e2020GL091,677, doi:10.1029/2021GL092843.

Swain, D. L., B. Langenbrunner, J. D. Neelin, and A. Hall (2018), Increasing precipitation volatility in twenty-first-century california, *Nature Climate Change*, *8*, 427–433, doi:10.1038/s41558-018-0140-y.

Swann, A. L. S., F. M. Hoffman, C. D. Koven, and J. T. Randerson (2016), Plant responses to increasing co2 reduce estimates of climate impacts on drought severity, *Proceedings of the National Academy of Sciences of the United States of America*, *113*, 10,019–10,024, doi:10.1073/pnas.1604581113.

Syphard, A. D., J. E. Keeley, A. H. Pfaff, and K. Ferschweiler (2017), Human presence diminishes the importance of climate in driving fire activity across the united states, *Proceedings of the National Academy of Sciences of the United States of America*, *114*(52), 13,750–13,755, doi:10.1073/pnas.1713885114.

Tai, X., D. S. Mackay, W. R. L. Anderegg, J. S. Sperry, and P. D. Brooks (2017), Plant hydraulics improves and topography mediates prediction of aspen mortality in southwestern usa, *New Phytologist*, *213*, 113–127, doi:10.1111/nph.14129.

Taylor, K., R. Stouffer, and G. Meehl (2012), An overview of cmip5 and the experiment design, *Bulletin of the American Meteorological Society*, *93*(4), 485–498.

Thackeray, C., and A. Hall (2019), An emergent constraint on future arctic sea-ice albedo feedback, *Nature Climate Change*, *9*(12), 972–978.

Theil, H. (1950), A rank-invariant method of linear and polynomial regression analysis, *Indagationes Mathematicae*, *12*, 85–91.

Tian, B., and X. Dong (2020), The double-itcz bias in cmip3, cmip5, and cmip6 models based on annual mean precipitation, *Geophysical Research Letters*, *47*(8), e2020GL087,232.

Toms, B. A., E. A. Barnes, and I. Ebert-Uphoff (2020), Physically interpretable neural networks for the geosciences: applications to earth system variability, *Journal of Advances in Modeling Earth Systems*, *12*, e2019MS002,002, doi:10.1029/2019MS002002.

Trenberth, K., A. Dai, R. Rasmussen, and D. Parsons (2003), The changing character of precipitation, *Bulletin of the American Meteorological Society*, *84*(9), 1205–1218, doi:10.1175/BAMS-84-9-1205.

USGCRP (2023), Fifth national climate assessment, doi:10.7930/NCA5.2023.

van Wagtendonk, J. W. (Ed.) (2018), *Fire in California's Ecosystems*, University of California Press.

Vecchi, G. A., and B. J. Soden (2007), Global warming and the weakening of the tropical circulation, *Journal of Climate*, *20*(17), 4316–4340.

Vicente-Serrano, S. M., et al. (2013), Response of vegetation to drought time-scales across global land biomes, *Proceedings of the National Academy of Sciences of the United States of America*, *110*, 52–57, doi:10.1073/pnas.1207068110.

Wang, D., D. Guan, S. Zhu, M. Mac Kinnon, G. Geng, Q. Zhang, H. Zheng, T. Lei, S. Shao, P. Gong, and S. J. Davis (2021), Economic footprint of california wildfires in 2018, *Nature Sustainability*, *4*(3), 252–260, doi:10.1038/s41893-020-00646-7.

Wang-Erlandsson, L., et al. (2016), Global root zone storage capacity from satellite-based evaporation, *Hydrology and Earth System Sciences*, *20*, 1459–1481, doi:10.5194/hess-20-1459-2016.

Wehner, M., D. R. Easterling, J. H. Lawrimore, R. R. Heim, R. S. Vose, and B. D. Santer (2011), Projections of future drought in the continental united states and mexico, *Journal of Hydrometeorology*, *12*, 1359–1377, doi:10.1175/JHM-D-11-15.1.

Westerling, A. L. (2016), Increasing western us forest wildfire activity: Sensitivity to changes in the timing of spring, *Philosophical Transactions of the Royal Society B: Biological Sciences*, *371*(1696), 20150,178, doi:10.1098/rstb.2015.0178.

Westerling, A. L. (2018), Wildfire simulations for california's fourth climate change assessment: Projecting changes in extreme wildfire events with a warming climate, California's Fourth Climate Change Assessment, California Energy Commission.

Westerling, A. L., H. G. Hidalgo, D. R. Cayan, and T. W. Swetnam (2006), Warming and earlier spring increase western u.s. forest wildfire activity, *Science*, *313*(5789), 940–943, doi:10.1126/science.1128834.

Williams, A. P., R. Seager, J. T. Abatzoglou, B. I. Cook, J. E. Smerdon, and E. R. Cook (2015), Contribution of anthropogenic warming to california drought during 2012-2014, *Geophysical Research Letters*, *42*(16), 6819–6828, doi:10.1002/2015GL064924.

Williams, A. P., J. T. Abatzoglou, A. Gershunov, J. Guzman-Morales, D. A. Bishop, J. K. Balch, and D. P. Lettenmaier (2019), Observed impacts of anthropogenic climate change on wildfire in california, *Earth's Future*, *7*(8), 892–910, doi:10.1029/2019EF001210.

Williams, A. P., et al. (2013), Temperature as a potent driver of regional forest drought stress and tree mortality, *Nature Climate Change*, *3*, 292–297, doi:10.1038/nclimate1693.

Williamson, G. J., L. D. Prior, W. M. Jolly, M. A. Cochrane, B. P. Murphy, and D. M. J. S. Bowman (2016), Measurement of inter- and intra-annual variability of landscape fire activity at a continental scale: The australian case, *Environmental Research Letters*, *11*(3), 035,003, doi:10.1088/1748-9326/11/3/035003.

Williamson, M., P. Cox, and F. Nijsse (2018), Theoretical foundations of emergent constraints: relationships between climate sensitivity and global temperature variability in conceptual models, *Dynamics and Statistics of the Climate System*, *3*(1), dzy006.

Williamson, M., C. Thackeray, P. Cox, A. Hall, C. Huntingford, and F. Nijsse (2021), Emergent constraints on climate sensitivities, *Reviews of Modern Physics*, *93*(2), 025,004.

Wills, R., S. Sippel, and E. Barnes (2020a), Separating forced and unforced components of climate change: The utility of pattern recognition methods in large ensembles and observations, *Variations*, *18*(2), 1–10.

Wills, R. C. J., D. S. Battisti, K. C. Armour, T. Schneider, and C. Deser (2020b), Pattern recognition methods to separate forced responses from internal variability in climate model ensembles and observations, *Journal of Climate*, *33*(20), 8693–8719, doi:10.1175/JCLI-D-19-0855.1.

Wotton, B. M., and M. D. Flannigan (1993), Length of the fire season in a changing climate, *The Forestry Chronicle*, *69*(2), 187–192, doi:10.5558/tfc69187-2.

Yeh, S., W. Cai, S. Min, M. McPhaden, D. Dommenget, B. Dewitte, M. Collins, K. Ashok, S. An, B. Yim, and J. Kug (2018), Enso atmospheric teleconnections and their response to greenhouse gas forcing, *Reviews of Geophysics*, *56*(1), 185–206.

Yin, J. (2005), A consistent poleward shift of the storm tracks in simulations of 21st century climate, *Geophysical Research Letters*, *32*, L18,701, doi:10.1029/2005GL023684.

Young, D. J. N., J. T. Stevens, J. M. Earles, J. Moore, A. Ellis, A. L. Jirka, and A. M. Latimer (2017), Long-term climate and competition explain forest mortality patterns under extreme drought, *Ecology Letters*, *20*, 78–86, doi:10.1111/ele.12711.

Yu, B., and F. Zwiers (2010), Changes in equatorial atmospheric zonal circulations in recent decades, *Geophysical Research Letters*, *37*(5).

Yu, B., F. Zwiers, G. Boer, and M. Ting (2012), Structure and variances of equatorial zonal circulation in a multimodel ensemble, *Climate Dynamics*, *39*, 2403–2419.

Zhang, S., P. Stier, G. Dagan, C. Zhou, and M. Wang (2023), Sea surface warming patterns drive hydrological sensitivity uncertainties, *Nature Climate Change*, *13*(6), 545–553.

Zheng, X., S. Xie, L. Lv, and Z. Zhou (2016), Intermodel uncertainty in enso amplitude change tied to pacific ocean warming pattern, *Journal of Climate*, *29*(20), 7265–7279.

Zhuang, J., V. M. Payyappalli, A. Behrendt, and K. Lukasiewicz (2017), Total cost of fire in the united states.

Zhuang, Y., R. Fu, B. D. Santer, R. E. Dickinson, and A. Hall (2021), Quantifying contributions of natural variability and anthropogenic forcings on increased fire weather risk over the western united states, *Proceedings of the National Academy of Sciences of the United States of America*, *118*(45), e21104105,118, doi:10.1073/pnas.21104105118.

Ziese, M., A. Rauthe-Schöch, A. Becker, P. Finger, A. Meyer-Christoffer, and U. Schneider (2018), Gpcc full data daily version. 2018 at 1.0°: Daily land-surface precipitation from

rain-gauges built on gts-based and historic data, Global Precipitation Climatology Centre (GPCC, http://gpcc.dwd.de/) at Deutscher Wetterdienst.